

Terminal Settling Velocity of a Sphere in a non-Newtonian Fluid

by

Ameneh Shokrollahzadeh

A thesis submitted in partial fulfillment of the
requirements for the degree of

Master of Science

in

Chemical Engineering

Department of Chemical and Materials Engineering

University of Alberta

Abstract

The production and disposal of thickened tailings continue to grow in importance in the mining industry around the world. Prediction of particle settling during transportation and handling processes is a critical element in system design and operation. Wilson et al. (2003) presented a direct method that was able to provide reasonably accurate predictions for the terminal settling velocity of a sphere in a fluid with a yield stress. The application of this method is limited; if the fluid yield stress is larger than the reference shear stress proposed by this method ($0.3\bar{\tau} \leq \tau_y$), the correlation cannot be used. The current study presents measurements of fall velocities of precision spheres in concentrated Kaolinite-water suspensions (10.6% to 21.7% by volume). Both Casson and Bingham models have been used to model the fluid rheology which provided yield stress values in the range of 1.3 Pa to 30 Pa, depending primarily on the clay concentration. An analogy of the Wilson-Thomas analysis for pipe flow of non-Newtonian fluids (Wilson and Thomas, 1985) has been used to develop a new method for predicting the terminal settling velocity of a sphere in a viscoplastic fluid. There are no limits for applicability of the new method and its performance on the experimental results from this study, along with data taken from the literature, shows higher accuracy in its predictions than the direct method of Wilson et al. (2003).

Acknowledgements

First of all, my deepest gratitude goes to my supervisor Dr. Sean Sanders whose supportive nature and dedicated character made me a better researcher. I will forever treasure my experience as a MSc student under his supervision.

Special thanks goes to Terry Runyon for her endless help. I would also like to thank my colleagues and friends in the Pipeline Transport Processes Research Group, especially Hamed Sepehr, Ardalan Sadighian and Maedeh Marefatallah for our friendship and all the fruitful conversations during this research. I would like to thank Allen Reule and Mohsen Khadem for their kindness, patience, and extremely useful consultations. I also appreciate the generous assistance of Christopher Billington and Amanda Marchak in the lab during the experimental work.

I would like to thank the NSERC Industrial Research Chair in Pipeline Transport Processes for funding this project.

The warmest appreciation goes to my husband Amir, who shows me the meaning of love everyday and always goes above and beyond all limits to be there for me.

I am eternally indebted to my family. My parents, Habibeh and Ebrahim and my brothers Hassan and Hossein, who are not physically close to me but I can feel their unconditional love and support from the other side of the planet every single day.

Table of Contents

Abstract	ii
1. Problem statement.....	1
1.1 Introduction	1
1.2 Project objectives	9
2. Background	10
2.1 Rheology of viscoplastic fluids	10
2.1.1 Rheology models	10
2.1.2 Rheometry.....	12
2.2 Kaolinite-water suspensions	15
2.2.1 Origins of viscoplastic behavior	15
2.2.2 Shear sensitivity	17
2.2.3 Determining yield stress	19
2.3 Settling sphere in a fluid.....	21
2.3.1 Settling sphere in a Newtonian fluid	21
2.3.2 Settling sphere in a viscoplastic fluid	26
2.4 Wall effects	36
2.4.1 Newtonian medium.....	36
2.4.2 Viscoplastic medium.....	39
3. Experimental method	43
3.1 Materials.....	43
3.1.1 Spheres	43
3.1.2 Kaolinite.....	45
3.1.3 Corn syrup.....	45
3.2 Equipment	45
3.2.1 Settling column	45
3.2.2 EIT sensors.....	48
3.2.3 Releasing mechanism.....	52
3.2.4 Rheometer	53
3.2.5 Mixer.....	54

3.3	Procedures	54
3.3.1	Preparation of corn syrup solutions	54
3.3.2	Preparation of Kaolinite-water mixture	55
3.3.3	Fluid density measurements.....	56
3.3.4	EIT operation	56
3.3.5	Settling tests	57
3.3.6	Kaolinite-water suspension rheometry.....	59
3.3.7	Additional shearing procedure for highly-concentrated suspensions ...	62
4.	Results and Discussion	63
4.1	Settling tests: Newtonian fluids.....	63
4.2	Settling tests: Kaolinite-water suspensions	69
4.3	Analysis of Wilson et al. (2003) direct method	77
4.4	Pipe flow analogy for non-Newtonian fluids	78
4.5	Analysis of rheogram shape factor.....	81
4.6	The modified prediction method	82
4.7	Modification development	83
4.7.1	Category I: fall velocity prediction for systems with $\alpha < 1.3$	87
4.7.2	Category II: fall velocity prediction for systems with $\alpha \geq 1.3$	89
5.	Conclusions and recommendations for future work	98
5.1	Summary and conclusions.....	98
5.2	Recommendations for future work.....	100
	References.....	101
	Appendix 1: Calibration tests.....	106
	Appendix 2: Properties of Kaolinite-water suspensions	111
	Appendix 3: Velocity measurements for spheres falling in Kaolinite-water suspensions	144
	Appendix 4: MatLab codes for correlation development	160
	Appendix 5: Genetic algorithm (GA)	164
	Appendix 6: Diagrams and pictures.....	166

List of Figures

Figure 1.1 Typical rheogram of a viscoplastic fluid	3
Figure 1.2 Images from a video sequence showing stratification of sand particle in a flowing yield stress fluid, from Thomas et al. (2004).....	6
Figure 2.1 Typical rheograms for viscoplastic fluids	11
Figure 2.2 Schematic view of concentric cylinder apparatus	13
Figure 2.3 Schematic view of cone and plate geometry	14
Figure 2.4 Different types of particle attachment in Kaolinite-water suspensions, (a) edge to face flocculated and aggregated, (b) edge to edge flocculated and aggregated, (c) face to face flocs not aggregated, (d) fully dispersed (van Olphen, 1977).....	16
Figure 2.5 Casson and Bingham models fit to the same Kaolinite-water mixture ($C_v=12.2\%$) rheometry measurements	17
Figure 2.6 Two vertically aligned identical bronze spheres (7.94 mm diameter), released with 2 seconds delay, in 1.1% Floxit solution (Gumulya, 2009).....	19
Figure 2.7 Rheograms of a Kaolinite-water sample ($C_v=15.8\%$) obtained with cone-and-plate and concentric cylinder geometries.....	21
Figure 2.8 Schematic diagram of forces acting on a sphere falling in a Newtonian fluid	22
Figure 2.9 Standard drag curve for a sphere falling in a Newtonian fluid (Clift et al. 1978)	24
Figure 2.10 Standard curve for a sphere falling in a Newtonian fluid based on the Wilson et al. (2003) method (reproduced).....	26
Figure 2.11 Shape of the sheared envelope surrounding a sphere in creeping motion in viscoplastic fluid: (a) Ansley and Smith (1967); (b) Yoshioka et al. (1971); (c) Beris et al. (1985), from Chhabra (2007)	28
Figure 2.12 Yielded (white) and unyielded (black) regions for flow of a Bingham fluid around a fixed sphere contained in a square cylinder with $L/d=4$ (Prashant & Derksen, 2011).....	29
Figure 2.13 Drag curve presented by Ansley and Smith (1967) for a sphere falling in a Bingham fluid (from Saha et al. (1992)).....	32

Figure 2.14 Overall performance of the correlation proposed by Atapattu et al. (1995), from Atapattu et al. (1995).....	33
Figure 2.15 Experimental fall velocity measurements reported by Wilson et al. (2003, 2004) and shown on their standard Newtonian curve, with $\tau_{ref}=0.3\bar{\tau}$	35
Figure 2.16 Schematic view of hindering effect of container boundaries on settling velocity of a single sphere in a Newtonian fluid.....	37
Figure 2.17 Schematic representation of the system of a sphere falling in a tube filled with a viscoplastic medium. Both the outer shaded regions and dark interior regions are unyielded (Beaulne and Mitsoulis, 1997).....	40
Figure 2.18 Size of the sheared zone around a particle moving at different velocities in a viscoplastic fluid ($\lambda=1/3$), from Beaulne and Mitsoulis (1997).....	41
Figure 3.1 Schematic view of the settling apparatus.....	47
Figure 3.2 Side view (left) and top view (right) of EIT sensor electrode arrangements.....	48
Figure 3.3 EIT reconstruction grids.....	49
Figure 3.4 Typical conductivity measurements for two planes as an aluminum sphere passes through each plane; Data acquisition speed was 670 fps.....	51
Figure 3.5 Reconstructed conductivity maps of aluminum sphere at the moment of arrival at the first plane (upper).....	51
Figure 3.6 Schematic illustration of the releasing mechanism.....	53
Figure 4.1 Sample conductivity maps for settling tests showing straight particle trajectory (left) and angled particle path (right).....	64
Figure 4.2 Sample of plane averaged conductivity measurements for settling tests with (a) a 12.7 mm aluminum sphere that has reached its terminal settling velocity and (b) an accelerating 12.7mm steel sphere.....	65
Figure 4.3 Terminal settling velocities corrected for wall effects; tests conducted with Newtonian fluids.....	69
Figure 4.4 Time-dependent behavior for a Kaolinite-water suspension ($C_v=22\%$); cone-and-plate rheometer; $\omega=20$ rad/s.....	71
Figure 4.5 Settling velocity measurements for four identical 12.7 mm ceramic spheres released at different time intervals; 15.6% Kaolinite-water mixture.....	72

Figure 4.6 Settling velocity measurements for six identical steel spheres (d=15.9 mm) released at 4 minutes intervals; 16% Kaolinite-water mixture	73
Figure 4.7 Settling velocity measurements for four identical steel spheres (d=17.5 mm) in 19.8% Kaolinite-water suspension; when the fluid was mixed before each individual test.....	73
Figure 4.8 Rheometry measurements for a single Kaolinite-water suspension (C _v =15.8%) made at 4 minutes intervals during settling tests	74
Figure 4.9 Casson and Bingham models fitted to rheogram of a Kaolinite-water suspension (C _v =19.8%)	75
Figure 4.10 Experimental results from current study plotted by Wilson et al. (2003) method.....	76
Figure 4.11 Comparisons of fall velocities measured during the present study and the predictions of the Wilson et al. (2003) method.....	77
Figure 4.12 The rheogram shape factor (α)	79
Figure 4.13 Comparison of α values calculated using the Casson and Bingham rheology models.....	82
Figure 4.14 The change in modeling parameter (β) with increase of characteristic shear stress (ξ)	86
Figure 4.15 The change in modeling parameter (β) with increase of rheogram shape factor (α).....	86
Figure 4.16 Experimental results and the fitted surface of function f , $\alpha < 1.3$	87
Figure 4.17 Comparison of experimental results and predicted velocities by modified method, $\alpha < 1.3$	89
Figure 4.18 Experimental results and the fitted surface of function f , $\alpha \geq 1.3$	90
Figure 4.19 Comparison of experimental results and predicted velocities by modified method , $\alpha \geq 1.3$	91
Figure 4.20 Prediction of relative velocities by the modified method for 360 data points.....	92
Figure 4.21 Velocity predictions by the modified method, applied to data for which the method of Wilson et al. (2003) provide no predictions	94

Figure 4.22 Terminal settling velocity predictions using the modified method for a sphere falling in a viscoplastic fluid 95

Figure 4.23 Rheogram of a Kaolinite-water suspension ($C_v=20.1\%$), obtained over two different shear rate ranges. The dotted lines represent the Bingham model fit to the two data sets 96

List of Tables

Table 1.1 Laminar-to-turbulent transition velocities for suspensions in a 300 mm pipe (Pullum et al. 2004).....	4
Table 2.1 Constitutive rheological models commonly used to describe viscoplastic fluids	12
Table 2.2 Physical properties and measured terminal settling velocity for a sphere falling in a Herschel-Bulkley fluid, reported by Gumulya (2009).....	34
Table 2.3 Correlations for estimating wall effects for a particle settling in a Newtonian fluid (Chhabra et al., 2003).....	39
Table 3.1 Properties of the precision spheres used in the present study.....	44
Table 4.1 Measured fall velocities for single spheres in corn syrup-water solution ($C_v=26\%$).....	67
Table 4.2 Measured fall velocities for single spheres in water.....	68
Table 4.3 Comparison of the performance of the modified method and Wilson et al. (2003) method for a sphere settling in a viscoplastic fluid, $\alpha < 1.3$	88
Table 4.4 Comparison of the performance of the modified method and Wilson et al.'s method for a sphere settling in a viscoplastic fluid, $\alpha \geq 1.3$	91
Table 4.5 The performance of the modified method for predicting the terminal settling velocities of a sphere falling in a viscoplastic fluid based on choice of Bingham or Casson fluid model	95
Table 4.6 Velocity predictions for a steel sphere ($\rho_s=7684 \text{ kg/m}^3$, $d=0.01428 \text{ m}$) in a Kaolinite-water suspension ($C_v= 20.1\%$, $\rho_f=1331 \text{ kg/m}^3$) fitted with two different Bingham models based on rheology measurements made over two different shear rate ranges	97

List of symbols

<i>Symbol</i>	Description	Unit
A_p	projected surface area of falling particle	m^2
Bn	Bingham number	-
Bn^*	modeling parameter	-
C_D	drag coefficient	-
C_V	volume fraction	-
D	container diameter	m
d	sphere diameter	m
f_w	wall factor	-
F_B	buoyancy force	N
F_D	drag force	N
F_G	gravity force	N
g	gravitational acceleration	m/s^2
K	Consistency index	$(Pa.s)^n$
L	bob length	m
n	Power law index	-
P	pressure	Pa
Q	Dynamic parameter	-
Q^*	modified dynamic parameter	-
r	radial coordinate	m
R_1	bob radius	m
R_2	cup radius	m

R	cone radius	m
Re^*	shear Reynolds number	-
Re_N^*	modeling parameter	-
Re_p	particle Reynolds number	-
Re_{HB}^*	modeling parameter	-
t	time	s
T	torque	N.m
\bar{U}	Mean flow velocity	m/s
U^*	flow shear velocity	m/s
V	particle velocity	m/s
V_t	Terminal settling velocity	m/s
V^*	particle shear velocity	m/s
V_{tm}	measured settling velocity	m/s
V_{tp}	predicted terminal settling velocity	m/s
\bar{V}_{tm}	averaged measured velocity	m/s
x	a parameter from Wilson et al.'s method	-
y	a parameter from Wilson et al.'s method	-
Y_G	yield-gravity parameter	-
α	rheogram shape factor	-
α_c	rheogram shape factor calculated from Casson model	-
α_B	rheogram shape factor calculated from Bingham model	-
β	modeling parameter $(\frac{\mu_N}{\mu_{eq}})$	-
$\dot{\gamma}$	shear rate	s ⁻¹

$\dot{\gamma}_r$	total shear rate of the particle	s^{-1}
$\dot{\gamma}_{ep}$	shear rate of falling particle in a stationary medium	s^{-1}
$\dot{\gamma}_x$	shear rate exerted on the particle due to fluid velocity	s^{-1}
$\bar{\gamma}$	calculated shear rate at $\bar{\tau}$	s^{-1}
ε	correlation parameter	-
θ	cone angle	rad
λ	sphere-to-tube diameter ratio	-
λ_{crit}	critical sphere-to-tube diameter ratio	-
μ	viscosity	Pa.s
μ_B	Bingham plastic viscosity	Pa.s
μ_c	Casson plastic viscosity	Pa.s
μ_{eq}	equivalent Newtonian viscosity at a reference point	Pa.s
μ_{app}	apparent viscosity of non-Newtonian fluid	Pa.s
μ_N	calculated Newtonian viscosity based on measured velocity	Pa.s
ξ	relative shear stress	-
ρ_s	particle (sphere) density	kg/m^3
ρ_f	fluid density	kg/m^3
ρ_m	mixture density	kg/m^3
τ	shear stress	Pa
$\bar{\tau}$	mean surficial stress on a falling sphere	Pa
τ_B	Bingham yield stress	Pa
τ_c	Casson yield stress	Pa

τ_{HB}	Herschel-Bulkley yield stress	Pa
τ_{ref}	reference shear stress	Pa
$\tau_{r\theta}$	local shear stress	Pa
τ_y	yield stress	Pa
τ_w	wall shear stress	Pa
ω	rotor speed	rad/s

1. Problem statement

1.1 Introduction

In the past two decades, economic and environmental considerations have had an increasing influence on the design and operation of waste management systems in the mining industry (Wilson et al., 2005). There has been growing pressure from regulatory agencies to decrease water usage, and at the same time, stakeholders demand higher rates of production to be able to compete in the growing market (Thomas et al. 2004). As a result, producing tailings waste with higher solids concentration has become more attractive and more necessary.

In the mine tailings disposal process, slurry pipelines are economically efficient, and thus have become the standard mode of transportation of waste tailings (Shook et al., 2002). The tailings stream consists of coarse particles, fine particles and a liquid phase. In most occasions the concentration of surface-active fine particles is high enough to form a colloidal suspension. The suspension formed from mixing the fine particles with the liquid (often $< 44 \mu\text{m}$ particles + water) is referred to as the “carrier fluid”. This type of carrier fluid invariably exhibits non-Newtonian behavior at higher solids concentration (Shook et al. 2002; Pullum et al. 2004).

Accurate prediction of the coarse particle settling process in a non-Newtonian carrier fluid under pipeline conditions is critical in the design, control, and operation of pipelines, pumps, and other elements of the transportation system; for example, the prediction of solids concentration distributions in slurry pipelines (Gillies and Shook 1994; Wilson et al. 2005; Kaushal and Tomita 2013). For spherical particles in

Newtonian fluids, these predictions are easily and accurately made (Whyte 1999). The options for predicting terminal particle settling velocity in non-Newtonian fluids are much more limited; therefore, the focus of the present study is on the prediction of the terminal settling velocity of a spherical particle in a non-Newtonian fluid.

To explain the problem more explicitly, a typical tailings disposal system is considered. The highly concentrated waste material from the mining complex is transported as slurry via pipeline to the tailings area for permanent storage. This slurry contains coarse particles, fine particles and a liquid phase (usually water). Fine particles and water form a non-Newtonian mixture that commonly behaves as a viscoplastic fluid (Gillies et al., 1997). This behavior is unique in that below a critical or minimum amount of applied force, no shear rate is produced; above a critical force, the fluid starts to flow (Chhabra, 2007). This critical minimum applied force, normalized using the area over which the force is applied, is referred to as “yield stress”. A typical example of this fluid flow behavior can be seen in Figure 1.1, which shows the rate of deformation of a paste-like material as a function of the applied shear stress.

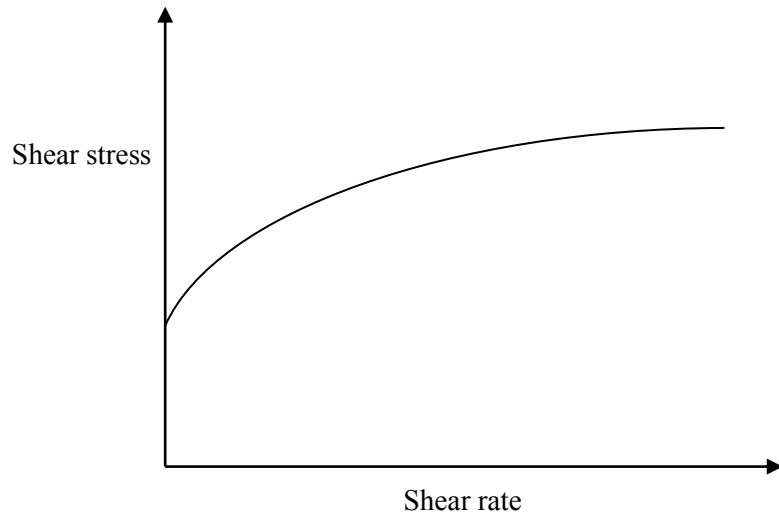


Figure 1.1 Typical rheogram of a viscoplastic fluid

By virtue of its yield stress, a stagnant viscoplastic fluid can keep even a relatively large particle suspended for an indefinite period of time. When a particle is placed in a stagnant viscoplastic fluid, the immersed weight of the particle is balanced by the fluid yield stress. There are several methods available to compare the magnitudes of these forces and determine whether the weight of the submerged particle is large enough to overcome the yield stress or not. In order to compare the gravity force acting on a sphere to the upward resistance forces -buoyancy and yield stress- a dimensionless number is commonly used:

$$Y_G = \frac{\tau_y}{dg(\rho_s - \rho_f)} \quad (1.1)$$

For a sphere to be suspended in a viscoplastic fluid in a typical stagnant or unsheared mineral slurry, $Y_G \geq 0.1$ (Thomas 1978; Cooke 2002; Wilson et al. 2005). Once the

slurry is sheared, however, even particles that were held motionless in the fluid will begin to settle (Cooke, 2002; Chhabra, 2007). Generally, fluid turbulence is relied upon to suspend the solids under sheared (flowing) conditions (Shook et al. 2002).

Even though it is ideal to have turbulent flow in slurry pipelines to decrease the probability of settling, laminar flow of heterogeneous non-Newtonian slurries is specifically attractive because, when the mixture yield stress increases, it is economically infeasible to operate in turbulent flow (Wilson et al. 2005). The viscoplastic nature of the carrier fluid radically delays the onset of turbulence and therefore increases the laminar-turbulent transition velocity (Pullum et al. 2004). In some sites the operation of a transportation system can occur only at velocities very near the transition velocity. If this is not possible, then operating in laminar flow is the only viable option (Pullum et al. 2004). In Table 1.1, the transition velocity of a water-based viscoplastic suspension typical of those produced by a thickener is compared to transition velocity of a Newtonian fluid.

Table 1.1 Laminar-to-turbulent transition velocities for suspensions in a 300 mm pipe (Pullum et al. 2004)

Mixture rheology	ρ_m (kg/m ³)	τ_y (Pa)	Transition velocity (m/s)
Newtonian	1000	-	0.01
Viscoplastic	1200	10	3.9

Transportation of highly concentrated slurries of coarse and fine coal particles under laminar conditions was first introduced by Elliot & Gilddon (1970). It was observed

that the non-Newtonian carrier fluid kept the coarse particles suspended at the center of the pipe and this phenomenon essentially reduced the total pressure gradient in the test pipe loop. This type of laminar flow was referred to as “stabilized flow”. Later, visualization studies showed that when the fluid is being sheared, the particles which were held suspended in an unsheared (stagnant) fluid tend to settle given enough time (Graham et al, 2003; Pullum 2003). Experiments done by Thomas et al. (2004) confirmed those observations and showed that the settling occurs quickly during the shearing that occurs in a pipeline. After a short amount of time, these settled particles were observed to form a sliding bed which moved more slowly than the rest of the flow. Figure 1.2 shows the observations of the stabilized flow reported by Thomas et al. (2004). Sand particles with 2mm diameter which were held suspended in a stagnant viscoplastic fluid with 25 Pa yield stress are introduced to the system from the right side and as can be seen after 6 seconds a bed starts to form.

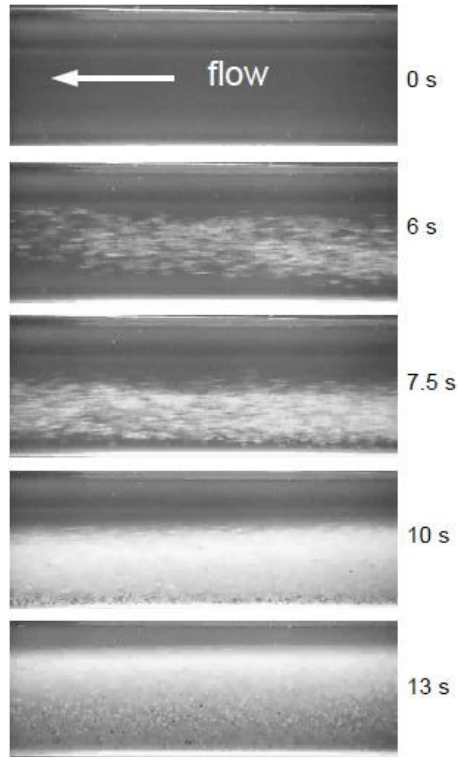


Figure 1.2 Images from a video sequence showing stratification of sand particle in a flowing yield stress fluid, from Thomas et al. (2004)

The formation of the bed of solids can drastically affect the transportation of the material in the pipeline. If the solids bed moves more slowly than the rest of the flow, the majority of coarse particles will move at a lower velocity than the mean flow velocity, and as a result the in-situ solids concentration will be higher than the solids concentration at the entrance (and at the discharge) (Gillies et al. 1999), which results in a higher pressure gradient (Gillies et al. 2007). If the settled bed is stationary, its existence reduces the effective inner diameter of the pipe which again increases pressure losses dramatically (Shook et al. 2002).

These observations suggest that the mechanism of particle settling in viscoplastic fluids is completely different in a stagnant fluid than in a sheared medium. To model complexities of settling process in flowing viscoplastic fluid, Wilson et al. (2004) introduced an equation for total shear rate applied to a coarse particle in a sheared carrier fluid:

$$\dot{\gamma}_r = [(\dot{\gamma}_{ep})^2 + (\dot{\gamma}_x)^2]^{0.5} \quad (1.2)$$

where $\dot{\gamma}_{ep}$ is the shear rate of the falling particle in a stationary medium, $\dot{\gamma}_x$ is the additional shear rate exerted on the particle due to fluid velocity and $\dot{\gamma}_r$ is the resultant total shear rate. As Equation (1.2) shows, a particle is exposed to a higher shear rate in a sheared medium than in a stationary fluid. For a typical rheological behavior of a viscoplastic fluid, such as the rheogram shown in Figure 1.1, a high shear rate corresponds to a lower viscosity. With a small viscosity, the particle falls more rapidly. Equation (1.2) suggests that a suspended particle in a sheared fluid settles and the fall velocity is higher than the fall velocity in a stagnant fluid. This prediction is in agreement with several observations in the literature (Graham et al. 2003; Thomas et al. 2004; Pullum et al. 2004; Gillies et al. 2007, Talmon et al. 2014).

Accurate prediction of $\dot{\gamma}_{ep}$ and $\dot{\gamma}_x$ is therefore essential in predicting the settling behavior of particles transported by pipeline. For that reason, prediction of the terminal settling velocity of a particle in a stagnant viscoplastic fluid is an important area of research.

There are several available methods to predict the terminal settling velocity of a spherical particle in a Newtonian fluid; for a particle settling in a viscoplastic fluid,

however, there are a limited number of techniques available in the literature. Analytical methods have led to limited results for highly constrained, carefully specified systems (Chhabra 2007). Several correlations have been developed to offer a convenient solution to the problem for engineering purposes. These different approaches will be reviewed in Chapter 2.

One of the practical problems in predicting terminal settling velocity – even in Newtonian fluids – is that usually an iterative procedure is required. Wilson et al. (2003) introduced a new method to predict the terminal settling velocity of spheres in Newtonian fluids directly, but the more important aspect of the proposed method was that it was also able to predict the terminal settling velocity of a sphere in a non-Newtonian, viscoplastic fluid by using an “apparent viscosity”. Apparent viscosity is a single number that is calculated based on the physical properties of the system and is able to represent the rheology of the fluid in that specific fluid-particle system. This method not only provides direct predictions for terminal settling velocities of spheres in viscoplastic fluids, it is also applicable to a wide range of system properties.

There are features of this method that limit both its applicability and its prediction accuracy. These shortcomings – which will be discussed in detail in Chapter 2– can dramatically limit the prediction of the fluid-particle settling conditions. Also industrially important conditions cannot always be modeled using this method. For this reason, a modified direct prediction method is required to predict the settling occurrence, and to provide a reasonably accurate estimation of the terminal settling velocity for a wide range of system properties.

1.2 Project objectives

The primary objective of this research is to develop a method to accurately predict terminal settling velocity of a sphere in a viscoplastic fluid. In order to do this, an experimental approach has been taken. The major activities that must be completed to meet this objective are:

- To analyze and evaluate existing methods of prediction for terminal settling velocity of spheres in viscoplastic fluids and identify the strength and limitations of each method;
- To develop a system of experimental equipment and a methodology through which the terminal settling velocity of a sphere in a viscoplastic suspension can be accurately measured for a wide range of fluid-particle system properties;
- To develop an inclusive and accurate direct method for predicting the terminal settling velocity of a sphere in a viscoplastic fluid based on the experimental results obtained from the present investigation and from experimental results available in literature.

2. Background

2.1 Rheology of viscoplastic fluids

2.1.1 Rheology models

When a Newtonian fluid is subjected to an applied force, the rate of deformation has a linear relationship with that force (Bird et al. 2007). Under laminar viscous flow conditions, the slope of this line, i.e. the Newtonian viscosity, is constant and independent of the force applied, the shear rate range, or time. Any deviation from this behavior is described as non-Newtonian behavior. There are several models to represent non-Newtonian fluid behavior; in some cases, more than one model can represent the fluid rheological properties. The focus here is on time-independent non-Newtonian behavior.

Among non-Newtonian fluids, the “viscoplastic” category is used to describe fluids that exhibit a yield stress. Although the existence of “true yield stress” in viscoplastic materials has been a subject of debate (Barnes and Walters, 1985), the concept has proven to be extremely useful in practice. The physical meaning of yield stress is often related to the postulation that the fluid at rest has a structure that will not break unless the external stress exceeds a minimum value (Andres 1961; Hariharaputhiran et al. 1998).

In characterizing fluid rheology, a plot of shear stress against shear rate (rheogram) is typically used. For viscoplastic fluids, the rheogram does not pass through the origin. Figure 2.1 shows a rheogram upon which different viscoplastic fluid models have been drawn. Note that the Newtonian fluid is shown for comparison.

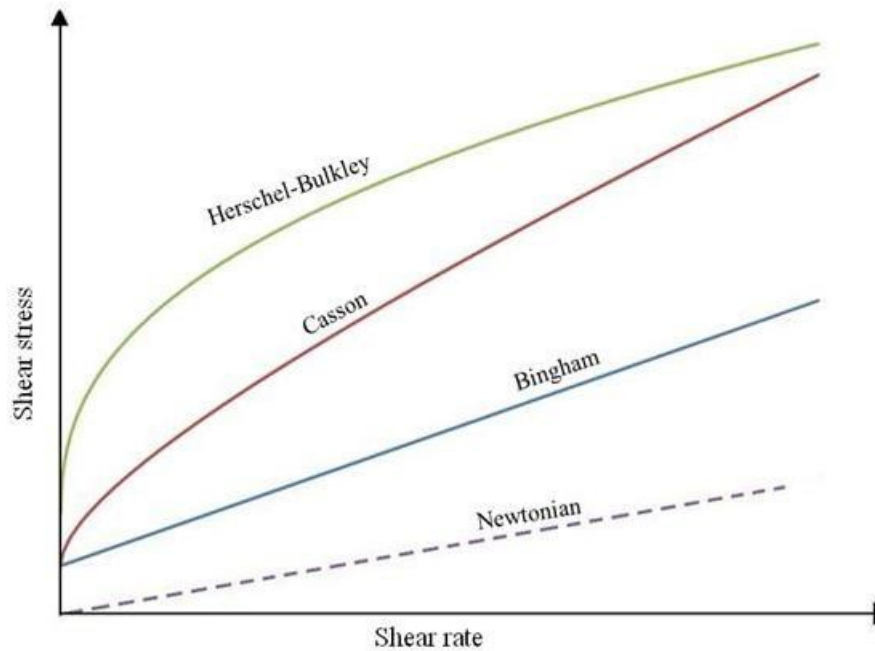


Figure 2.1 Typical rheograms for viscoplastic fluids

Several different mathematical models can be used to represent the rheological behavior of a viscoplastic fluid. When the fluid is subjected to a shear stress less than fluid yield stress, no measureable flow takes place. For this reason all these mathematical relationships hold only for shear stresses larger than yield stress. It is important to note that the magnitude of fluid yield stress obtained from the rheogram is a fitting parameter which can strongly depend on shear rate range of the measurements. Table 2.1 shows some of the rheological models commonly used to characterize viscoplastic fluids.

Table 2.1 Constitutive rheological models commonly used to describe viscoplastic fluids

Newtonian*	$\tau = \mu\dot{\gamma}$
Bingham	$\tau = \mu_B\dot{\gamma} + \tau_B$
Casson	$\tau^{0.5} = \mu_c^{0.5}\dot{\gamma}^{0.5} + \tau_c^{0.5}$
Herschel-Bulkley	$\tau = K\dot{\gamma}^n + \tau_{HB}$

* Provided for comparison; not used for viscoplastic fluids

2.1.2 Rheometry

Rotational rheometry tests with concentric cylinder geometry are commonly conducted to investigate the flow behavior of both Newtonian and non-Newtonian fluids. Typically, a rheometer with concentric cylinder geometry measures the torque T required to rotate a spindle of radius R_1 and effective height L at an angular velocity ω immersed in a fluid contained in a cup with radius R_2 (Shook et al. 2002). Figure 2.2 shows a schematic view of a concentric cylinder viscometer.

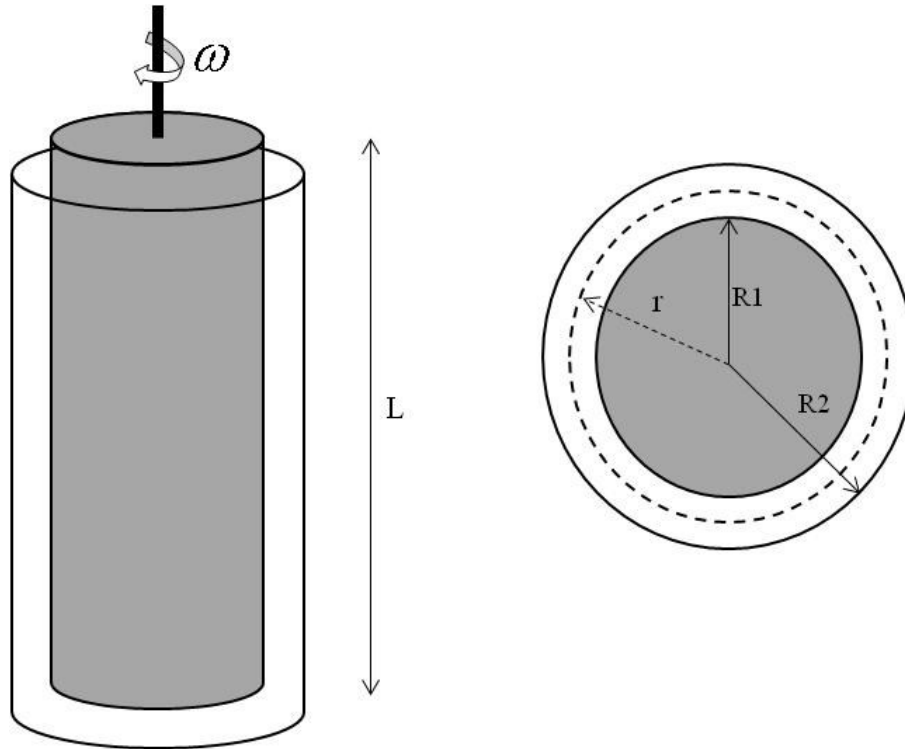


Figure 2.2 Schematic view of concentric cylinder apparatus

When the fluid is placed between two cylinders and fluid motion is induced by rotational movement of one of the cylinders, the torque at any surface a distance r from the center will be:

$$T = 2\pi r^2 \tau_{r\theta} L \quad (2.1)$$

If one considers a differential volume element defined by dr , it can be shown that for any radial surface the applied torque remains constant (Shook et al., 2002). As a result:

$$r^2 \tau_{r\theta} = \text{constant} \quad (2.2)$$

This even distribution of torque is an important constraint for testing a fluid with a yield stress. If the torque is not high enough, then $\tau_{r\theta} < \tau_y$ (where τ_y is the fluid

yield stress), some fluid in the gap adjacent to the cup wall (R_2) will be unsheared. For this reason a minimum torque must be provided to ensure the fluid in the gap is fully sheared. This limitation does not allow for measurements in low shear rate regions. In evaluating the problem of a sphere settling in a viscoplastic fluid, the shear rate of the fluid surrounding the falling particle is often low. Because of the aforementioned torque limitation, it may be that such low shear rates cannot be tested using a concentric cylinder viscometer.

The cone-and-plate geometry has an advantage over the concentric cylinder apparatus that is specifically important for tests of yield stress fluids. When a small cone angle is used and the fluid has negligible inertia, i.e. purely viscous flow, the shear rate (and shear stress) throughout the sample is uniform. This quality ensures the even shearing of the sample and therefore, cone-and-plate geometry is commonly selected for low shear rate measurements of yield stress fluids (Gumulya, 2009). Figure 2.3 shows a schematic illustration of a cone-and-plate rheometer.

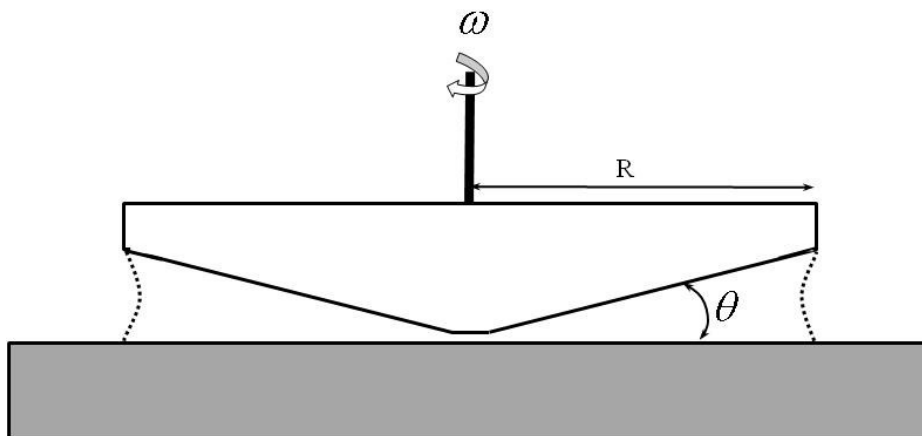


Figure 2.3 Schematic view of cone and plate geometry

For a cone-and-plate geometry, conversion of angular velocity and measured torque to shear rate and shear stress is possible using (AR-G2 manual)

$$\tau = \frac{1}{\frac{2}{3}\pi R^3} \times T \quad (2.3)$$

$$\dot{\gamma} = \frac{1}{\theta} \times \omega \quad (2.4)$$

2.2 Kaolinite-water suspensions

2.2.1 Origins of viscoplastic behavior

Clay particles have a high surface-to-mass ratio, meaning that when they are placed in water, a colloidal suspension is produced. In colloidal suspensions the particle-particle interactions are often modeled using the DLVO theory, which is a sum of the attractive van der Waals forces and repulsive electrostatic forces caused by charged surfaces of the particles (Masliyah et al., 2011). The relative magnitudes of these interactions determine the rheology of the mixture (Masliyah et al., 2011). Michaels and Bolger (1962), in a classic work, analyzed and characterized different types of particle-particle interactions in Kaolinite-water suspensions. They showed that if the attractive van der Waals forces are dominant, the particles attach to each other and form flocs. If the attractive forces are large enough, the flocs will form aggregates. Alternatively, if repulsive electrostatic forces are dominant, particles remain dispersed (Masliyah et al. 2011).

Kaolinite particles are plate-like units which stack face to face to form a lattice crystal (Michaels and Bolger, 1962). When the Kaolinite particles are placed in water, the surface of these plates bears a negative charge, but the charge on the surface and

edges can change with the concentration of ions present in the mixture (Nasser and James, 2006). Based on the surface charge distribution of these particles, they can attach in various ways. Figure 2.4 shows different types of Kaolinite particle attachment, where different amounts of water are trapped within the structures. The network of attached particles and high volume of entrapped water are primarily responsible for producing the yield stress associated with Kaolinite-water suspensions.

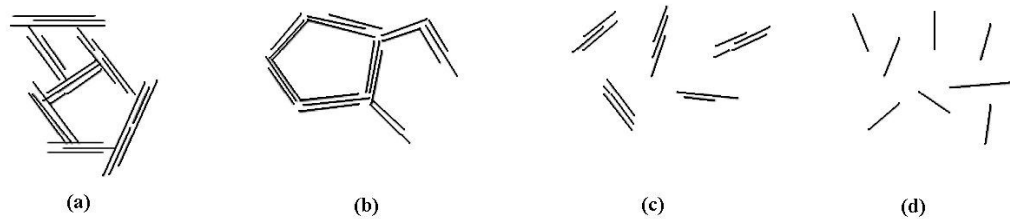


Figure 2.4 Different types of particle attachment in Kaolinite-water suspensions, (a) edge to face flocculated and aggregated, (b) edge to edge flocculated and aggregated, (c) face to face floccs not aggregated, (d) fully dispersed (van Olphen, 1977)

Litzenberger and Sumner (2004) investigated rheological behavior of concentrated Kaolinite-water suspensions, and showed that both Bingham and Casson models can be used to predict accurately (i) the mixture rheology over shear rate ranges relevant to pipeline transport, (ii) laminar flow curves of wall shear stress as a function of nominal shear rate ($8\bar{U}/D$) and (iii) the laminar-to-turbulent transition velocity. Therefore, in the present study, rheograms obtained for each mixture were fit using

the Bingham and Casson models. The results, and the implications for the prediction of terminal settling velocity of particles in viscoplastic fluids, are described subsequently. Figure 2.5 shows the rheogram of a Kaolinite-water mixture modeled using both Casson and Bingham models.

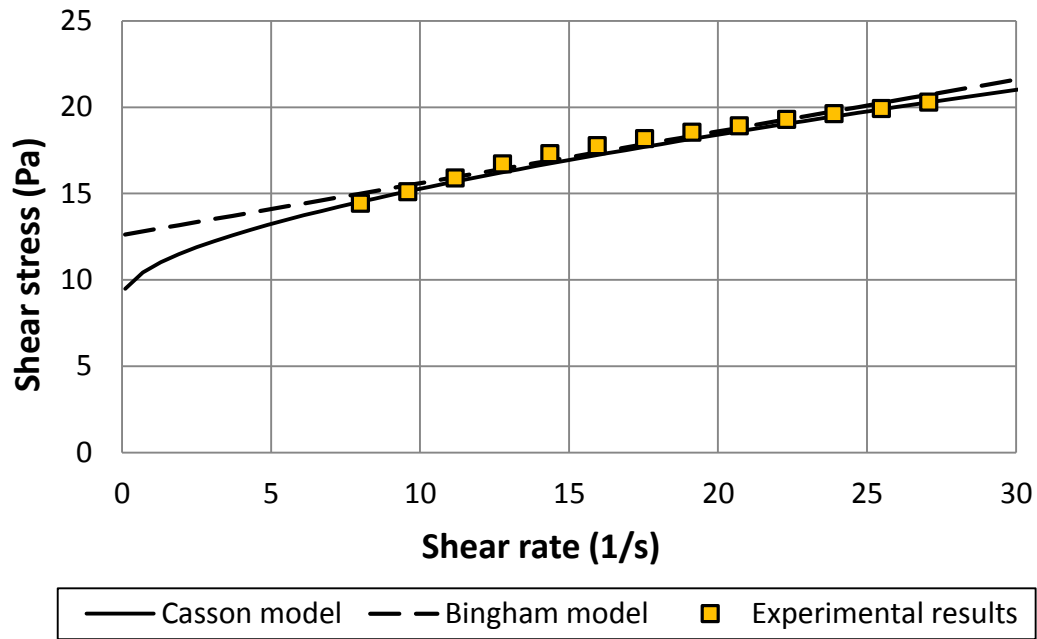


Figure 2.5 Casson and Bingham models fit to the same Kaolinite-water mixture ($C_v=12.2\%$) rheometry measurements

2.2.2 Shear sensitivity

When Kaolinite-water mixtures are produced, the flocs form an initial type of structure. If the mixture is then sheared, the flocs rearrange themselves in response to the flow. The rearrangement of the structure continues until ultimately it reaches an equilibrium condition. The rheological properties of the mixture at equilibrium

depend on two parameters; the shearing rate and the exposure time to shear (Schaan et al. 2004).

Shear sensitivity can be detected by online torque measurements taken during shearing. Schaan et al. (2004) have shown that the minimum time required to reach an equilibrium state is a function of shear rate in mixing process; higher shear rates can take the mixture to equilibrium more rapidly.

After shearing ceases the links between the flocs are re-established primarily through Brownian motion and particle collision (van Olphen, 1977). This effect causes the yield stress to increase with time when the mixture is left at rest. Thixotropic effects can dramatically change the properties of viscoplastic fluids once they are no longer exposed to shear (Nguyen and Boger, 1997).

In the study of the particle settling process, one must be aware that the particle “builds” a path by breaking the links between flocs during its fall (Hariharaputhiran et al. 1998; Gumulya 2009). The broken “links” may re-attach immediately or may take a long time to recover depending on the mechanism of attachments and the particles involved. Figure 2.6 shows the difference in fall velocities of two spheres falling through a yield stress fluid, where the second sphere is released 2 seconds after the first. Note that the image of the second sphere is distorted due to its higher velocity.

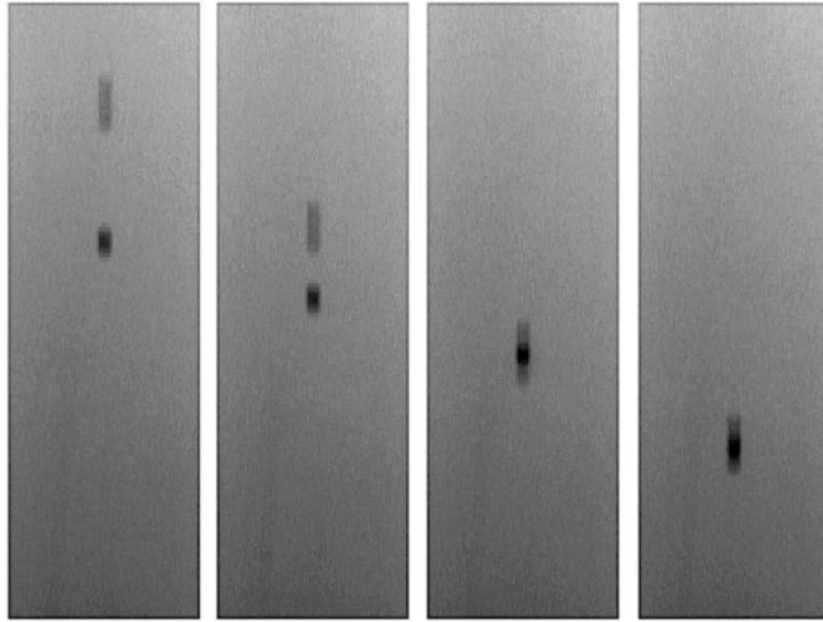


Figure 2.6 Two vertically aligned identical bronze spheres (7.94 mm diameter), released with 2 seconds delay, in 1.1% Floxite solution (Gumulya, 2009)

2.2.3 Determining yield stress

The magnitude of the mixture yield stress becomes especially important when it comes to the problem of settling particles. In order to compare the downward gravity force of a falling sphere to the upward resistance forces -buoyancy and yield stress- a dimensionless number is commonly used:

$$Y_G = \frac{\tau_y}{dg(\rho_s - \rho_f)} \quad (2.5)$$

The question of whether a sphere would or would not settle in an unsheared viscoplastic medium has attracted attention in the literature. For example, Boardman and Whitmore (1961), Ansley and Smith (1967), Beris et al. (1985) and Chafe and de Bruyn (2005) have used Bingham fluids and reported a range between 0.048 to 0.2

for maximum Y_G as a necessary condition for the sphere to move, while others like Uhlherr (1986) and Atapattu (1989) have used vane yield stress measurements as a basis for their analysis and reported different values. Part of the disagreement of results is due to different methods used by researchers to determine the yield stress of the mixture. As was mentioned earlier, the yield stress obtained from a viscoplastic rheology model is a fitting parameter and can vary significantly depending on the method used. Figure 2.5 shows the difference between τ_B and τ_C for the same set of measurements. In this example, the Bingham model gives $\tau_B = 12.6$ Pa while the Casson model gives $\tau_C = 8.9$ Pa.

Another parameter that can affect the magnitude of the fitted yield stress is the technique used for the rheometry tests. Measurements must be made over the relevant shear rate range when working with viscoplastic fluids such as Kaolinite-water mixtures. Figure 2.7 shows the rheogram of the same suspension from cone-and-plate and concentric cylinder rheometry. The requirement to ensure $\tau|_{R2} \geq \tau_y$ during concentric cylinder rheometry tests of viscoplastic fluids means that the “typical” shear rate range for this geometry is $\sim 20\text{-}200$ s⁻¹. Note how the results of the two rheometry tests shown in Figure 2.7 produce substantially different yield stress values; $\tau_y = 6.1$ Pa for the cone-and-plate measurements, and $\tau_y = 17.9$ Pa for the concentric cylinder viscometer.

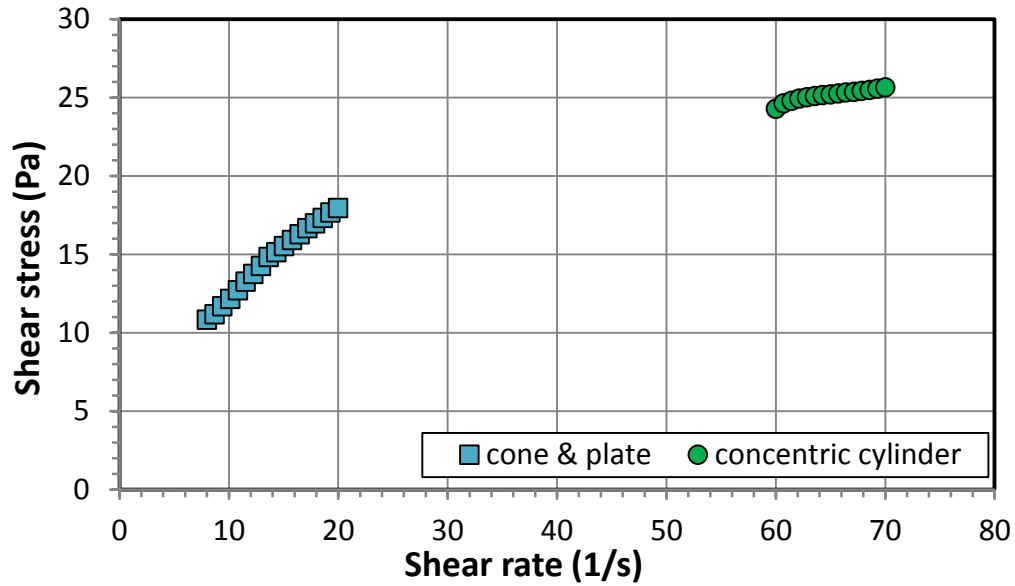


Figure 2.7 Rheograms of a Kaolinite-water sample ($C_v=15.8\%$) obtained with cone-and-plate and concentric cylinder geometries

2.3 Settling sphere in a fluid

2.3.1 Settling sphere in a Newtonian fluid

A particle falling in a Newtonian fluid is subjected to the forces of gravity, buoyancy, and drag. Particle motion may initially accelerate but since the drag force increases with velocity, at some point the net force becomes zero and the particle continues falling with a constant velocity. This velocity is referred to as the terminal settling velocity of the particle.

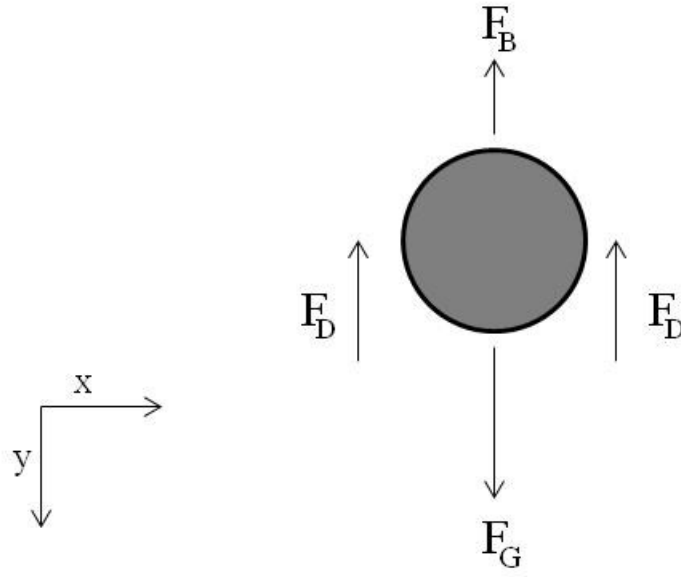


Figure 2.8 Schematic diagram of forces acting on a sphere falling in a Newtonian fluid

The force balance in the y-direction will be:

$$F_g - F_B - F_D = 0 \quad (2.6)$$

For a spherical particle, Equation (2.6) becomes:

$$\frac{1}{6}\pi d^3 \rho_s g - \frac{1}{6}\pi d^3 \rho_f g - F_D = 0 \quad (2.7)$$

The drag coefficient, sometimes defined as the dimensionless form of the drag force, is (Rhodes, 2008):

$$C_D = \frac{2F_D}{A_p \rho_f V_t^2} \quad (2.8)$$

where A_p is the projected area of the falling particle. By replacing Equation (2.8) in

Equation (2.7) and considering A_p for a sphere to be $\frac{1}{4}\pi d^2$, we have:

$$C_D = \frac{4(\rho_s - \rho_f)dg}{3V_t^2 \rho_f} \quad (2.9)$$

For low particle Reynolds numbers, $Re_p < 0.3$ (Rhodes, 2008), Stokes (1851) showed that

$$C_D = \frac{24}{Re_p} \quad (2.10)$$

where the particle Reynolds number is

$$Re_p = \frac{d\rho_f V_t}{\mu} \quad (2.11)$$

As Re_p increases, correlations are used to predict the terminal settling velocity (and drag coefficient) of a single sphere. Many these correlations give C_D as a function of Re_p . As was shown in Equations (2.9) and (2.11), C_D and Re_p are both functions of velocity. Therefore, most of the correlations require a trial and error method to calculate terminal settling velocity. Figure 2.9 shows the standard $C_D - Re_p$ curve for a sphere falling in a Newtonian fluid.

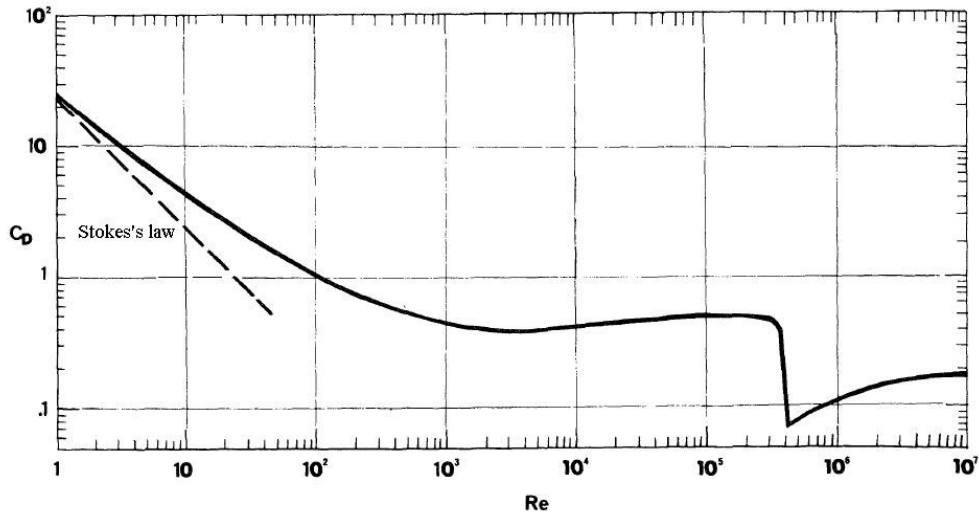


Figure 2.9 Standard drag curve for a sphere falling in a Newtonian fluid (Clift et al. 1978)

In order to provide direct predictions of terminal settling velocity of a sphere in a Newtonian fluid, Wilson et al. (2003) adopted the pipe flow analysis of Prandtl (1933) and Colebrook (1938) to develop a new set of equations based on shear velocity (V^*) and shear Reynolds number (Re^*).

In pipe flow, shear velocity (U^*) is the square root of the ratio of the shear stress at the pipe wall to the fluid density and shear Reynolds number (Re^*) is calculated based on U^* . One major difference between the pipe-flow analysis and the flow around a falling particle is that the stress distribution around the particle is not uniform (Wilson et al. 2003). In order to represent the characteristic shear stress of this process, the mean surficial stress ($\bar{\tau}$) of a falling particle was chosen, where $\bar{\tau}$ represents the immersed weight of the particle divided by its total surface area:

$$\bar{\tau} = \frac{dg(\rho_s - \rho_f)}{6} \quad (2.12)$$

Considering the definition of shear velocity (U^*), the parameter V^* for a settling particle will be:

$$V^* = \sqrt{\frac{\bar{\tau}}{\rho_f}} = \sqrt{\frac{dg(\rho_s - \rho_f)}{6\rho_f}} \quad (2.13)$$

The shear Reynolds number can be therefore written as:

$$Re^* = \frac{d\rho_f V^*}{\mu} \quad (2.14)$$

The authors then transformed the correlations and available experimental data in the literature from C_D versus Re_p to V_t/V^* versus Re^* , thereby producing a “new” standard curve for a sphere falling in a Newtonian fluid. This curve has three distinct regions as shown in Figure 2.10. In Region I, for $Re^* < 10$, the fitting equation is:

$$\frac{V_t}{V^*} = \frac{Re^*}{[3(1 + 0.08Re^{*1.2})]} + \frac{2.80}{[1 + 3.0 \times 10^4(Re^{*-3.2})]} \quad (2.15)$$

In Region II ($10 < Re^* < 260$),

$$\frac{V_t}{V^*} = 10^y \quad (2.16)$$

where

$$y = 0.2069 + 0.500x - 0.158x^{1.72} \quad (2.17)$$

$$x = \log\left(\frac{Re^*}{10}\right) \quad (2.18)$$

Region III ($Re^* > 260$) corresponds to particle Reynolds numbers larger than 1100, where the drag coefficient can be taken as approximately constant, at $C_D = 0.445$.

This corresponds to $\frac{v_t}{v^*} = 4.24$ in the direct method of Wilson et al. (2003).

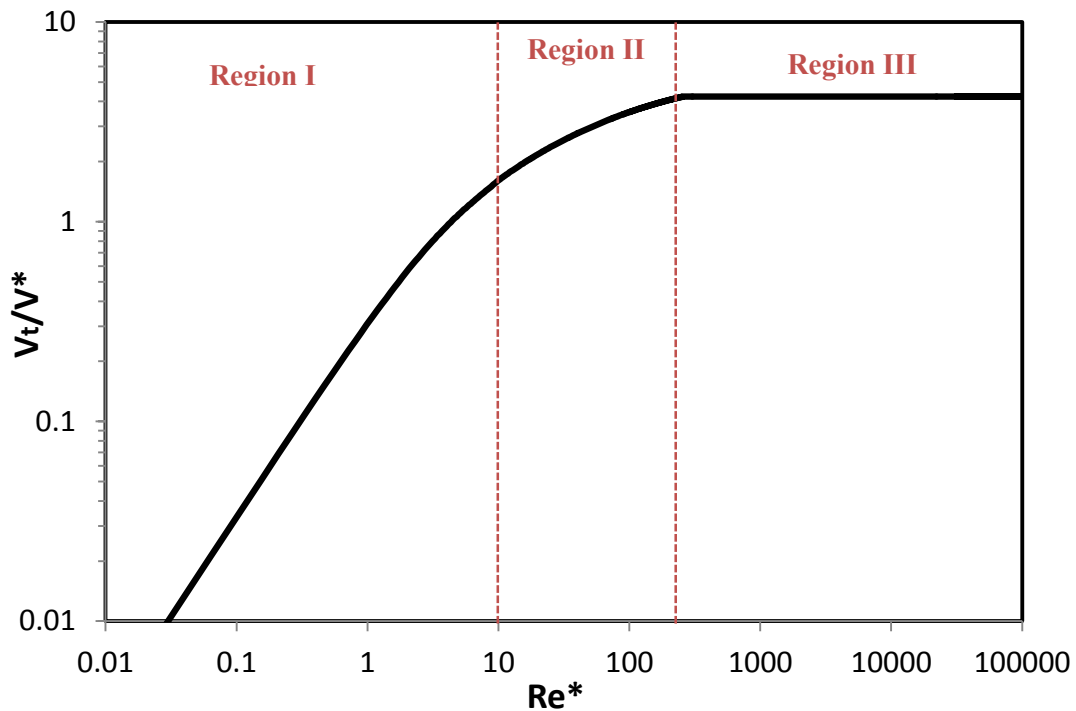


Figure 2.10 Standard curve for a sphere falling in a Newtonian fluid based on the Wilson et al. (2003) method (reproduced)

2.3.2 Settling sphere in a viscoplastic fluid

When a particle moves in a Newtonian fluid, the flow field around the particle theoretically expands to infinity. The shear stress exerted on the surrounding fluid around a falling particle decreases with distance from the particle surface and approaches zero at some location far from the particle. For viscoplastic fluids, the flow field is much different. If the applied shear stress falls below the yield stress, the

fluid acts as an elastic solid instead of a viscous material. For this reason, there are different zones in the fluid surrounding a falling particle.

Volarovich (1953) was among the first to postulate the existence of a sheared zone and an unsheared zone around the falling sphere in a viscoplastic medium. Later, Whitmore and Boardman (1962) suggested an “envelope” shape for the flow field around the particle. Ansley and Smith (1967) proposed a new shape for the flow field which was obtained based on slip line theory of solid mechanics. Beris et al. (1985) solved the problem numerically, limiting their analysis to creeping motion and using the assumption that the sheared zone boundaries are unknown. Blackery and Mitsoulis (1997) took a different numerical approach to solve the equations in both solid-like and fluid-like regions and thereby predict the location of the sheared zone boundary. Figure 2.11 shows different shapes of the sheared fluid region surrounding a falling particle, as suggested by different researchers. Note that the shape of the sheared fluid around the sphere suggested by Ansley and Smith (1967) comes from slip-line theory, the dimensions of the sheared zone by Yoshioka et al. (1971) come from stress and velocity variation principles, and Beris et al. (1985) used a numerical method for locating yielded/unyielded regions of a viscoplastic fluid around a falling sphere.

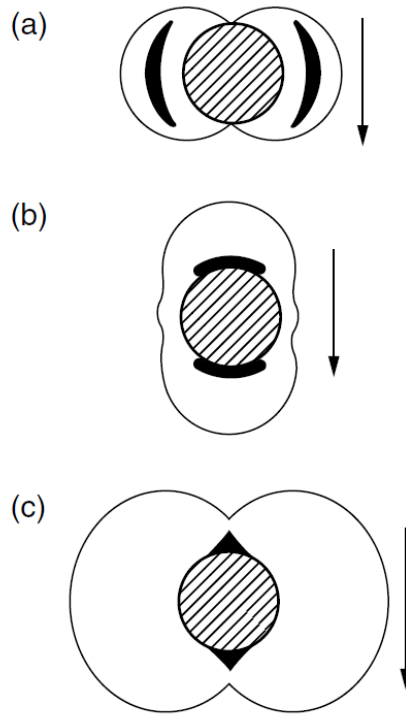


Figure 2.11 Shape of the sheared envelope surrounding a sphere in creeping motion in viscoplastic fluid: (a) Ansley and Smith (1967); (b) Yoshioka et al. (1971); (c) Beris et al. (1985), from Chhabra (2007)

The simulations by Beris et al. (1985), Blackery and Mitsoulis (1997) and more recently by Prashant and Derksen (2011) suggest that the size and shape of the sheared zone around a creeping sphere in a yield stress fluid strongly depend on the fluid's yield stress. Figure 2.12 shows the simulation results of Prashant and Derksen (2011) for a sphere falling in a square cylinder filled with a Bingham fluid. The Bingham number for these systems is defined as:

$$Bn = \frac{\tau_B d}{\mu_B V_t} \quad (2.19)$$

As the Bingham number increases, unyielded zones (shown by black spots) expand and shift closer to the particle surface. As a result, terminal settling velocity of the particle decreases dramatically with increase of fluid yield stress (Prashant and Derksen, 2011).

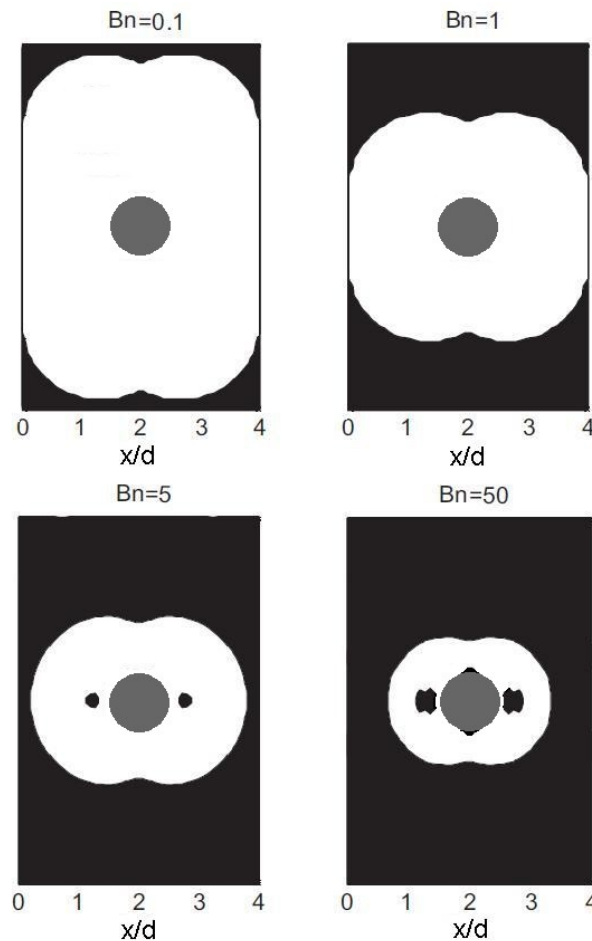


Figure 2.12 Yielded (white) and unyielded (black) regions for flow of a Bingham fluid around a fixed sphere contained in a square cylinder with $L/d=4$ (Prashant & Derksen, 2011)

Although the numerical simulations described above provide valuable information on the size and shape of the sheared region surrounding a falling particle, they suffer from one important constraint: the assumption of creeping motion. Therefore, on a

practical level, one must resort to empirical correlations to predict the drag coefficient (and particle fall velocity) for many scenarios.

The correlations can be divided into two different categories. The first category includes the methods that introduce dimensionless numbers based on fluid models (Bingham, Casson, and Herschel-Bulkley) and correlate C_D with these parameters. Andres (1961), du Plessis and Ansley (1967), Ansley and Smith (1967), Valentik and Whitmore (1965) have published notable studies in this category. In the second category, the definition of Reynolds number is modified in a way that the results of viscoplastic settling tests coincide with the standard Newtonian drag curve. Attapatu et al. (1995) and Chafe and du Bryan (2005) provide examples of this type of correlation.

While C_D is an important parameter, it has been proven to be particularly difficult to calculate V_t using these methods (Gumulya 2009), mainly because V_t emerges in both C_D and the modified Reynolds number and numerous iterations are required to obtain an acceptable estimate of V_t . Furthermore, the modified Reynolds numbers are commonly defined by “apparent viscosity” for viscoplastic fluids, which is a function of applied shear rate, which is a function of velocity itself. These complications reduce the chances of (a) convergence and (b) obtaining a reasonably accurate prediction of V_t .

The prediction methods of Ansley and Smith (1967) from the first category and Attapatu et al. (1995) from the second category are explained here so that the complexities associated with these trial-and-error methods can be illustrated.

Ansley and Smith (1967) postulated that the drag on a sphere falling in a viscoplastic medium consists of two contributions, the dynamic component of viscous stress and yield stress. They developed a dynamic parameter (Q) based on this assumption and modified its definition using slip-line theory:

$$Q = \frac{\rho_f V_t^2}{\left(\frac{\mu_B V_t}{d}\right) + \left(\frac{7\pi}{24} \tau_y\right)} \quad (2.20)$$

$$C_D = \frac{34}{Q} \quad \text{if } Q < 20 \quad (2.21)$$

$$C_D = 0.4 \quad \text{if } Q > 200 \quad (2.22)$$

Interestingly, no correlation is offered for $20 < Q < 200$. If $\tau_y \rightarrow 0$, the dynamic parameter (Q) reverts to the particle Reynolds number, but the standard Newtonian curve cannot be obtained. Figure 2.13 shows the drag curve presented initially by Ansley and Smith (1967), along with the standard Newtonian drag curve.

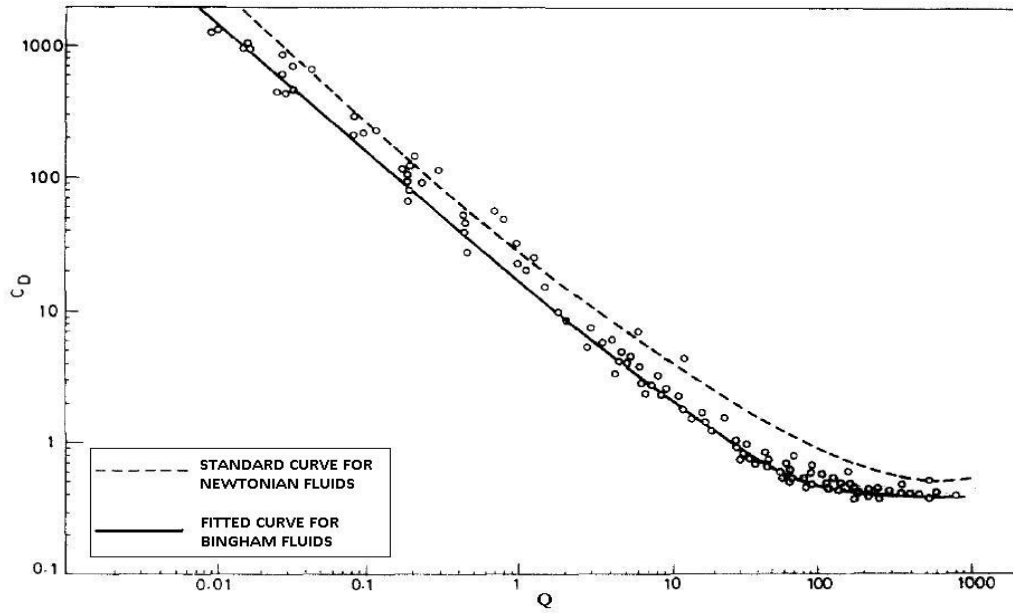


Figure 2.13 Drag curve presented by Ansley and Smith (1967) for a sphere falling in a Bingham fluid (from Saha et al. (1992))

Attapatu et al. (1995) extended the stress analysis of Ansley and Smith and developed a new method for predicting drag coefficient associated with a falling sphere in Carbopol solutions, which were modeled using the Herschel-Bulkley equation. A new dynamic parameter (Q^*) was defined to collapse the experimental data for non-Newtonian fluids on the standard Newtonian C_D - Re curve:

$$Q^* = \frac{Re^*_{HB}}{1 + 0.6143Bn^*} \quad (2.23)$$

where

$$Re^*_{HB} = \frac{V_t^{(2-n)} d^n \rho_f}{K} \quad (2.24)$$

$$Bn^* = \frac{\tau_y}{K(V_t/d)^n} \quad (2.25)$$

Figure 2.14 shows the performance of the method proposed by Attapattu et al.(1995).

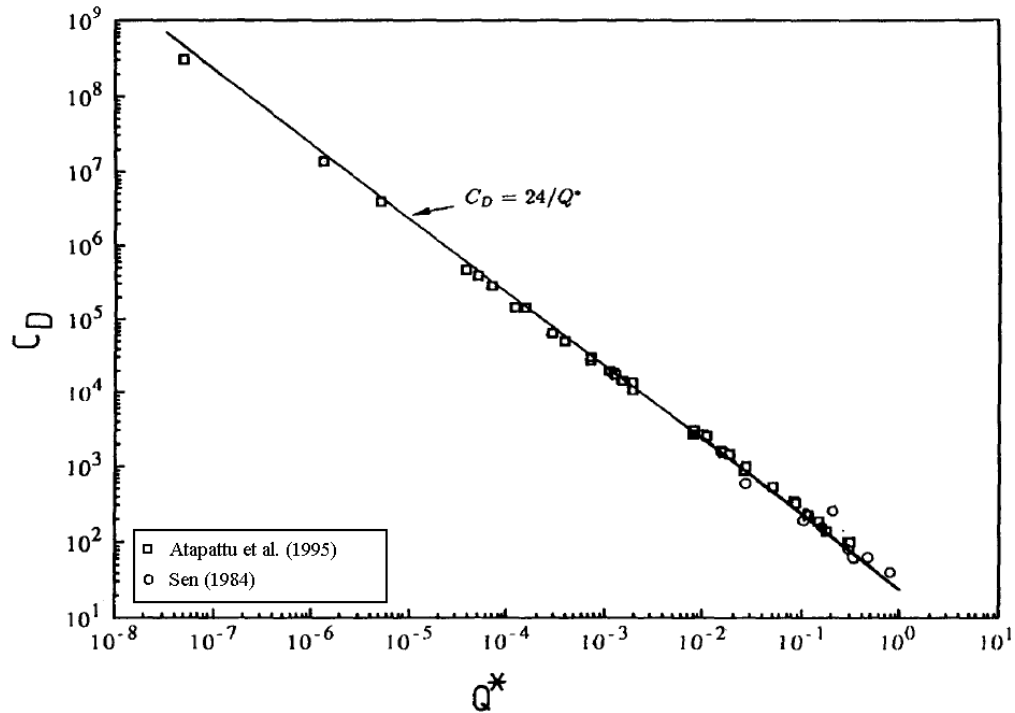


Figure 2.14 Overall performance of the correlation proposed by Atapattu et al. (1995) , from Atapattu et al. (1995)

Although this correlation does collapse onto the Stokes curve for Newtonian fluids when $n \rightarrow 1$ and $\tau_y \rightarrow 0$, it deviates from expected behavior of Bingham fluids when $n \rightarrow 1$. This correlation was developed based on experimental data from systems with $10^{-8} < Q^* < 0.3$ and the error in predictions increases dramatically for systems with $Q^* > 0.3$. For example consider the measured terminal settling velocity for the fluid-particle system shown in Table 2.2 initially reported by Gumulya (2009).

Table 2.2 Physical properties and measured terminal settling velocity for a sphere falling in a Herschel-Bulkley fluid, reported by Gumulya (2009)

d (m)	ρ_f (kg/m ³)	ρ_s (kg/m ³)	τ_{HB} (Pa)	K (Pa.s ^{n})	n	V_{tm} (m/s)
0.00635	998	8876	1.289	6.718	0.257	0.155

For $V_t = 0.155$ m/s, $Q^* = 1.49$. If one applies the correlation proposed by Attapatu et al. (1995) the predicted fall velocity will be $V_{tp} = 1.31$ m/s which is more than 8 times larger than the measured velocity. Another limitation of this method is that it can only be used for fluids with Herschel-Bulkley models.

Wilson et al. (2003) proposed a direct method for predicting terminal settling velocity of spheres in viscoplastic fluids, which provided V_t without iteration, but also utilized the standard Newtonian drag curve. An apparent viscosity is calculated from the fluid and particle properties and the terminal settling velocity is calculated for the sphere falling in a Newtonian fluid with that apparent viscosity. In order to find the proper apparent viscosity, the authors suggested a reference point on the fluid rheogram such that the equivalent Newtonian viscosity at that point can be used and thus the non-Newtonian settling data collapse on the Newtonian curve. The best reference point for more than 180 data points was found to be $0.3\bar{\tau}$, where $\bar{\tau}$ is the mean surficial stress of a falling sphere and can be calculated using Equation (2.12). This method provides good predictions for cases where $Re^* > 100$. In this region, ($Re^* > 100$) the average absolute error is 9.7% for 133 data points. Figure 2.15 shows the results of Wilson et al.'s method.

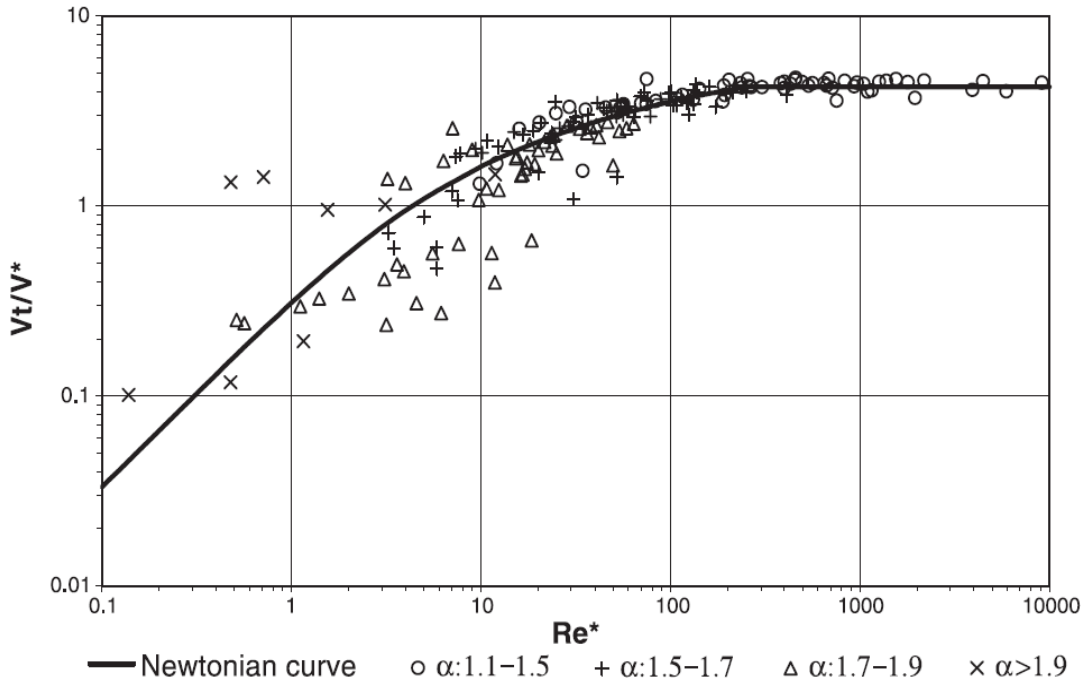


Figure 2.15 Experimental fall velocity measurements reported by Wilson et al. (2003, 2004) and shown on their standard Newtonian curve, with $\tau_{\text{ref}} = 0.3\bar{\tau}$

There are two important limitations associated with this method. The predictions for terminal settling velocity seem to deviate considerably from the Newtonian curve when $Re^* < 100$. The average absolute error for predictions in this region is 75% for 62 data points. The other limitation of this method is that if, for a particular fluid-particle system, the reference point of $0.3\bar{\tau}$ is less than yield stress of the fluid (τ_y), there are no points on the rheogram to choose as the reference point; without a reference point no apparent viscosity can be calculated and therefore no prediction of terminal settling velocity can be made. Because of this constraint, the Wilson et al. (2003) method is not universally applicable. The focus of the present study, as was

mentioned in Chapter 1, is to modify the Wilson et al. (2003) method to improve both the accuracy of predictions and the range of applicability.

2.4 Wall effects

2.4.1 Newtonian medium

When a particle falls in a fluid in the presence of solid boundaries, it reaches a stabilized velocity which is less than its terminal settling velocity in that fluid (Rhodes, 2008). From an analytical point of view, the containing walls change the boundary conditions needed to solve the equations of motion and the continuity equation for the continuous phase (Clift et al., 1978). The physical explanation for this phenomenon is that as the particle settles, an upward fluid displacement occurs. As the particle-to-container diameter ratio increases, the upward velocity of the fluid becomes significant (i.e. it can no longer be considered to be zero), which in turn increases the drag force acting on the particle; thus the terminal settling velocity of the particle is reduced. Figure 2.16 shows a schematic view of this mechanism. A good understanding of this phenomenon is crucial in the design of settling experiments and interpretation of results, and is therefore discussed in greater detail in the following paragraphs.

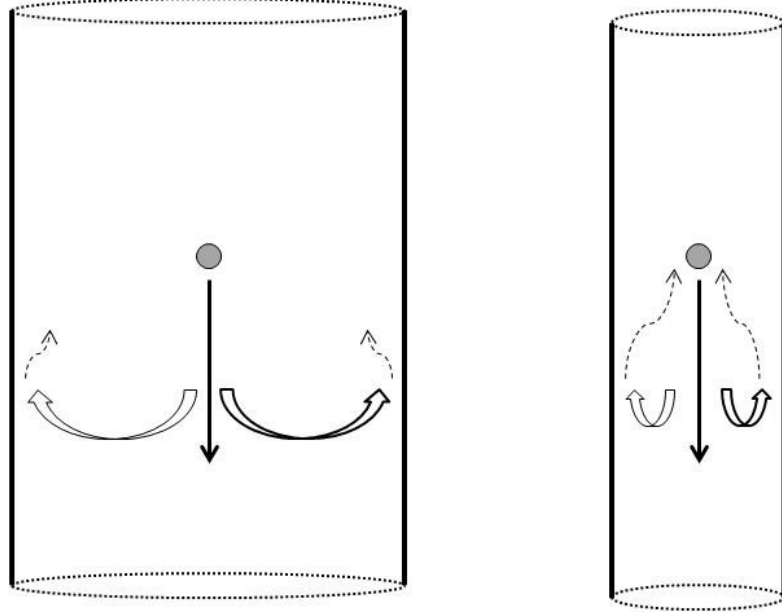


Figure 2.16 Schematic view of hindering effect of container boundaries on settling velocity of a single sphere in a Newtonian fluid

One can use a wall factor (f_w) to relate the measured particle settling velocity (V_m) to the velocity of the same particle in an unbounded medium, i.e. the terminal settling velocity (V_t):

$$f_w = \frac{V_m}{V_t} \quad (2.26)$$

Based on this definition, f_w can take a value between zero and unity. Other definitions of wall factor have been used in the literature, including the ratio of drag forces in bounded and unbounded media, the ratio of calculated viscosity using Stokes formula in finite and infinite mediums and $1/f_w$ (Chhabra, 2007). The velocity ratio as shown in Equation (2.26) has been chosen to calculate f_w by many researchers (Chhabra, 2007).

For a rigid sphere falling axially in an incompressible Newtonian fluid in a cylindrical tube, the wall factor f_w is function of particle Reynolds number (Re_p) and sphere-to-container diameter ratio ($\lambda = d_p/D$)(Chhabra et al., 2003).

There are numerous correlations available to predict the wall factor f_w for different ranges of both Re_p and λ . Chhabra et al. (2003) conducted an extensive review on methods used to predict f_w for the case of a single rigid sphere settling in a Newtonian fluid in a cylindrical container. Their review showed that at very low or very high Re_p , the wall factor is a function of λ only, while at intermediate Re_p , f_w is a function of both Re_p and λ . The limiting values of particle Reynolds number for each region (viscous, transition, and turbulent) are functions of sphere-to-container diameter ratio. Based on a statistical analysis of 1260 data points collected from several sources in the literature, Chhabra et al. (2003) selected the correlations which gave predictions with the lowest maximum and average error in each region. Table 2.3 shows the preferred correlations and the range of applicability for each region.

Table 2.3 Correlations for estimating wall effects for a particle settling in a Newtonian fluid (Chhabra et al., 2003)

Source	Correlation	Range of applicable Re
Haberman and Sayre (1958)	$f_w = \frac{1 - 2.105\lambda + 2.0865\lambda^3 - 1.7068\lambda^5 + 0.72603\lambda^6}{1 - 0.75857\lambda^5}$	$Re_p < 0.027$ for $\lambda = 0.1$ $Re_p < 0.04$ for $\lambda = 0.2$
(Di Felice, 1996)	$f_w = \left(\frac{1 - \lambda}{1 - 0.33\lambda}\right)^\varepsilon$ where $\varepsilon = \frac{3.3 + 0.085Re_p}{0.1Re_p + 1}$	$0.027 < Re_p < 60$ for $\lambda = 0.1$ $0.04 < Re_p < 110$ for $\lambda = 0.2$
Newton (1863)	$f_w = (1 - \lambda^2)(1 - 0.5\lambda^2)^{0.5}$	$Re_p > 60$ for $\lambda = 0.1$ $Re_p > 110$ for $\lambda = 0.2$

2.4.2 Viscoplastic medium

For viscoplastic fluids, wall effects cannot be described using the wall factors produced for Newtonian fluids, primarily because of the different flow field around the moving particle (Chhabra, 2007). As was discussed earlier, the sheared zone around the moving sphere has a finite radius and the fluid is undisturbed beyond that radius. If the sheared region of fluid does not extend to the container walls, then the measured terminal settling velocity will be equal to the “true” or unhindered settling velocity (Carreau et al., 1997).

Figure 2.17 shows a schematic view of the yielded and unyielded regions around a sphere falling in a tube filled with a viscoplastic fluid.

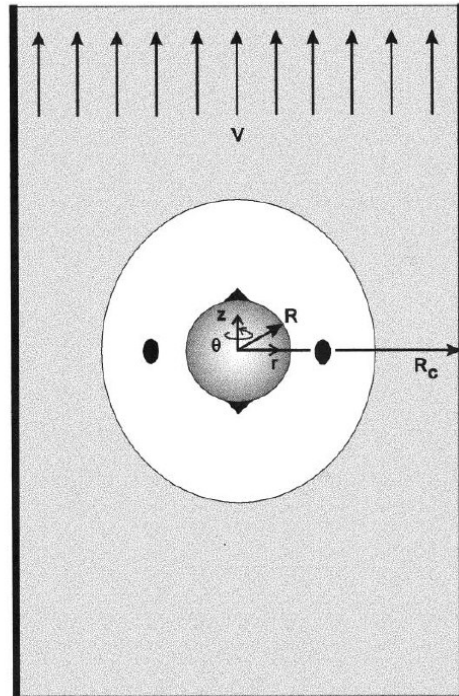


Figure 2.17 Schematic representation of the system of a sphere falling in a tube filled with a viscoplastic medium. Both the outer shaded regions and dark interior regions are unyielded (Beaulne and Mitsoulis, 1997)

Beaulne and Mitsoulis (1997) conducted finite element simulations to predict the size and shape of the sheared zone around a moving sphere in a Herschel-Bulkley fluid. The results were in good agreement with experimental results reported by Attapatu et al. (1995). Figure 2.18 shows the results of a series of simulations conducted to show a sphere of constant diameter falling in a Herschel-Bulkley fluid with constant properties. Only the particle density was varied in these simulations. The parameter Bn^* is calculated using Equation (2.25) and increases as the particle velocity decreases. Note how the sheared zone shrinks progressively as the particle velocity decreases.

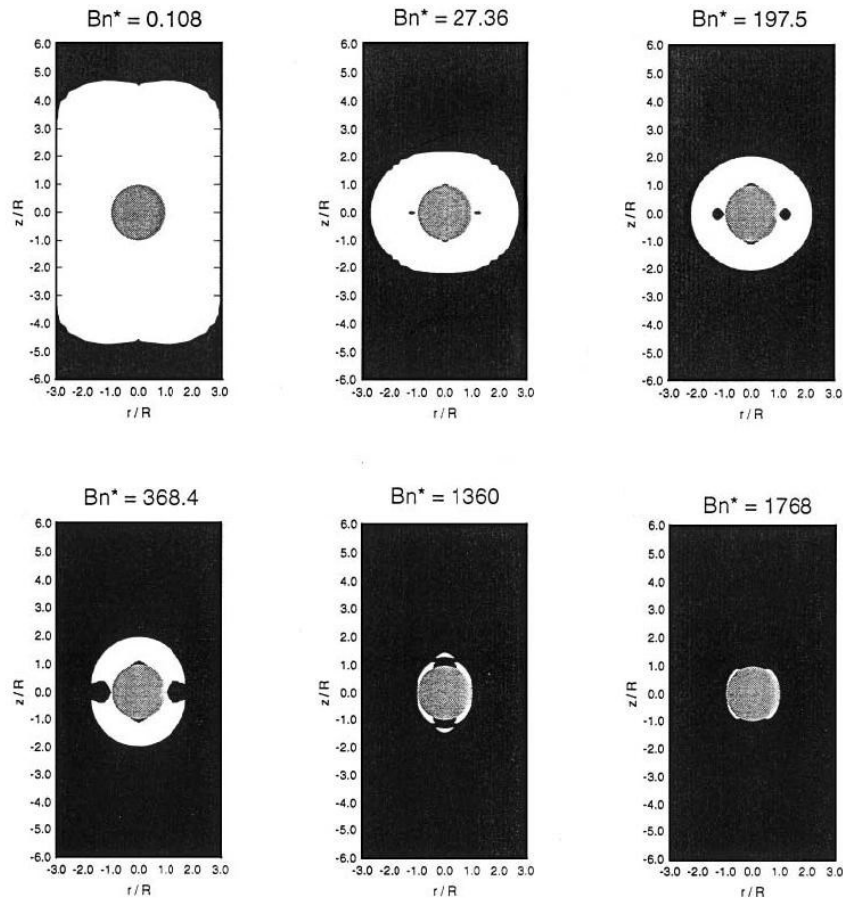


Figure 2.18 Size of the sheared zone around a particle moving at different velocities in a viscoplastic fluid ($\lambda=1/3$), from Beaulne and Mitsoulis (1997)

Chhabra (2007) conducted a comprehensive review of the investigations available in the literature to estimate the radius of the sheared zone around the particle. Experimental data and simulations for a wide range of system properties and geometries were collected. It was concluded from experimental studies such as those of Atapattu et al. (1990) and Atapattu et al. (1995) and from the simulations of Beris et al. (1985) and Beaulne and Mitsoulis (1997) that the extent of the sheared region radius is on the order of four times the sphere radius and decreases with decreasing

velocity. In a more recent study by Chafe and de Bryan (2005) a single sphere was pulled through different bentonite clay suspensions and the radius of the sheared zone was found to be twice the radius of the moving sphere in presence of significant wall effects ($\lambda = 6$).

Atapattu et al. (1986) proposed the following predictive expression for wall effects in viscoplastic fluids:

$$f_w = 1 \quad \text{if } \lambda < \lambda_{crit} \quad (2.27)$$

$$f_w = 1 - 1.7(\lambda - \lambda_{crit}) \quad \text{if } \lambda > \lambda_{crit} \quad (2.28)$$

$$\lambda_{crit} = 0.055 + 3.44Y_G \quad (2.29)$$

where Y_G is the yield-gravity parameter which can be calculated using Equation (2.5).

With the background provided in this chapter, one can conclude that a more comprehensive and accurate method is required for the prediction of a sphere's terminal settling velocity in a viscoplastic fluid. In order to develop an improved correlation that can cover a wider range of fluid-particle properties, it is critical to conduct high quality experiments. The experiments conducted as part of the present study are described in the following chapter.

3. Experimental method

3.1 Materials

3.1.1 Spheres

Several sizes of precision spheres made from different grades of steel, aluminum, and ceramic (Penn Ball Bearing Co, Inc.) were used for settling experiments. Spheres were reported to be smooth and have sphericity of more than 99%. The diameter was reported by supplier with accuracy of 0.1%. The density of each set of spheres was reported based on the grade of materials used. All the reported properties were measured and confirmed during this study. Physical properties of the spheres are listed in Table 3.1.

Table 3.1 Properties of the precision spheres used in the present study

Material	Density (kg/m ³)	Diameter (mm)
Aluminum	2710	12.7
Aluminum	2790	12.7
Aluminum	2790	15.9
Aluminum	2790	19
Ceramic	3925	12.7
Ceramic	3904	14
Ceramic	3950	14.3
Ceramic	3957	15.9
Ceramic	3940	19
Steel	7841	12.7
Steel	7684	14.3
Steel	7722	15.9
Steel	7675	17.5
Steel	7697	19

3.1.2 Kaolinite

It was established in Chapter 2 that Kaolinite is a type of clay, often found in mining operations and oil sands extraction, which can produce a viscoplastic fluid when mixed with water. The Kaolinite in this study was supplied by Kentucky-Tennessee Clay Company. According to the supplier, between 54% to 65% of particles have a mean diameter less than $2\ \mu\text{m}$, the density is $2650\ \text{kg/m}^3$, and the pH is 6.5.

3.1.3 Corn syrup

A solution of corn syrup and tap water was used as the Newtonian fluid for settling column calibration experiments. The corn syrup was provided by a local supplier (Bakers Supreme) and the density was measured to be $1371\ \text{kg/m}^3$.

3.2 Equipment

3.2.1 Settling column

A column with a circular cross section was used for settling experiments conducted as part of the present study. A schematic view of this setup is shown in Figure 3.1. The column is 1.5 m in length and 101.6 mm in diameter (i.d.). The settling column consists of four main sections. The acrylic transparent section provides visual access to a settling particle. The second section is used for Electrical Impedance Tomography (EIT) measurements and consists of two sets of sensors located 40cm from each other. At the very top part of the column, a frame, secured to the column itself, holds in place the vacuum tube guide, which is used to hold the vacuum tube in the dead-center of the column and just at the fluid free surface. The frame can be removed for cleaning or sample collecting purposes. At the bottom of the apparatus, a

series of valve arrangements, tubes and hoses connect a positive displacement pump (Masterflex variable speed, Model NO. RK-77111-60) to the column. The system is used to fill and drain the column and also to circulate the fluid when shearing is needed.

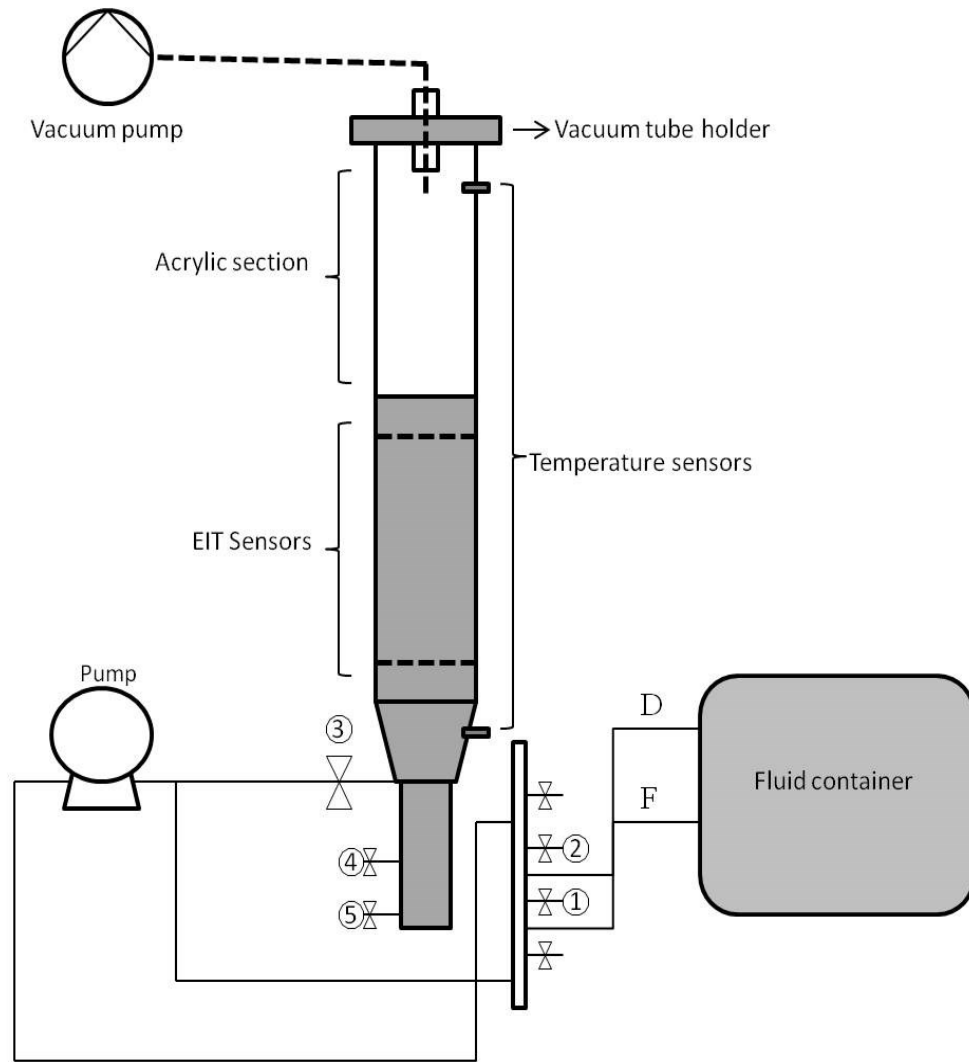


Figure 3.1 Schematic view of the settling apparatus

3.2.2 EIT sensors

The fall velocity of each particle tested in this study was measured using Electrical Impedance Tomography sensors. There are two rows of sensors located within 40 cm from each other and each row consists of 16 single electrodes arranged at equal spacing around the circular pipe. A current is provided from an external source for an initial pair of electrodes and the measured voltage from these two sensors and all the other ones in the same row is recorded. Then the same current is provided for a different pair and the same process is repeated. The recording of voltage responses continues until all the sensors are covered and a full rotation of voltage measurements is obtained. Each full set of voltage measurements, is translated to a full conductivity map of the fluid disk in contact with the sensors (Brown, 2003). The thickness of this disk is 5 mm and each full conductivity map is recorded as a “frame”.

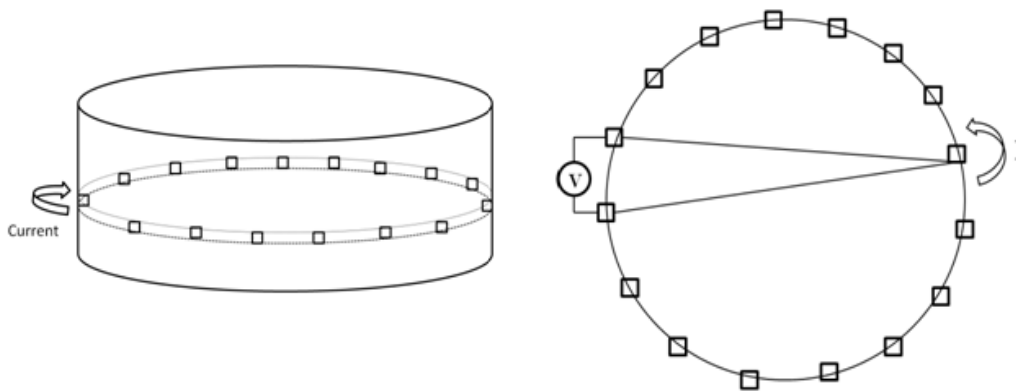


Figure 3.2 Side view (left) and top view (right) of EIT sensor electrode arrangements

The electrode sensors are connected to the EIT z8000, a high speed electrical impedance tomography data acquisition system, which can capture more than 1000 frames from 2×16 electrode sensors every second (z8000 EIT product sheet). The data collection speed in this study covered a large range from 10 fps for creeping particles to 825 fps for rapidly settling ones. The frequency of AC injecting current was set at 80 kHz.

The instrument collects the voltage measurements from the sensors and reconstructs the data to produce a conductivity map (Hashemi, 2013). The reconstruction grid is shown here as Figure 3.3.

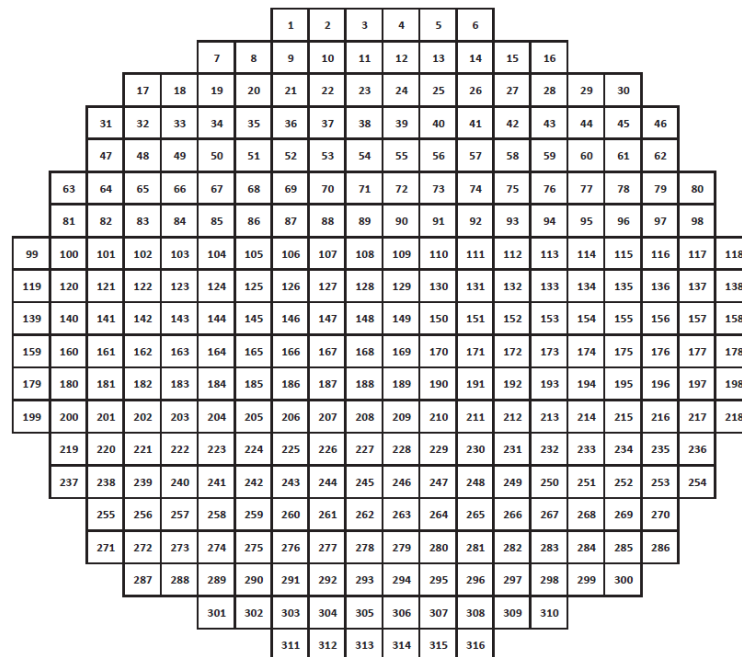


Figure 3.3 EIT reconstruction grids

When an object with a different conductivity relative to the reference medium fluid passes through, the conductivity in a series of pixels shown in Figure 3.3 changes. The average conductivity of each plane at any moment is assigned to the frame collected at that moment; therefore, by having a graph of average (plane) conductivity versus number of frames, the precise moment of particle arrival can be determined. Figure 3.4 shows the change in average conductivity caused by a passing aluminum sphere. Two high peaks on the graph show that the particle has a higher conductivity than the medium and by comparing the width of peaks it can be concluded that the velocity of particle has remained constant from the first plane to the second one. Figure 3.5 shows full conductivity maps of the first sensor plane, just before and just at the time the particle reaches the plane.

In this study, the exact arrival time of the particle to the first and second plane is observed, and the velocity is calculated by dividing the flight time of the particle by the distance between the two sensor planes (40 cm).

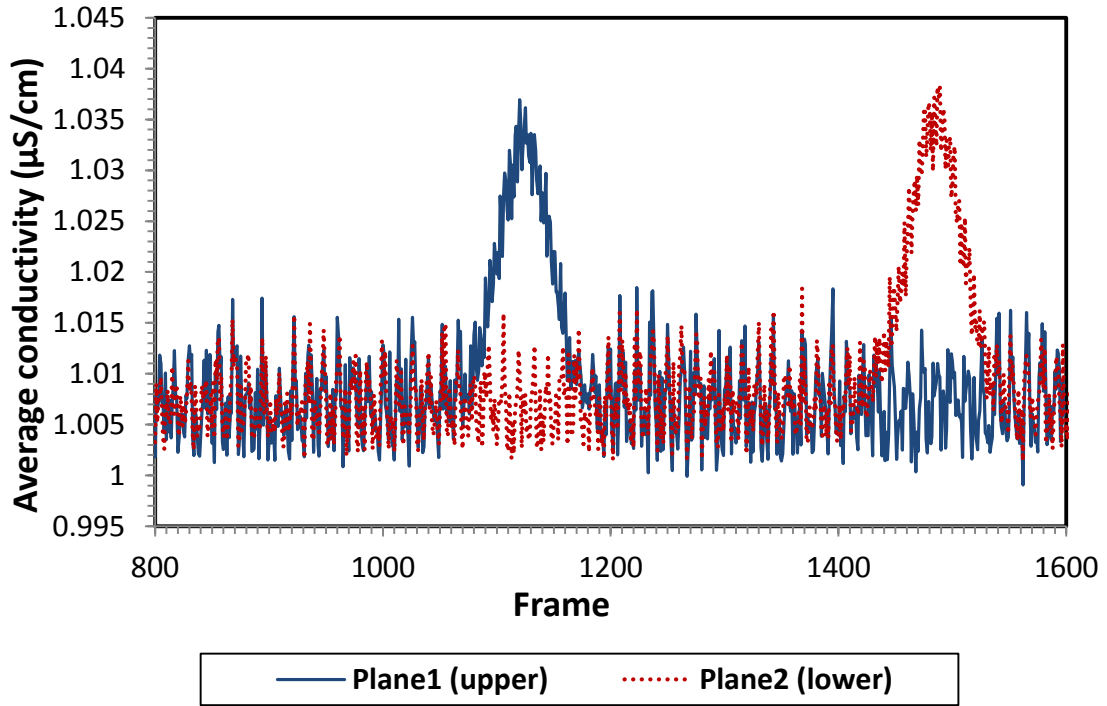


Figure 3.4 Typical conductivity measurements for two planes as an aluminum sphere passes through each plane; Data acquisition speed was 670 fps.

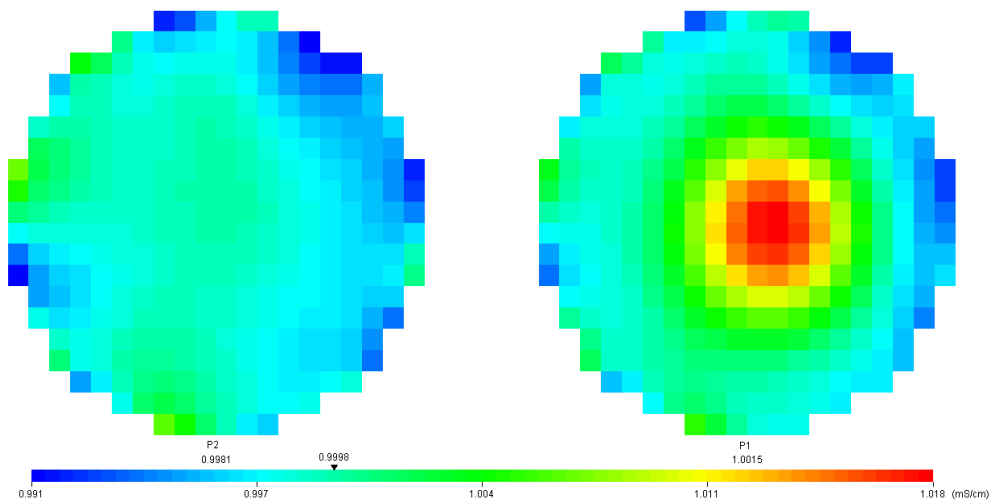


Figure 3.5 Reconstructed conductivity maps of aluminum sphere at the moment of arrival at the first plane (upper)

3.2.3 Releasing mechanism

A precise releasing mechanism was designed to drop each particle with minimum induced rotation or extra force. A schematic view of this system is shown in Figure 3.6. This mechanism consists of a vacuum tube, a vacuum tube holder, a vacuum pump, and a number of joints and elbows used to secure the location of different sections of the system. The vacuum pump is a small pressure/diaphragm pump (model NO. RK-07061-40) and provides suction to hold the particle in place at the tip of the tube. The vacuum tube holder is a rectangular frame with a cylinder tightened in the middle. This frame is bolted at the top of the settling column in a way that the axis of the cylinder in the middle matches the axis of the settling column. When performing settling tests, the particle is held at the tip of the vacuum tube by means of the vacuum pump, the vacuum tube runs down the cylinder, and is secured in a way that the particle is located right below the fluid surface. When the test is to begin, the particle is released by suddenly interrupting the vacuum. The detailed diagram of the apparatus is available in Appendix 6.

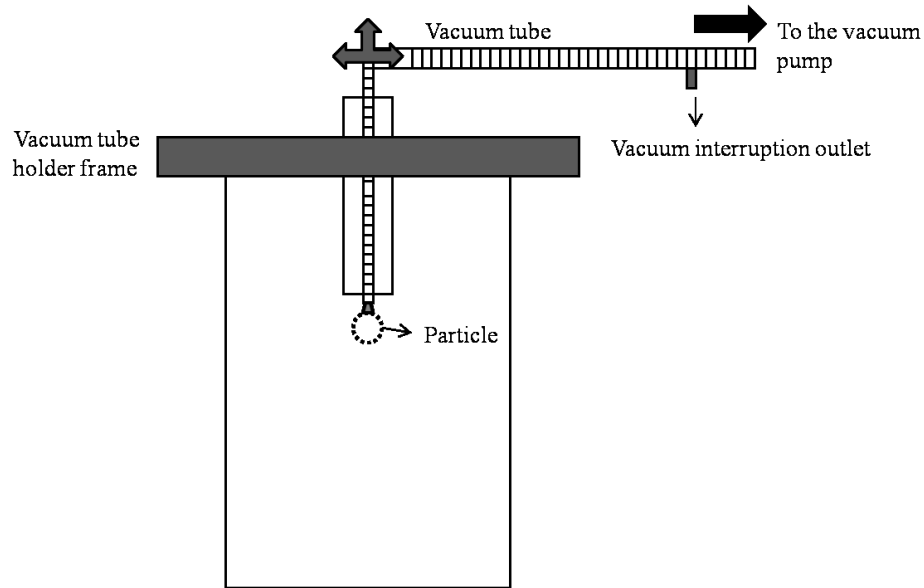


Figure 3.6 Schematic illustration of the releasing mechanism

3.2.4 Rheometer

All rheometry measurements were made using an ARG2 rheometer (TA instruments, New Castle, DE, USA). There are various types of geometries available for this instrument including concentric cylinder, cone and plate, and parallel plates. The combination of magnetically levitating mechanism with traditional air-bearing supposedly increases the accuracy of results in comparison to similar instruments. ARG2 can provide angular velocities between $1.4E-9$ rad/s to 300 rad/s and torques between $0.03 \mu\text{N}\cdot\text{m}$ to $200 \text{mN}\cdot\text{m}$ with a resolution of $0.1 \text{nN}\cdot\text{m}$. The rheometer is connected to a temperature control unit that utilizes deionized water as the circulating cooling fluid.

The cone and plate geometry is used for majority of rheology measurements in this study. The diameter of the cone is 60mm with an angle of 2.0 degrees. The tip of the

cone is truncated and a gap of 58 μm between the cone tip and the peltier plate is set before each experiment.

3.2.5 Mixer

A heavy duty mixer from the EUROSTAR series of IKA mixers (model NO. S-50705-30) was used to prepare Kaolinite-water mixtures. The overhead motor was able to provide a range of mixing speeds between 30 and 2000 rpm, a maximum torque of 60 N.cm, and a maximum input power of 0.19 hp.

A 3-blade axial flow impeller (Lightning A315) was used to stir the mixture. The approximate dimensions of the mixing apparatus are available in Appendix 6.

3.3 Procedures

3.3.1 Preparation of corn syrup solutions

The general procedure is as follows:

1. Weigh the required amount of tap water and place it in mixing container.
2. Start the mixer on 140 rpm.
3. Weigh the required amount of corn syrup and gradually add it to the solution. Increase the mixing velocity at each step to have a full vortex all the time.
4. Let the mixing continue for a minimum of 15 minutes after the last addition. Once the solution appears to be homogenous, stop the mixer and place the mixing container near the column.

3.3.2 Preparation of Kaolinite-water mixture

A standard procedure developed by Rahman (2011) was followed to prepare the Kaolinite-water mixtures. The purpose of this procedure is to first ensure the suspension is entirely homogenous, and then to eliminate or minimize the shear-dependent sensitivities of the suspension. The total volume of fluid required for the settling column is 17L.

The procedure is as follows:

1. Weigh the required amount of tap water and place it in the mixing container.
2. Adjust the impeller height so that the distance between the impeller tip and the bottom of the container is half the container diameter.
3. Start the mixer on the lowest mixing speed that produces a vortex at the center. For water, this mixing speed was 140 rpm.
4. Gradually add the required amount of Kaolinite to the mixture. A 500 mL beaker was used to weigh and add Kaolinite to the mixture in multiple steps. Increase the rpm after each step to get a full vortex.
5. Add required amount of $\text{CaCl}_2 \cdot 2\text{H}_2\text{O}$ such that $\text{CaCl}_2 \cdot 2\text{H}_2\text{O}$: Kaolinite (w/w) = 0.001.
6. Continue mixing at the minimum velocity that provides a full vortex for an hour.
7. Collect 3 mL of sample by means of a syringe for an early rheometry test.
8. If the rheological properties of the fluid are to be manipulated for the settling tests, use 0.25 M NaOH to adjust the pH. Continue mixing for an hour after the last addition step.

3.3.3 Fluid density measurements

The general procedure is as follows:

1. Use a syringe to collect a 10 ml sample of fluid for density measurements.
2. Ensure the pycnometer is completely dry. Record the weight of dry pycnometer (W_p).
3. Inject 10 ml of deionized water into the pycnometer and secure the thermometer at the top.
4. Dry the outer surface of pycnometer with a paper towel and record the weight (W_w).
5. Drain the pycnometer and repeat the same procedure (steps 2 to 4) for sample fluid ($W_{(p+s)}$).
6. Calculate the specific gravity of the sample fluid using:

$$SG = \frac{(W_{(p+s)} - W_{(p)})}{(W_w - W_{(p)})} \quad (3.1)$$

The density of the fluid can be calculated by multiplying SG by the density of deionized water at the temperature of the experiment.

3.3.4 EIT operation

In this study, a wide range of particle fall velocities between 3 mm/s to 1.8 m/s was measured. To guarantee that the z8000 system will be able to track the particle movement from the first sensor to the second, the proper data collection speed must be selected. For the calibration phase, the velocity of a sphere in a Newtonian fluid

was estimated using the Wilson et al. (2003) method. The arrival time of a chosen particle to each sensor was then calculated based on this estimation and the EIT data collection speed was set so that this time of flight could be easily tracked.

There are two categories for data collection on the z8000 instrument. The first category is an “offline” measurement which is suited for high speed data collection with higher sensitivity to conductivity change, and the second category is online measurement which is more appropriate for lower velocities. In the z8000 operating software, there are two parameters that manipulate measurement speed: “waiting time” controls the data collection speed for offline mode and “sample interval (ms)” manages the speed in online measurements. The total time required for a sphere to fall can be calculated and the measurement method/speed was selected to cover that time.

3.3.5 Settling tests

There is always a possibility for excessive humidity, rust or dust inside the column. To ensure that the fluid in the column is still homogenous, before filling the column for settling experiment, the new fluid will be circulated several times in the system. The procedure for performing a settling test on the settling column requires two operators. See Figure 3.1 for visual references. The general procedure is as follows:

1. Locate the filling tube (F) in the container.
2. In filling situation, Valves NO. 1, 4, 5 must be closed and Valve 3 should be open.
3. Set the pump speed on 3 rpm. Start the pump in forward direction.
4. Wait for the fluid to reach the top of the column and stop the pump when the fluid level has reached the mark on the top.

5. Wait for two minutes and inspect different parts of the setup to detect any possible leaks caused by loose joints.
6. Drain the column. Locate the draining tube in the container. In draining mode, Valves 4, 5 must be closed and 1, 2, 3 should be open.
7. Start the pump with the same speed (3 rpm) in reverse direction.
8. Repeat steps 5 to 12 three times. Then collect a 3 ml sample from the container for rheometry measurements.
9. Set the proper method/speed for EIT sensors.
10. Fill the column based the procedure explained in steps 1 to 5.
11. Close the Valve NO. 3. This valve connects the pump to the column. If it is left open the fluid will return to the fluid container.
12. Start the vacuum pump and Operator 1 climbs the ladder with desired spheres.
13. Operator 1 places the sphere at the tip of the vacuum tube and secures it on the holder frame.
14. Operator 2 starts the EIT, performs the basic calibrations and takes reference measurements.
15. When everything is set, Operator 1 interrupts the vacuum system using the outlet. Operator 2, at the same time, starts acquiring data on the software.
16. During the settling, the trajectory of the sphere will be monitored by the operators. The settling experiment is repeated (at least four times) at identical conditions and an average of measured velocities are reported.
17. After obtaining at least four data points, the procedure will be repeated with a different sphere as needed.

3.3.6 Kaolinite-water suspension rheometry

It was concluded in Chapter 2 that the cone-and-plate geometry is appropriate for rheometry measurements on Kaolinite-water mixtures at low shear rates. At different times during the settling experiments, 3 mL samples of fluid were collected from top and bottom of the column by means of a syringe and tested to ensure rheology properties of the fluid are stable. The procedure for low shear rheometry with the AR-G2 rheometer is as follows:

1. Before each test, it is crucial to provide enough air pressure to the motor to ensure that leveling, rotations and all the mechanical settings of the device can be properly controlled. The optimum pressure for this device is 30 psi.
2. Before turning the device on, any new geometry or locking piece should be detached. The moment the device starts, it attempts to recognize the geometry and reload the details from its library. If the geometry is new, it tries to perform zero gap and all other procedures to record the properties of this new piece. These procedures at this stage can damage the device since it cannot be stopped or controlled.
3. After the instrument is safely on and the spindle is rotating freely, the software can be started and connected to the device. From the software menu on the left “calibration” and on the top right the option of Instrument should be selected. The first option on the menu is “inertia”. At this point, no geometry should be attached. Inertia calibration takes about 30 seconds and at the end of it a single number is reported. This number should be around $18.8 \mu N \cdot m \cdot s^2$. The instrument uses this

as a correction factor for torque response measurements. It is recommended that this type of calibration is performed at least once every three months.

4. After inertia calibration, the chosen geometry should be attached. All geometries have a serial number written at the part where they are connected to the instrument. After attaching it to the device safely, “smart swap” option must be chosen. The geometry will rotate and the device will read the serial number and reload the information on the attached geometry from its library. After this, it is important to turn the smart swap off because the device keeps reading the serial number and reloading everything even during the tests.
5. The only control parameter here is the precision. For these tests, number of iterations was set on 2, as was advised by the training agent from the company. This calibration takes 10 minutes and it is recommended to be performed each time the geometry is detached and attached again. In this calibration, the device rotates the geometry with a large range of velocities and records the torque response of the geometry when no fluid is being tested. These torque responses produce a reference map for the device which is used to correct torque measurements.
6. After the rotational mapping is complete, “zero gap” calibration should be performed. In this type of calibration, the device lowers slowly and marks the point where the cone tip touches the plate. That reference point is used later to set the dimensions at which measurements are made. When this has been completed, the cone/spindle should be raised so that the rheometer can be loaded.

7. The last step before setting the specific procedure of the experiment is to set the temperature. To achieve best results in terms of temperature stability, the sample is loaded first and then the desired temperature is set. This allows the sample temperature to stabilize at the same time that the instrument temperature is being stabilized. For loading, 2 ml of fluid was collected by means of a syringe and put carefully at the center of the plate. From the environment menu the desired temperature can be entered now.
8. At this point all necessary calibrations have been performed and the device is ready to receive details of the desired experimental procedure. Two steps were defined for each test. The first step (conditioning) has two control parameters; temperature and soaking time. The temperature is inherited from the setting in step 7, and the soaking time was set to be 20 seconds.
9. The second step is the main test. There are several options available as control parameters. Spindle velocity was chosen. There are critical parameters that should be calculated before setting the test. The details of these calculations have been discussed in Chapter 2.
10. Start the experiment.
11. After the test is over, geometry should be raised to the “loading gap”, detached and washed. The data will be transferred to Excel sheets for analysis.

3.3.7 Additional shearing procedure for highly-concentrated suspensions

The procedure for shearing the non-Newtonian fluids inside the column is as follows:

1. Fill the column following Steps 1 to 4 as described in Section 3.3.5.
2. Relocate the container and attach tubes to the bottom of the column.
3. Open Valves NO.4, 5, 3, 2 and close the Valve NO.1.
4. Wait until the container is almost half full. Then start the pump with 3 rpm speed in forward direction. This way, the fluid is automatically circulated through the column. Let the pump run for 10 minutes.

4. Results and Discussion

4.1 Settling tests: Newtonian fluids

The first phase of this study includes measurement of terminal settling velocity of spheres in Newtonian fluids to calibrate the apparatus and develop the experimental methodology. The settling column and particles along with primary procedures for preparations have been introduced in the previous chapter. In order to produce repeatable results, there are several parameters that have to be carefully monitored and controlled during the experiment. As was mentioned in Chapter 2, terminal settling velocity is the stabilized velocity of a single particle, falling in a stagnant and infinite fluid. In order to ensure that the measured velocity of each sphere in the settling column is in fact “terminal settling velocity” of that particle in the fluid, two important conditions should apply:

- The particle should reach a constant velocity before measurement begins, which means that the observed velocity must be the same in both planes.
- The sphere must have a straight trajectory, and fall at the center of the column because the direct distance between two rows of sensors is used to calculate velocity. Also, if the sphere is closer to the wall at different locations along its trajectory, the wall effects will be important.

With the aim of designing the settling experiments such that these conditions are met, a series of calibration tests were conducted.

A solution of corn syrup-water was prepared and used as the Newtonian fluid and several spheres with different densities and diameters were used to perform settling

tests in low Reynolds numbers. For higher Reynolds numbers, tap water was used as the Newtonian fluid. As was mentioned in Chapter 3, each test was repeated at least four times and an average of recorded velocities was reported as the final result.

Transparency of corn syrup solutions and water made it possible to monitor the trajectory of the sphere and ensure a relatively straight falling path. The settling tests with visible inclined trajectories were discarded. In addition to that, the location of sphere in each EIT plane was checked to confirm the straight trajectory in non-transparent parts of the settling column. In cases where the sphere did not follow a straight path because of error in the releasing process, the experiment was repeated. Figure 4.1 shows examples of EIT results for settling tests with straight and angled trajectories.

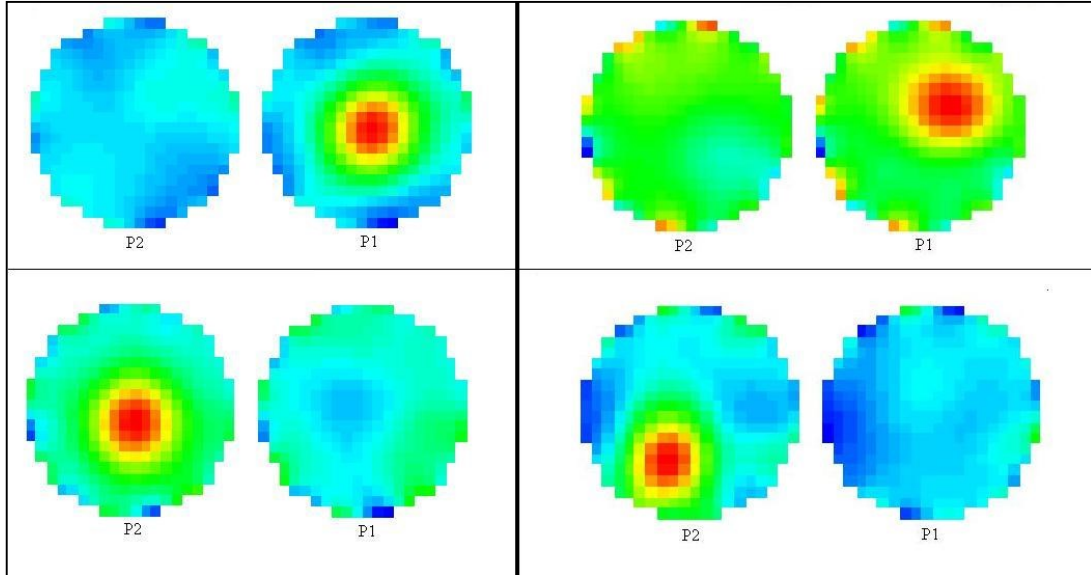


Figure 4.1 Sample conductivity maps for settling tests showing straight particle trajectory (left) and angled particle path (right)

The particle must also reach a steady state velocity before any measurement is made. In order to confirm the constancy of velocity at both measurement planes, the width of the conductivity interruption curves was compared; identical curves meant constant velocity. Figure 4.2 shows the conductivity curves for sphere (a) falling with constant velocity and sphere (b) which hasn't reached its stabilized settling velocity yet.

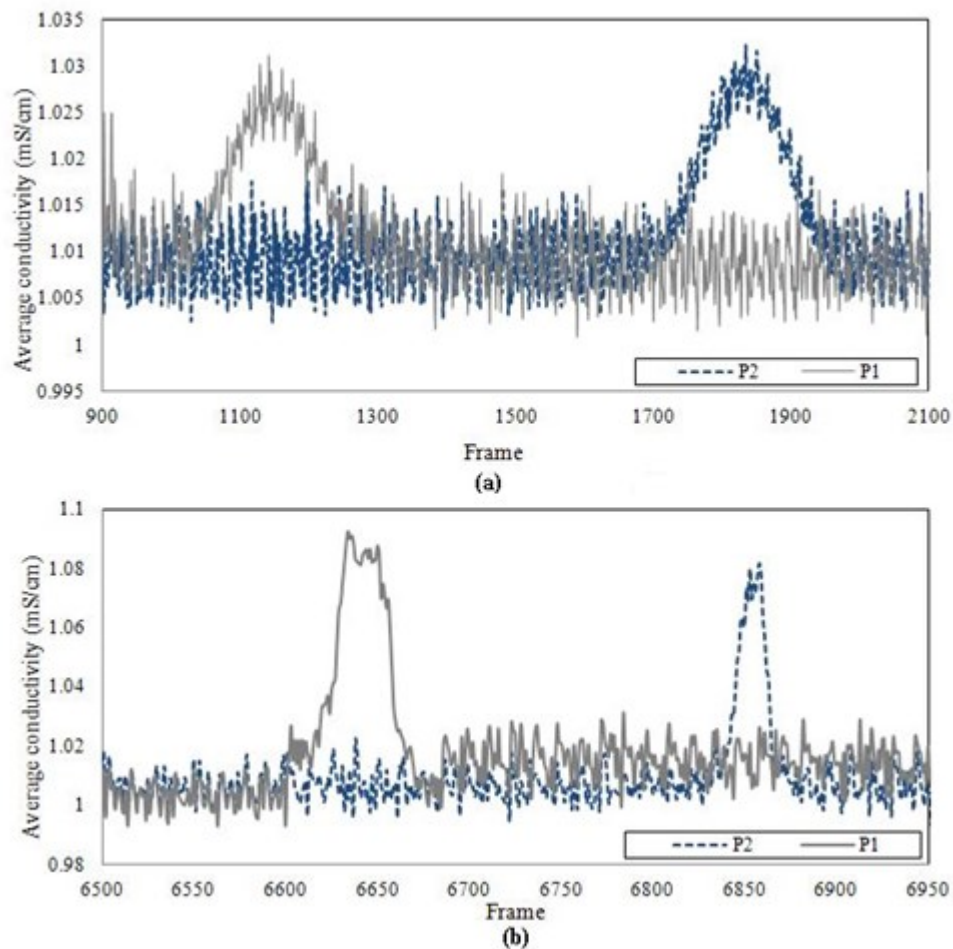


Figure 4.2 Sample of plane averaged conductivity measurements for settling tests with (a) a 12.7 mm aluminum sphere that has reached its terminal settling velocity and (b) an accelerating 12.7mm steel sphere

The wall effects for particles settling in Newtonian fluids were discussed in detail in Chapter 2. In order to account for wall effects in a series of calibration experiments, three correlations were selected based on the report by Chhabra et al. (2003). Reynolds numbers for these fluid-particle systems fall under the “intermediate” category in Chhabra et al.’s classification and the correlation proposed by Di Felice (1996) was selected to calculate f for each settling test. The system properties, velocity measurements, and the calculated correction factors for spheres falling in the corn syrup-water solution are shown in Table 4.1. The error in the last column has been calculated based on the corrected V_t and the predicted V_t from Wilson et al.’s direct method.

Table 4.1 Measured fall velocities for single spheres in corn syrup-water solution ($C_v=26\%$)

$d(m)$	ρ_f (kg/m^3)	ρ_s (kg/m^3)	μ ($Pa.s$)	V_{tm} (m/s)	Re_p	λ	f_w	V_{tm} (corrected) (m/s)	Error (%)
0.0127	1095	2710	0.267	0.22	11.47	0.13	0.82	0.244	9.00
0.0127	1095	2790	0.267	0.23	11.93	0.13	0.82	0.256	7.94
0.0127	1095	3925	0.267	0.34	17.75	0.13	0.84	0.381	6.65
0.0159	1095	2790	0.267	0.29	19.04	0.16	0.80	0.347	5.08
0.019	1095	2790	0.267	0.35	27.15	0.19	0.78	0.434	3.15
0.014	1095	3904	0.267	0.38	21.56	0.14	0.83	0.451	0.80
0.0143	1095	3950	0.267	0.39	22.71	0.14	0.83	0.480	2.11
0.0159	1095	3957	0.267	0.43	28.14	0.16	0.81	0.561	5.70
0.019	1095	3940	0.267	0.51	39.71	0.19	0.79	0.684	6.58
0.0127	1095	7841	0.267	0.65	33.71	0.13	0.86	0.779	2.97
0.0143	1095	7684	0.267	0.71	41.80	0.14	0.84	0.852	0.86
0.0159	1095	7722	0.267	0.79	51.57	0.16	0.84	0.944	0.38
0.0175	1095	7675	0.267	0.86	61.47	0.17	0.83	1.028	1.12
0.019	1095	7697	0.267	0.93	72.17	0.19	0.82	1.094	3.47

For settling tests in higher Reynolds numbers, tap water was used as the Newtonian fluid and the relationship proposed by Newton (1863) was used to correct the measured velocities. Table 4.2 shows the results of these settling experiments in water.

Table 4.2 Measured fall velocities for single spheres in water

$d(m)$	ρ_f (kg/m^3)	ρ_s (kg/m^3)	μ ($Pa.s$)	V_{tm} (m/s)	Re_p	λ	f_w	V_{tm} (corrected) (m/s)	Error (%)
0.0127	998	2710	0.001	0.78	9945	0.13	0.98	0.767	4.18
0.0127	998	2790	0.001	0.80	10175	0.13	0.98	0.782	4.46
0.0127	998	3925	0.001	1.03	13000	0.13	0.98	0.980	6.31
0.01588	998	2790	0.001	0.89	14070	0.16	0.97	0.915	0.08
0.019	998	2790	0.001	0.96	18160	0.19	0.96	1.011	1.00
0.014	998	3904	0.001	1.07	14930	0.14	0.98	1.107	1.11
0.01428	998	3950	0.001	1.09	15490	0.14	0.98	1.137	2.02
0.01588	998	3957	0.001	1.14	18080	0.16	0.97	1.210	2.84
0.019	998	3940	0.001	1.23	23270	0.19	0.96	1.329	3.59
0.0127	998	7841	0.001	1.57	19880	0.13	0.98	1.633	2.09
0.01428	998	7684	0.001	1.64	23310	0.14	0.98	1.718	2.48
0.01588	998	7722	0.001	1.72	27250	0.16	0.97	1.796	1.26
0.01746	998	7675	0.001	1.78	31100	0.17	0.97	1.833	1.10
0.019	998	7697	0.001	1.85	35120	0.19	0.96	1.884	2.72

Figure 4.3 shows the corrected terminal settling velocities on the standard Newtonian curve.

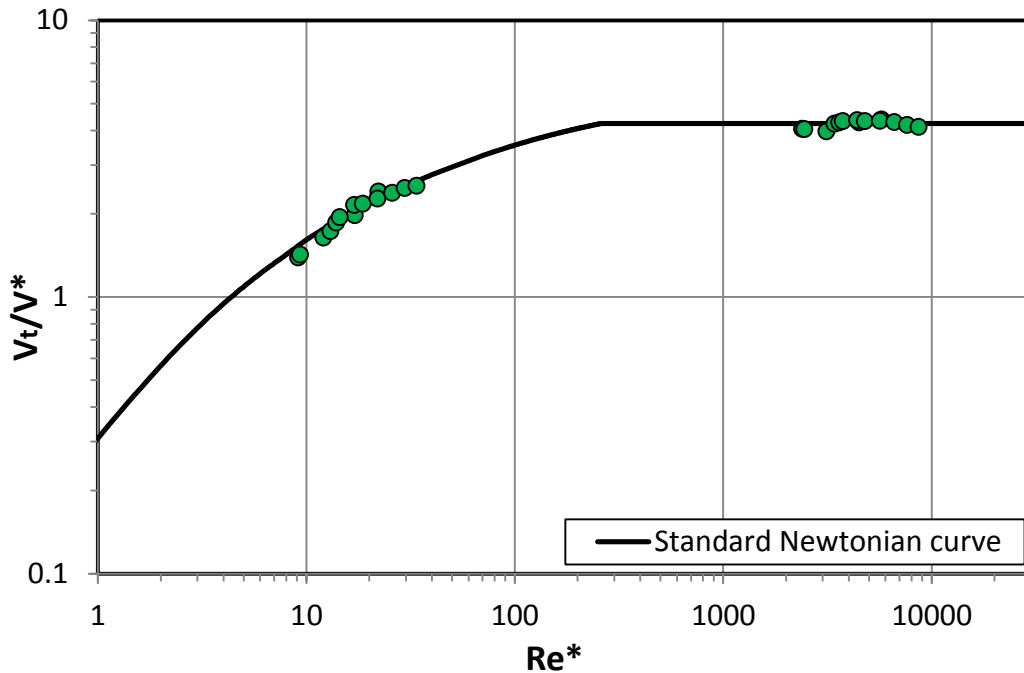


Figure 4.3 Terminal settling velocities corrected for wall effects; tests conducted with Newtonian fluids

4.2 Settling tests: Kaolinite-water suspensions

Settling experiments were performed on more than 100 different fluid-particle systems, using several different Kaolinite-water mixtures prepared based on the procedures explained in Chapter 3, along with 14 spheres with different sizes and densities. The yield-gravity parameter Y_G for fluid-particle systems in these experiments varied from 0.0058 to 0.073. The correlation proposed by Atapattu et al. (1986) for wall effect is based on the systems with $0.0091 < Y_G < 0.058$ and therefore covers a large portion of the experiments done in this study. Less than 13% of the

data points had the condition of $\lambda > \lambda_{crit}$ and according to Atapattu et al. (1986) were affected by the presence of the settling column (see Section 2.4.2). These data points were discarded.

The procedure for settling tests in non-Newtonian fluids is similar to the procedure followed for the Newtonian fluid tests. However, there are a number of considerations that have to be taken into consideration when working with viscoplastic fluids. As was explained in Chapter 2, the important feature of Kaolinite-water suspensions is the shear sensitivity. Rheological behavior of a viscoplastic fluid can be a strong function of two parameters; first, the shear rate it was exposed to before measurements, and second, the relaxation time after the shearing ceased. These sensitivities make it essential to have a very precise procedure for performing settling tests in viscoplastic fluids. In the experiments of the current study, “shear history” can change the properties of the fluid in two stages.

The first stage is the shearing during sample preparation and mixing. A series of shear-conditioning tests were performed in a previous study to develop a practical shearing condition to produce the most stable form of the Kaolinite-water mixture (Rahman, 2011). The results of that investigation were confirmed by additional experiments conducted during the present study. It was observed that after shearing the fluid for 30 minutes, the torque response was completely stable for suspensions with $C_V=10\% - 22\%$. A mixing time of 30 minutes was set as the minimum duration for mixing in the preparation step. Figure 4.4 shows the torque response of a mixture of 22% Kaolinite by volume versus time when sheared with an angular velocity of 20 rad/s.

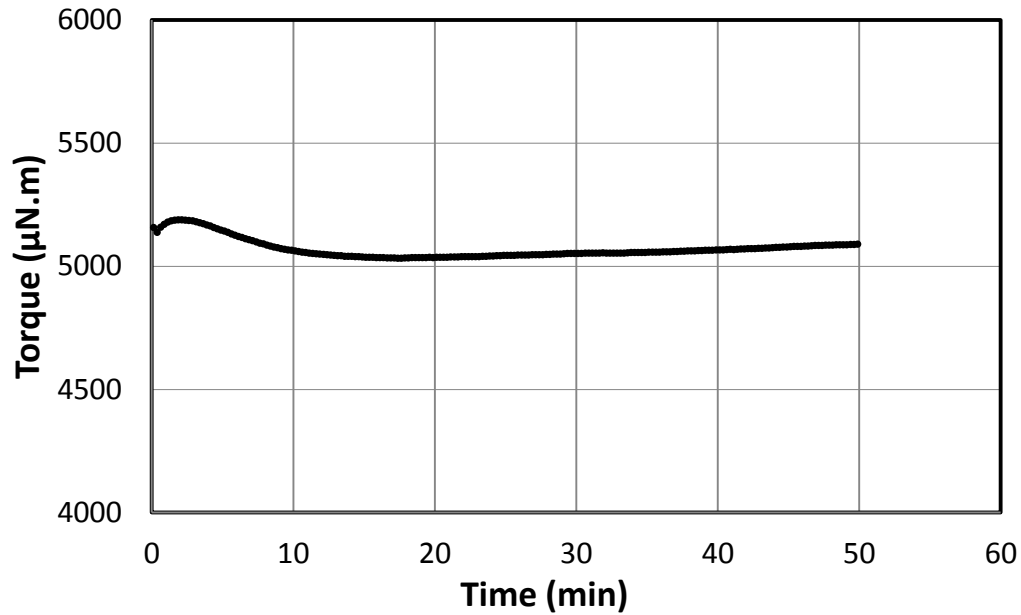


Figure 4.4 Time-dependent behavior for a Kaolinite-water suspension ($C_v=22\%$); cone-and-plate rheometer; $\omega=20$ rad/s

The second stage of shear sensitivity occurs during the settling tests. For viscoplastic fluids, it is extremely important to choose a waiting time to allow the fluid structure to recover after shearing (Gumulya, 2009). This shearing can be caused by the pump (when filling/draining the column) or a falling particle (during a settling test). To find the appropriate waiting time, a series of settling tests were conducted with different time intervals, and the minimum waiting time that could produce repeatable velocity measurements for identical fluid-particle systems was established. Figure 4.5 shows the measured velocity for a series of identical settling tests, performed with different waiting times. The waiting time was found to be 4 minutes for suspensions with $C_v = 10\% - 17\%$.

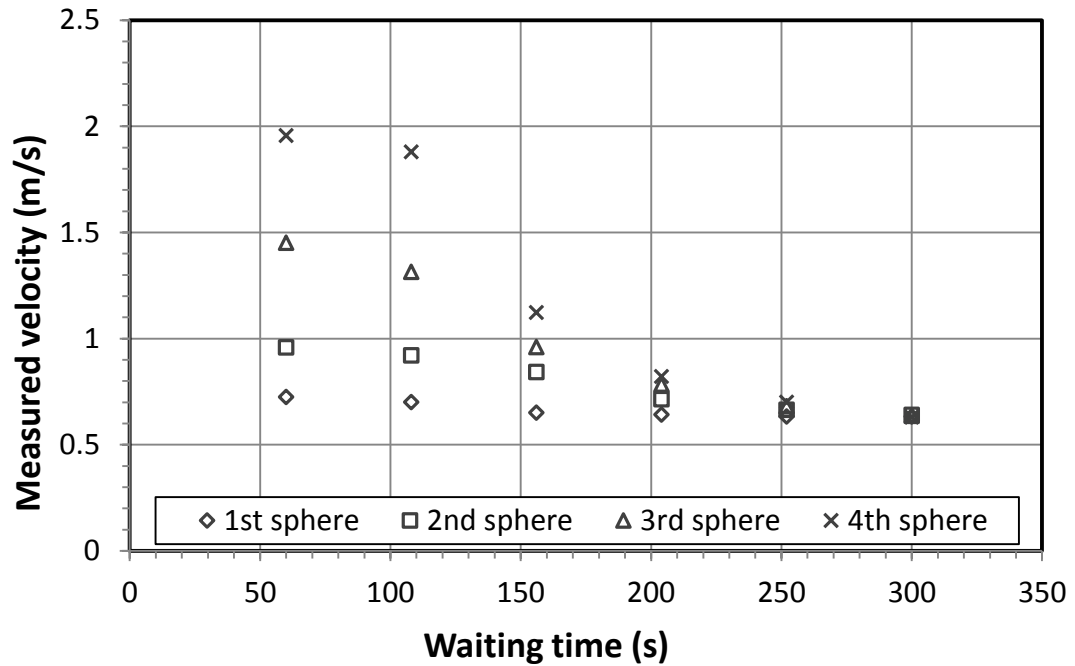


Figure 4.5 Settling velocity measurements for four identical 12.7 mm ceramic spheres released at different time intervals; 15.6% Kaolinite-water mixture

Figure 4.6 shows the velocity measurements made using a time interval of 4 minutes. Fluids with higher concentrations were so unstable that the only way to obtain repeatable results was to shear the fluid in the pump after each settling test and use the freshly mixed suspension. Figure 4.7 shows the measured velocity for a ceramic sphere in a 20.6% Kaolinite-suspension when the fluid was being sheared in between tests.

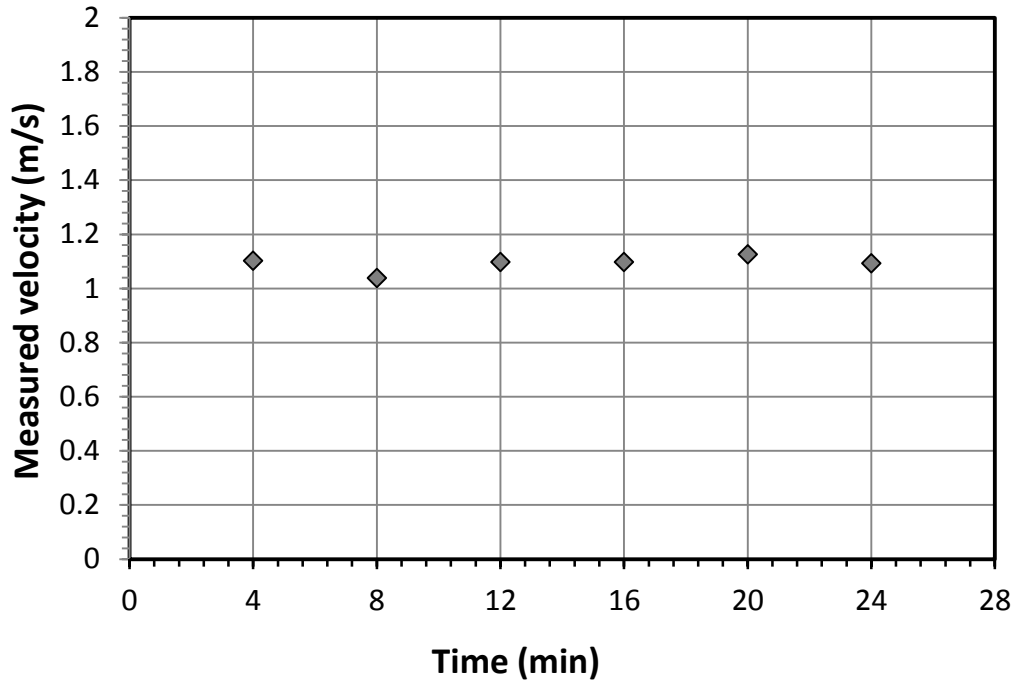


Figure 4.6 Settling velocity measurements for six identical steel spheres ($d=15.9$ mm) released at 4 minutes intervals; 16% Kaolinite-water mixture

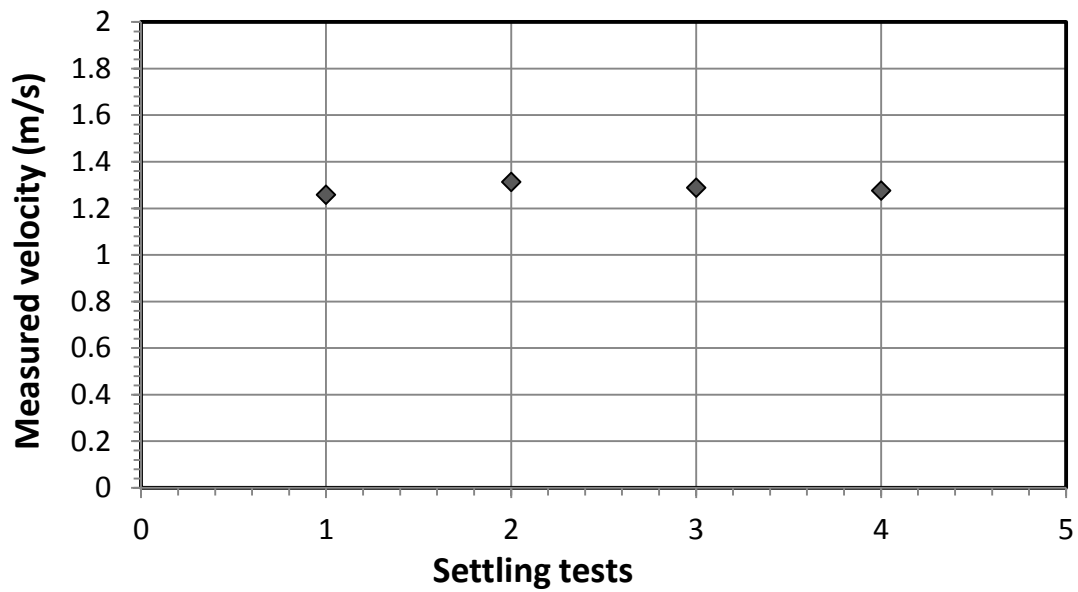


Figure 4.7 Settling velocity measurements for four identical steel spheres ($d=17.5$ mm) in 19.8% Kaolinite-water suspension; when the fluid was mixed before each individual test

During settling tests, fluid samples were collected from the column for rheometry tests to ensure the rheological properties of the fluid remained constant. Figure 4.8 shows the results of a typical set of rheometry measurements made for the same fluid during the settling experiments.

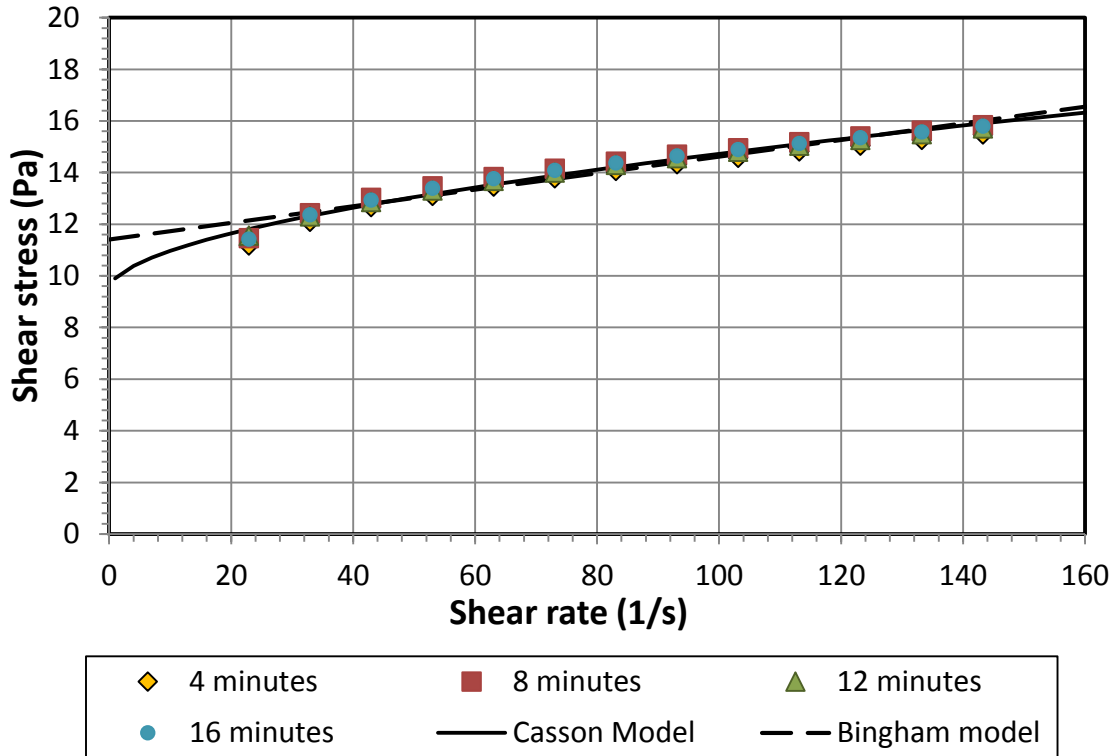


Figure 4.8 Rheometry measurements for a single Kaolinite-water suspension ($C_v=15.8\%$) made at 4 minutes intervals during settling tests

The rheogram of the fluid was then characterized with both Casson and Bingham models. Figures 4.8 and 4.9 show the fitted models on the rheogram of the Kaolinite-water suspension with $C_v = 15.8\%$ (Figure 4.8) and $C_v = 19.8\%$ (Figure 4.9).

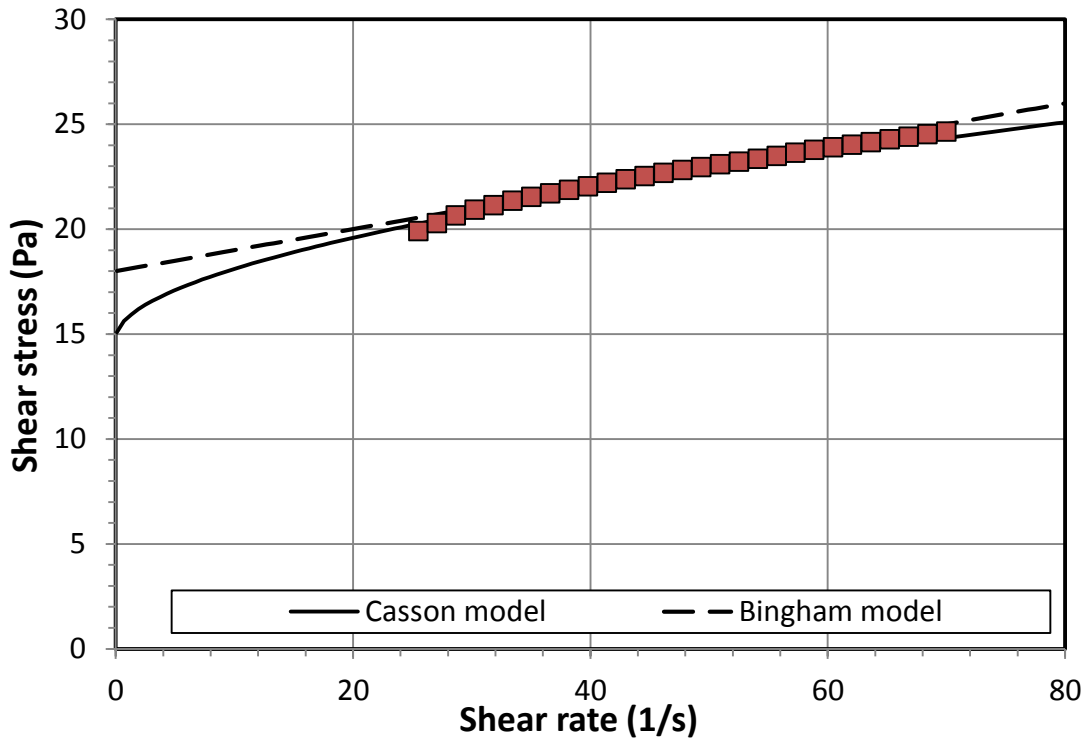


Figure 4.9 Casson and Bingham models fitted to rheogram of a Kaolinite-water suspension ($C_v=19.8\%$)

In experiments done in the present study, the rheogram of the fluid was fitted with both Casson and Bingham models and the shear Reynolds number was calculated with the apparent viscosity proposed in Wilson et al. (2003) method (with equivalent Newtonian viscosity at $\tau_{ref} = 0.3\bar{\tau}$). The shear Reynolds number is plotted versus the relative shear velocity in Figure 4.10 for the experimental results obtained in this research project. Ten of the data points from the present study could not be plotted in Figure 4.10 using the Wilson et al. (2003) method.

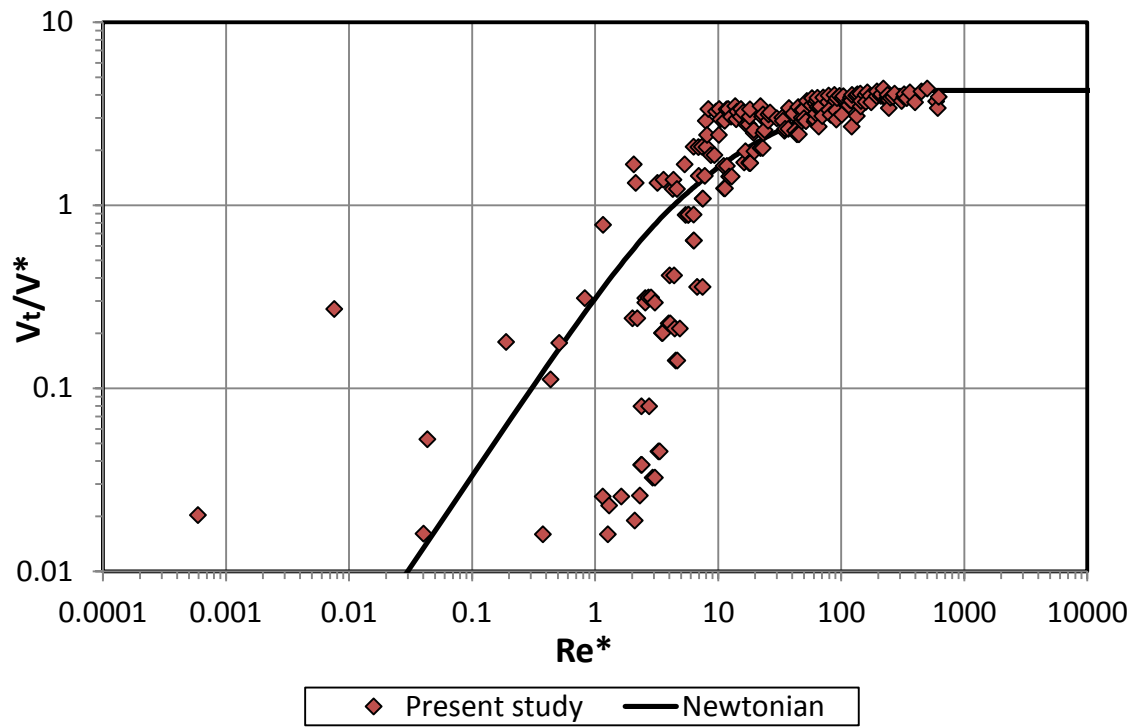


Figure 4.10 Experimental results from current study plotted by Wilson et al. (2003) method

4.3 Analysis of Wilson et al. (2003) direct method

Figure 4.11 compares the velocity predicted by the Wilson et al. (2003) method with the measured velocities for experimental results obtained in this study.

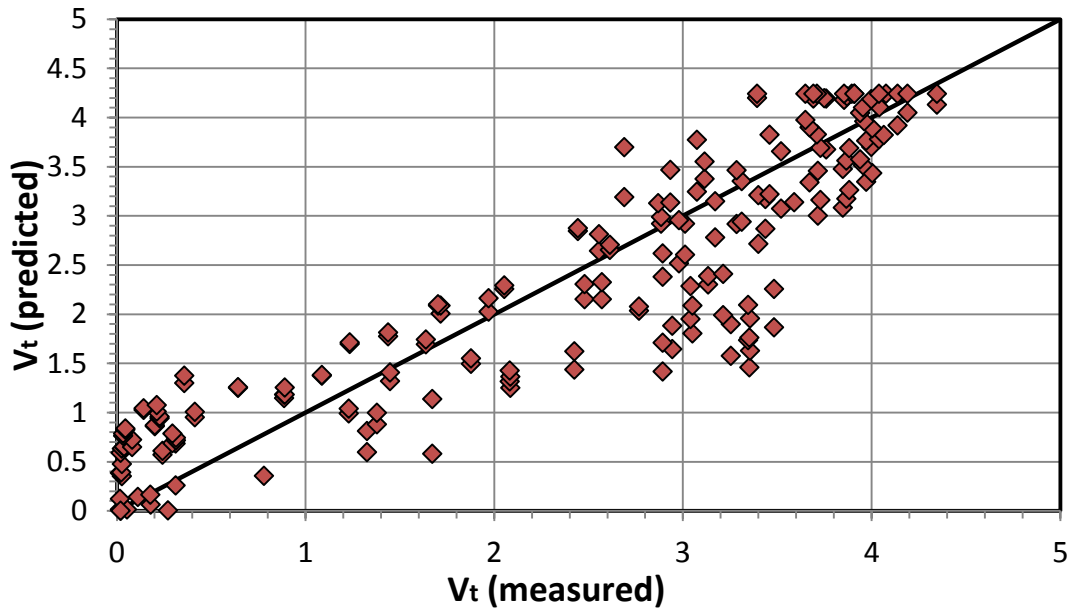


Figure 4.11 Comparisons of fall velocities measured during the present study and the predictions of the Wilson et al. (2003) method

In Chapter 2, Wilson et al.'s method for predicting terminal settling velocity of spheres in viscoplastic fluids was explained in detail. The most important advantage of this method is that no iterative calculations are required for predicting terminal settling velocity. The other major advantage is that there is no need for a different family of curves for non-Newtonian fluids and the standard Newtonian curve can be used for predictions.

The first disadvantage of Wilson et al.'s method appears in Step two of the calculations. If the reference stress of $0.3\bar{\tau}$ happens to be less than τ_y , the reference

shear rate cannot be obtained and the calculations cannot continue. While the authors argued that for these fluid-particle systems probably no settling occurs because of the large yield stress, in the present study, ten different fluid-particle systems were observed to have this condition, where the settling in fact occurred and the velocity was successfully measured, but no prediction could be made.

The second disadvantage of Wilson et al.'s method is that for $Re^* < 30$, the correlation seems to be incapable of collapsing the experimental results from settling tests in viscoplastic fluids on the Newtonian curve; in other words, the prediction method is not accurate.

In order to understand the scale of these limitations, experimental results from several sources in literature were extracted. Valentik and Whitmore (1965) published the results of settling experiments with Kaolinite-water suspensions and metal spheres. The authors reported 120 data points in total. The Wilson et al. (2003) method can only predict V_t for 68 fluid-particle systems from that study, which means 43% of the settling experiments cannot be predicted by this method.

4.4 Pipe flow analogy for non-Newtonian fluids

Wilson and Thomas (1985) introduced an analysis for the turbulent flow of non-Newtonian fluids which could explain and predict the flow properties of Bingham and power law fluids at high velocities. In this analysis, the rheological behavior of the fluid is directly obtained from the fluid rheogram without employing correlations from pipe flow data. In order to use the rheogram, a geometrical parameter was

introduced which was independent of fluid rheology model and yet could represent fluid rheology in a specific situation. The rheogram shape factor or α was defined as the ratio of the area below the rheogram (from zero to a reference point), to the area under the line for an equivalent Newtonian fluid at that reference point. Figure 4.12 shows the schematic definition of this parameter. An α of value 1 represents a Newtonian fluid while $\alpha = 2$ represents a pure plastic solid.

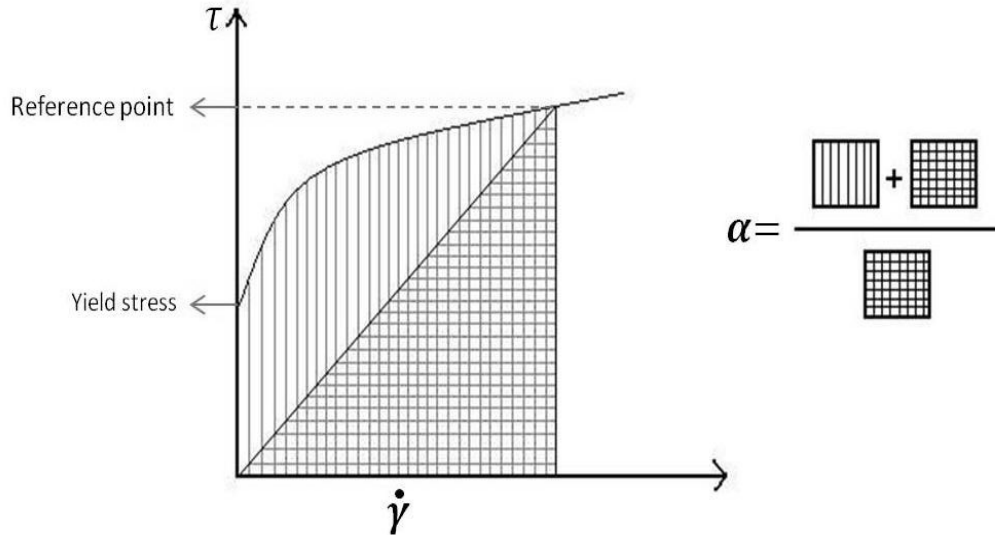


Figure 4.12 The rheogram shape factor (α)

Introducing α as the representative of fluid rheology in specific applications allowed the researchers to model complicated processes without limiting the fluid properties to any specific two-parameter or three-parameter rheology models.

In pipe flow (laminar or turbulent) the shear stress varies linearly from zero at the axis to a maximum value at the pipe wall. The Wilson-Thomas model introduces the flow properties as a function of α for non-Newtonian fluids without yield stress:

$$\frac{\bar{U}}{U^*} = f(\mu_{eq}, \alpha) \quad (4.1)$$

where \bar{U} is the time-averaged velocity of the fluid and μ_{eq} is the equivalent Newtonian viscosity of the non-Newtonian fluid at the wall. For yield stress fluids on the other hand, in addition to α , another parameter is introduced to represent deviation from Newtonian behavior:

$$\frac{\bar{U}}{U^*} = f(\mu_{eq}, \alpha, \xi) \quad (4.2)$$

$$\xi = \frac{\tau_y}{\tau_w} \quad (4.3)$$

where \bar{U} is fluid velocity, τ_y is the fluid yield stress and τ_w is the wall shear stress.

In the problem of a settling sphere in a viscoplastic fluid, α is a unique parameter that is calculated based on a combination of fluid and particle properties. In order to calculate α , a proper reference point with regard to the fluid application should be selected. Following the pipe flow analogy, Wilson et al. (2003) chose the mean surficial stress on falling sphere, or $\bar{\tau}$ (Equation 2.12), as the initial reference point for calculating α in problem of settling sphere.

4.5 Analysis of rheogram shape factor

To determine α in a settling problem, $\bar{\tau}$ is first calculated as the reference point. The rheology model of the fluid is then integrated from zero to $\bar{\tau}$ to calculate the area under the rheogram. The result of this integral is then divided by the area of the triangle produced by linking zero to the reference point. Final formulas for calculating α are shown in Equations (4.4) and (4.5) for Casson and Bingham models respectively:

$$\alpha_c = \frac{\tau_c + \frac{1}{2}\mu_c\bar{\gamma} + \frac{4}{3}(\tau_c\mu_c\bar{\gamma})^{0.5}}{\frac{1}{2}\bar{\tau}} \quad (4.4)$$

$$\alpha_B = 1 + \frac{\tau_B}{\bar{\tau}} \quad (4.5)$$

where $\bar{\gamma}$ is the corresponding shear rate at the reference point. Figure 4.13 shows that α_c is between 7.5% to 11.5% different from α_B for the 108 data points of the present study.

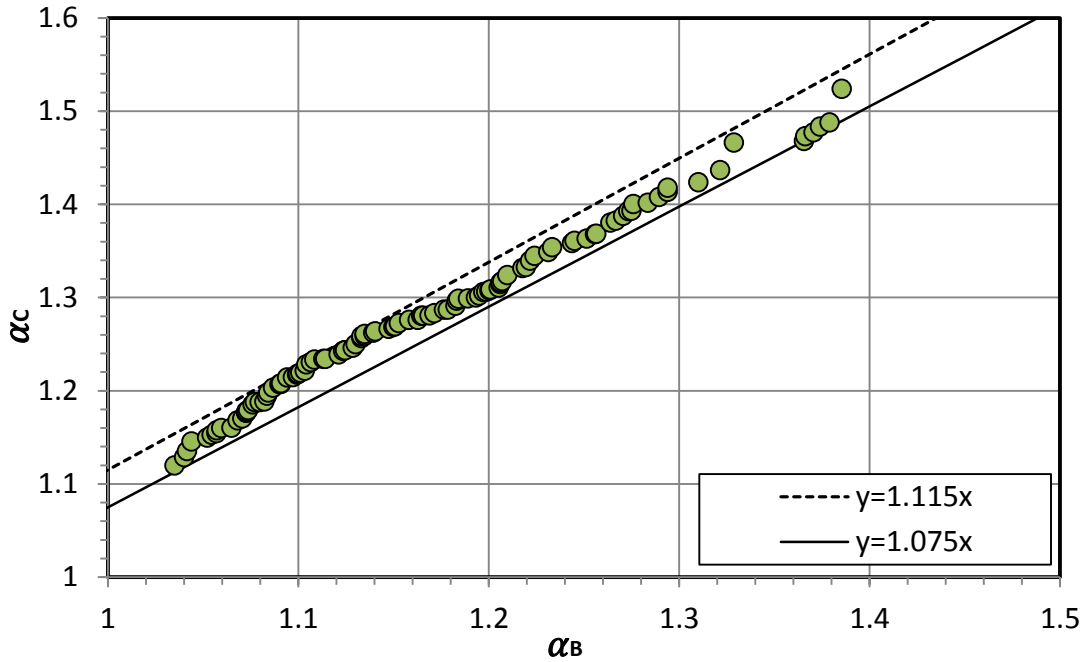


Figure 4.13 Comparison of α values calculated using the Casson and Bingham rheology models

The minor difference between calculated shape factors from the Casson and Bingham models suggests that α can be considered as a model-independent parameter which can represent the rheological behavior of the fluid in specified fluid-particle systems.

4.6 The modified prediction method

The modified method employs the Thomas-Wilson analysis for flow of non-Newtonian fluids. It was mentioned in Section 4.4 that the flow velocity of a yield stress fluid in a pipe is a function of three parameters:

$$\frac{\bar{U}}{U^*} = f(\mu_{eq}, \alpha, \xi) \quad (4.6)$$

The objective of the modified approach developed here is to apply the pipe flow analogy to particle settling and then find a function based on the same parameters to relate terminal settling velocity of a sphere in a viscoplastic fluid to the properties of the fluid-particle system. In order to do this, it is convenient to define the apparent viscosity of the viscoplastic fluid as a function of the specified parameters. The mean surficial stress ($\bar{\tau}$) is chosen as both the reference point for calculating α and as the characteristic shear stress used to calculate ξ . Experimental results published by Valentik and Whitmore (1965), Ansley and Smith (1967), Tran et al. (1993) and Wilson et al. (2003) were added to the experimental results from this study to increase the number of data points and broaden the range of applicability of the modified method.

4.7 Modification development

The proposed form of the relation between apparent viscosity and the three parameters mentioned above is:

$$\mu_{app} = \mu_{eq} \cdot f(\alpha, \xi) \quad (4.7)$$

The general methodology is to calculate μ_{app} based on different forms of f , and determine the errors of predicted fall velocities. The best function will be the one which produces the smallest errors in final predictions of V_t . The surface-fitting toolbox from MATLAB (r2010a) was applied using a trust-region fitting algorithm to fit a two-variable model (based on α and ξ) to define the apparent viscosity of the viscoplastic fluids. The root mean square error (RMSE) and coefficient of

determination (R^2) for calculated and predicted velocities are the basic criteria used to evaluate and compare different models:

$$RMSE = \left(\frac{\sum_1^n (V_{tp} - V_{tm})^2}{n} \right)^{0.5} \quad (4.8)$$

$$SS_{res} = \sum_1^n (V_{tp} - V_{tm})^2 \quad (4.9)$$

$$SS_{tot} = \sum_1^n (V_{tm} - \bar{V}_{tm})^2 \quad (4.10)$$

$$R^2 = 1 - \frac{SS_{res}}{SS_{tot}} \quad (4.11)$$

where V_{tp} is the predicted terminal settling velocity, V_{tm} is the measured terminal settling velocity, \bar{V}_{tm} is the average of measured velocities, and n is the number of data points. The RMSE represents the sample standard deviation of the differences between predicted values and observed values, and R^2 indicates how well data fit the statistical model (Morrison 2009).

To develop the model, an equivalent Newtonian fluid-particle system was assigned to each measured velocity. Each V_{tm} was inserted into Newtonian relations for the falling sphere (see Chapter 2) and a shear Reynolds number (Re_N^*) was found by back-calculation. The equivalent Newtonian viscosity calculated from this shear Reynolds number is denoted by μ_N . In order to define the apparent viscosity of the

viscoplastic fluid in a way that the settling data coincide with the standard Newtonian curve, μ_N is assumed to be the apparent viscosity of the fluid:

$$\mu_N = \mu_{eq} \cdot f(\alpha, \xi) \quad (4.12)$$

and

$$\frac{\mu_N}{\mu_{eq}} = f(\alpha, \xi) = \beta \quad (4.13)$$

The fraction $\frac{\mu_N}{\mu_{eq}}$ has been denoted as β for simplification. In order to discover the optimum form of the function f , the sensitivity of $\frac{\mu_N}{\mu_{eq}}$ to α and ξ is visualized in Figures 4.14 and 4.15. Comparison of these two graphs suggests that although no specific pattern is visible between β and ξ , the behavior of β clearly changes when α values become larger than 1.3. Based on these observations, the data points were divided into two categories based on values of α .

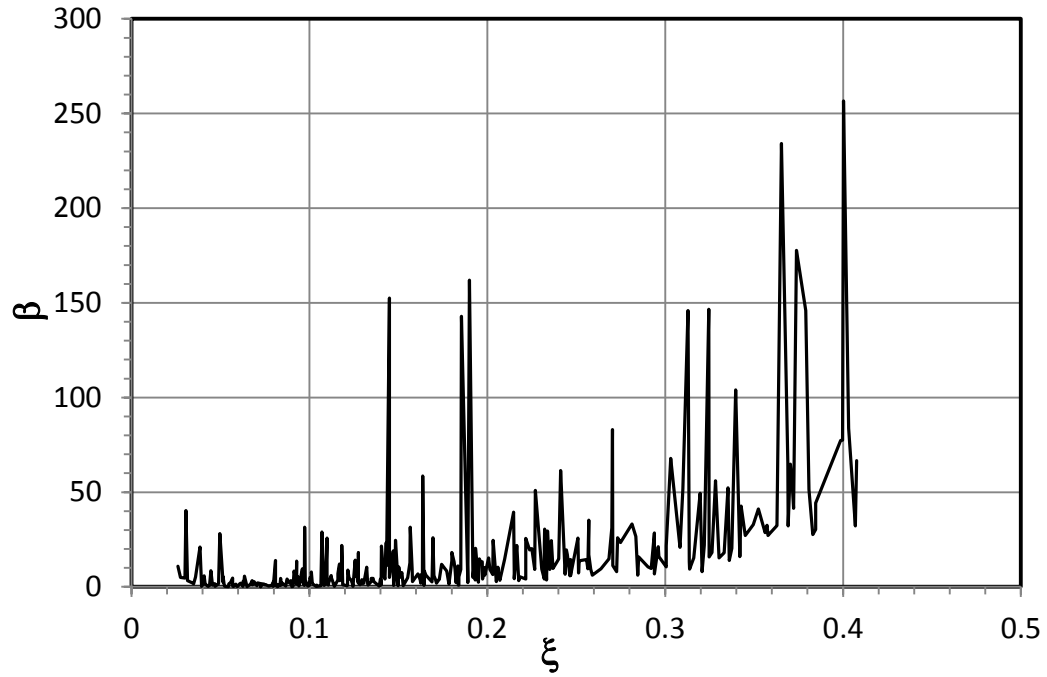


Figure 4.14 The change in modeling parameter (β) with increase of characteristic shear stress (ξ)

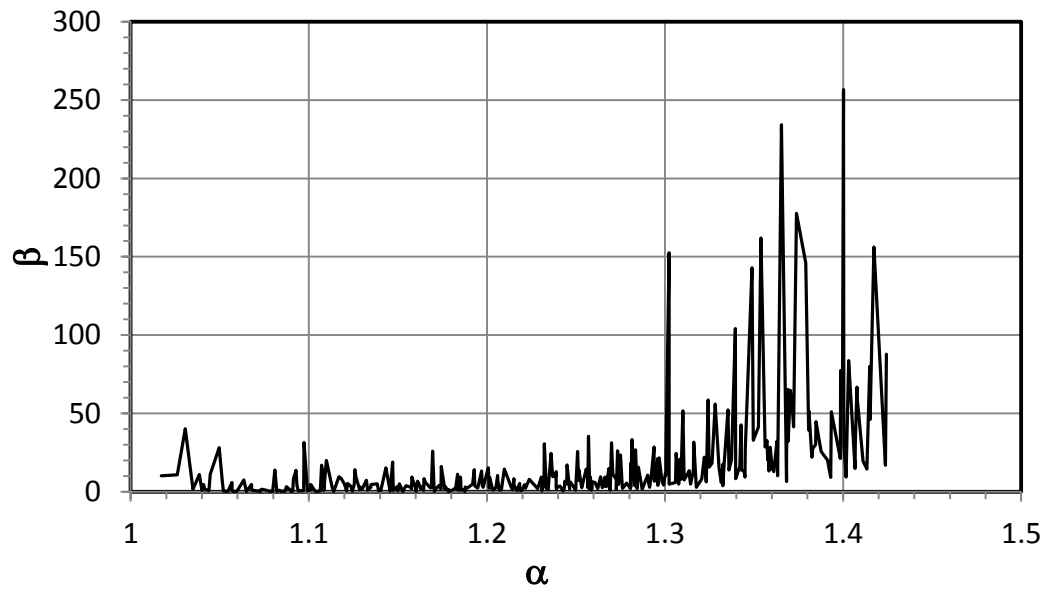


Figure 4.15 The change in modeling parameter (β) with increase of rheogram shape factor (α)

4.7.1 Category I: fall velocity prediction for systems with $\alpha < 1.3$

Surface fitting tools from MatLab (R2010a) were applied using a trust-region fitting algorithm to fit a two-variable model (based on α and ξ) to find the optimum form of the function $f(\alpha, \xi)$. A simple power form has been chosen to fit the data. Figure 4.16 visualizes the mathematical form of f . The coefficients of this equation were optimized using a genetic algorithm. The details of the optimization method and the codes are available in Appendices 4 and 5.

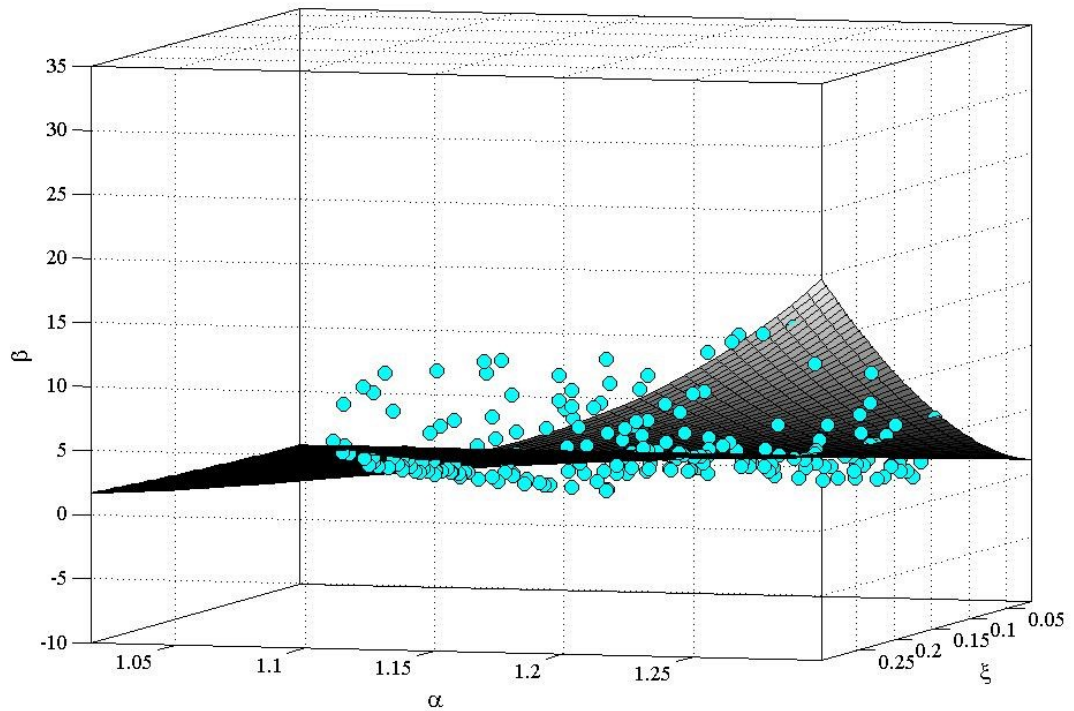


Figure 4.16 Experimental results and the fitted surface of function f , $\alpha < 1.3$

The optimization process results in Equation (4.14)

$$f(\alpha, \xi) = 4.586\alpha^{12.878}\xi^{1.612} \quad (4.14)$$

Table 4.3 compares the performance of the modified model with predictions by Wilson et al.'s correlation for 252 data points with $\alpha < 1.3$.

Table 4.3 Comparison of the performance of the modified method and Wilson et al. (2003) method for a sphere settling in a viscoplastic fluid, $\alpha < 1.3$

Prediction method	<i>RMSE</i>	<i>R</i> ²
Wilson et al.'s method	0.69	0.67
Modified method	0.47	0.85

Figure 4.17 shows the comparison between the measured velocities and predicted velocities by the modified method.

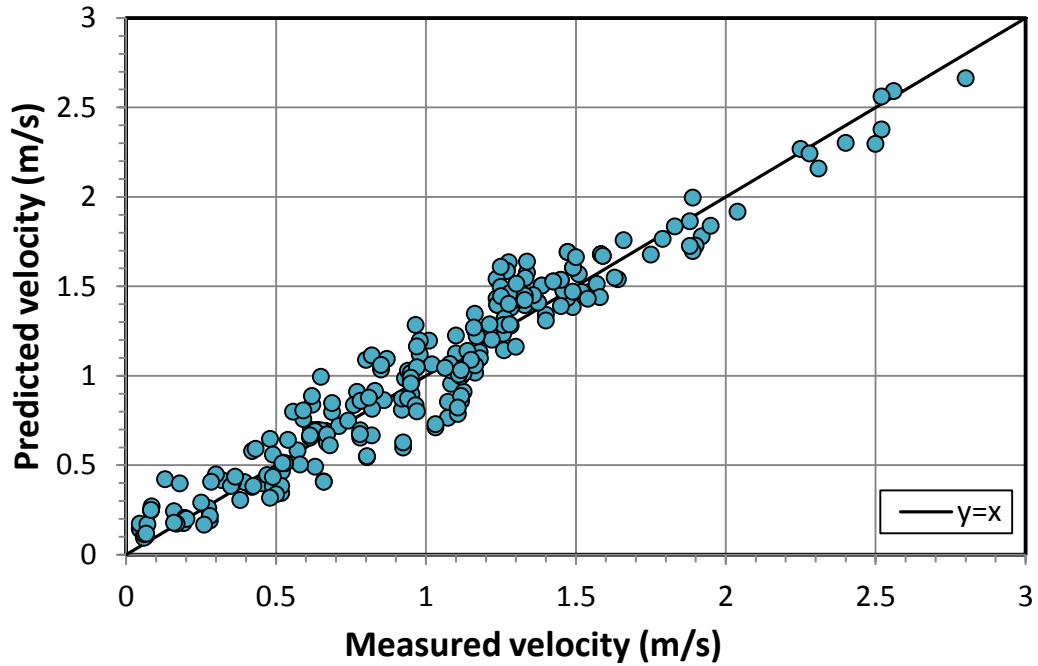


Figure 4.17 Comparison of experimental results and predicted velocities by modified method, $\alpha < 1.3$

4.7.2 Category II: fall velocity prediction for systems with $\alpha \geq 1.3$

For data points with higher values of α , a different equation was found to result in more accurate predictions. The proper form of the function was discovered by surface fitting tools and the coefficients were optimized using genetic algorithm optimization method. Figure 4.18 shows the three dimensional graph of the fitted equation.

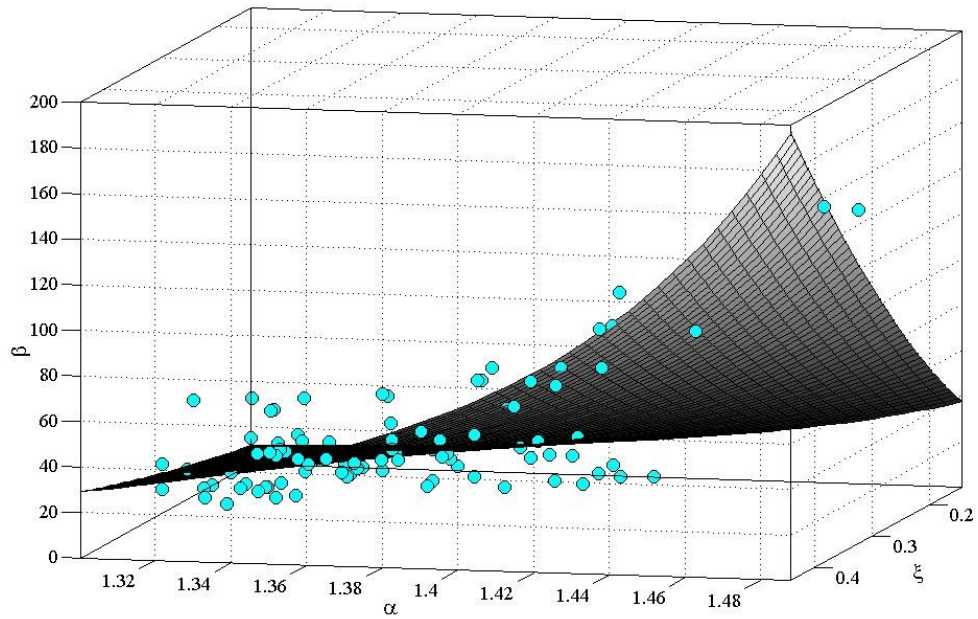


Figure 4.18 Experimental results and the fitted surface of function f , $\alpha \geq 1.3$

The optimized function was found to be:

$$f(\alpha, \xi) = 5.139\xi^{1.55} \exp(\alpha^{3.995}) + \xi^{2.747} + 0.731 \quad (4.15)$$

It is important to mention that Wilson et al.'s method was only applicable to 50 data points in this category ($\alpha \geq 1.3$) because for the remained 57 data points, $0.3\bar{\tau} < \tau_y$. Table 4.4 shows the comparison between velocity predictions by Wilson et al.'s method and the modified correlation for data points with $\alpha \geq 1.3$.

Table 4.4 Comparison of the performance of the modified method and Wilson et al.'s method for a sphere settling in a viscoplastic fluid, $\alpha \geq 1.3$

Prediction method	<i>RMSE</i>	R^2
Wilson et al.'s method	0.34	0.7
Modified method	0.33	0.92

Figure 4.19 shows the comparison between the measured velocities and predicted velocities for both methods.

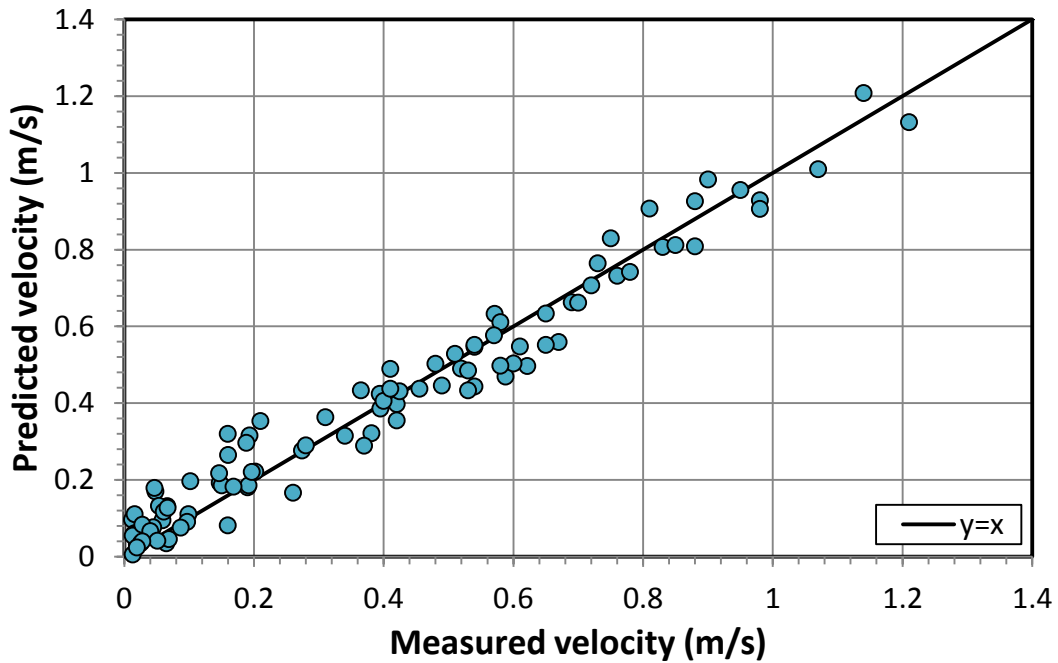


Figure 4.19 Comparison of experimental results and predicted velocities by modified method , $\alpha \geq 1.3$

Based on the results from this section and Section 4.7.1, the appropriate correlation for determining apparent viscosity of a viscoplastic fluid given the problem of predicting terminal settling velocity of a sphere is found to be:

$$\mu_{app} = \mu_{eq}(4.586\alpha^{12.878}\xi^{1.612}) \quad \text{if } \alpha < 1.3 \quad (4.16)$$

$$\mu_{app} = \mu_{eq}(5.139\xi^{1.55} \exp(\alpha^{3.995}) + \xi^{2.747} + 0.731) \quad \text{if } \alpha \geq 1.3 \quad (4.17)$$

Figure 4.20 shows the dimensionless fall velocity versus shear Reynolds number for 360 data points from this study and several sources in literature. The data points are far less scattered compared to Figure 2.15 and a fall velocity is predicted for all the fluid-particle systems.

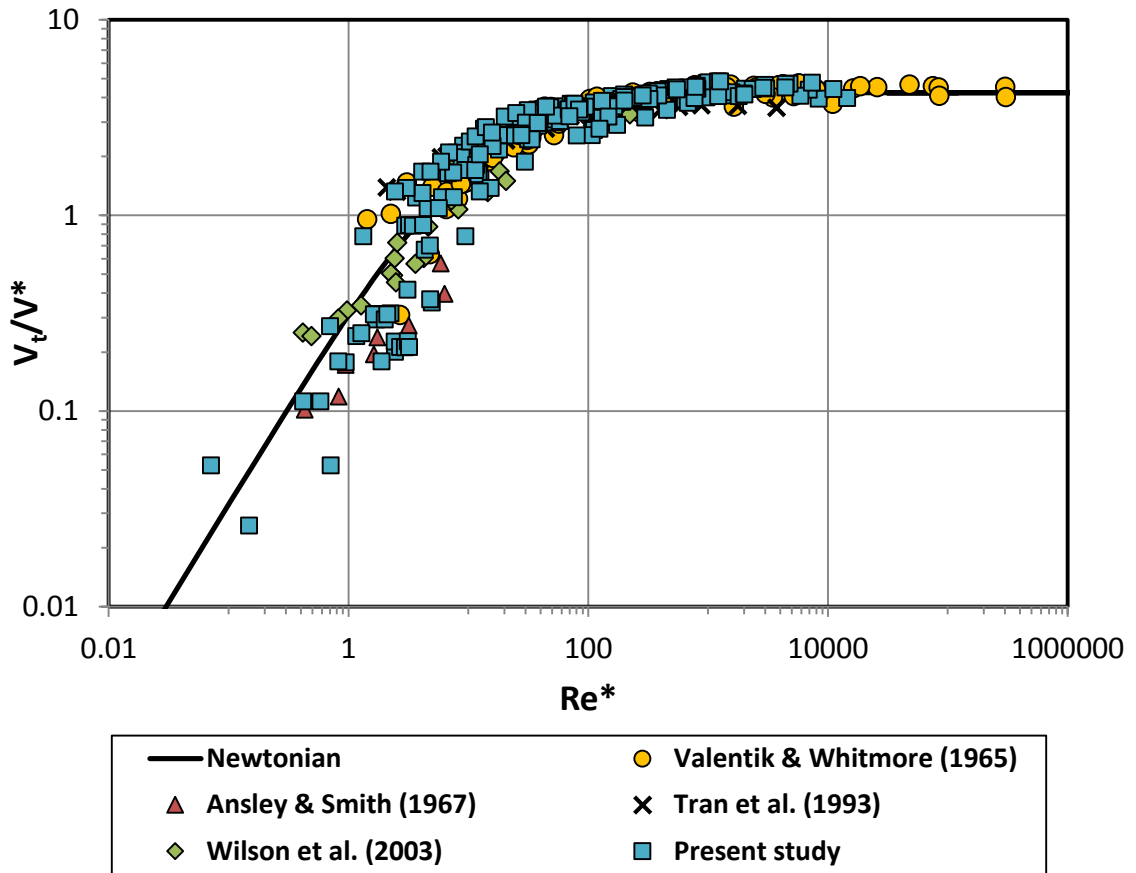


Figure 4.20 Prediction of relative velocities by the modified method for 360 data points

The statistical analysis of these prediction methods presented in Table 4.3 and 4.4 shows lower standard error (RMSE) and less scattered results (R^2 is closer to unity) for the modified method. The observations in the present study suggest that a different approach is required for prediction of settling behavior in systems with higher α . This is in qualitative agreement with the simulation results from Blackery and Mitsoulis (1997) and Prashant and Derksen (2011). These simulations suggest that in creeping motion of a sphere in a yield stress fluid, unyielded zones form close to the particle surface and expand as the yield stress increases. The high yield stress condition corresponds to a higher value of α in the pipe flow analogy. The transformation of the settling mechanism shown in existing simulations is represented in the modified prediction method by proposing different relations of apparent viscosity for high values of α .

The most important advantage of the modified method is that the new correlation is capable of predicting terminal settling velocities for fluid-particle systems where $0.3\bar{\tau} < \tau_y$. It should be noted that experiments to which this condition applied also corresponded to the fluid-particle systems with the condition $\alpha \geq 1.3$. For example, in the case of Valentik and Whitmore's study (1965), Wilson et al.'s original method is only applicable to 52% of their data. Figure 4.21 shows the data points for experiments from the present study and from the study by Valentik & Whitmore (1965) and Ansley and Smith (1967), for which Wilson et al.'s method is not capable of predicting settling velocities. For 24% of the fluid-particle systems presented here, settling occurs but the Wilson et al.'s method cannot predict the terminal settling velocity.

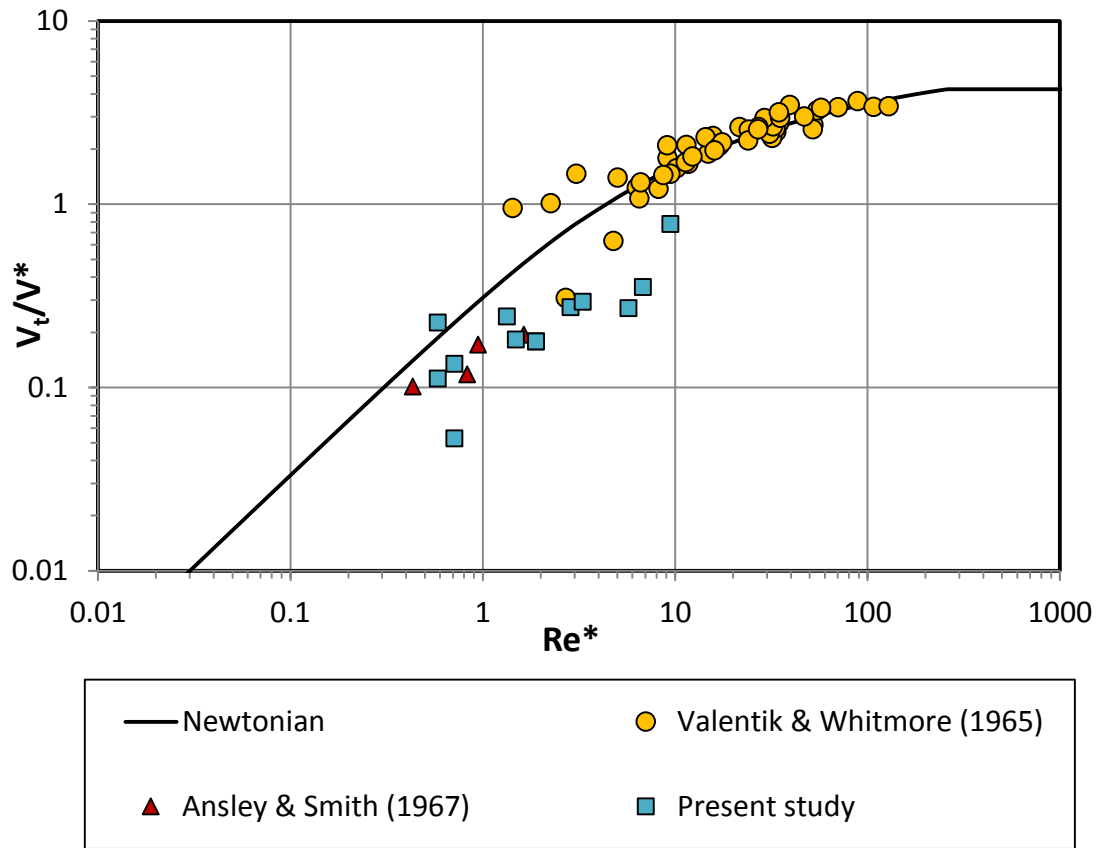


Figure 4.21 Velocity predictions by the modified method, applied to data for which the method of Wilson et al. (2003) provide no predictions

It was mentioned in Section 4.2 that the rheograms of Kaolinite-water mixtures in present study were fitted with both Casson and Bingham models. The modified correlation has been optimized to predict terminal settling velocity of a sphere in a viscoplastic fluid, regardless of the rheometry model. Figure 4.22 compares the velocity predictions of the modified method for fluid-particle systems characterized by Bingham and Casson models. It can be seen in Table 4.5 that the accuracy of predictions by the modified method is stable with the choice of either the Bingham or Casson models.

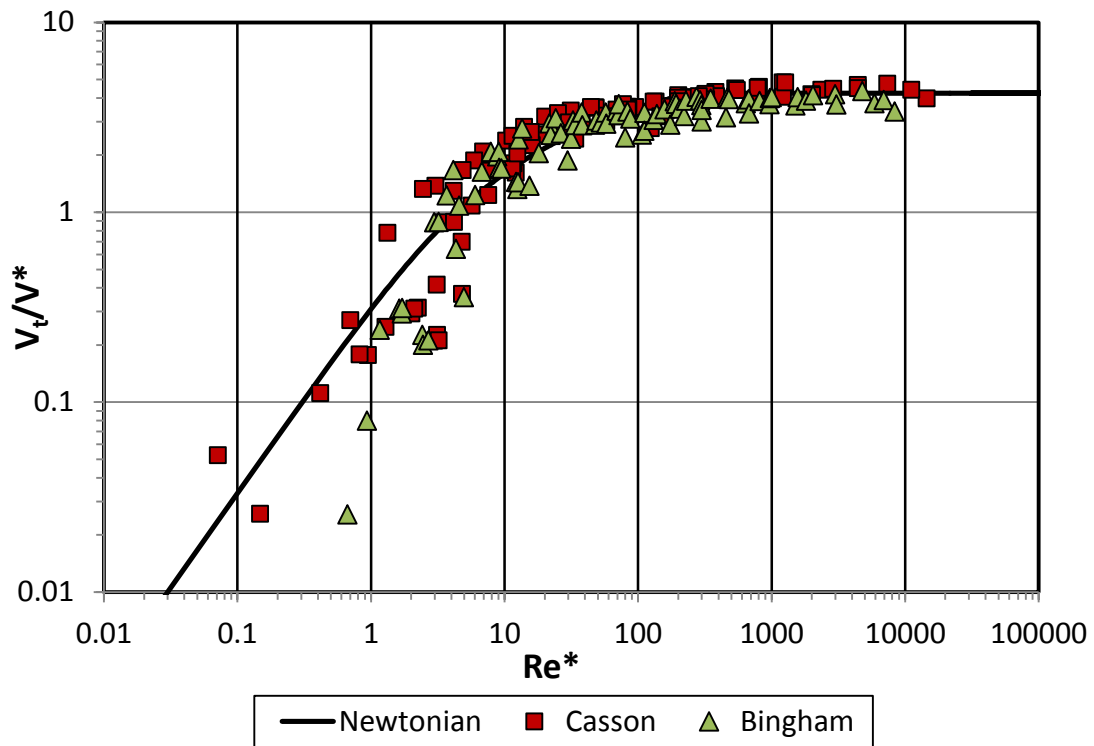


Figure 4.22 Terminal settling velocity predictions using the modified method for a sphere falling in a viscoplastic fluid

Table 4.5 The performance of the modified method for predicting the terminal settling velocities of a sphere falling in a viscoplastic fluid based on choice of Bingham or Casson fluid model

Rheometry model	<i>RMSE</i>	<i>R</i> ²
Casson	0.12	0.95
Bingham	0.16	0.88

The importance of conducting rheometry tests over a shear rate range relevant to the application of interest can be quantitatively evaluated here. For example, Figure 4.23

shows the rheometry results of a Kaolinite-water suspension ($C_v=20.1\%$, $\rho_f=1331$ kg/m³) performed for two different shear rate ranges.

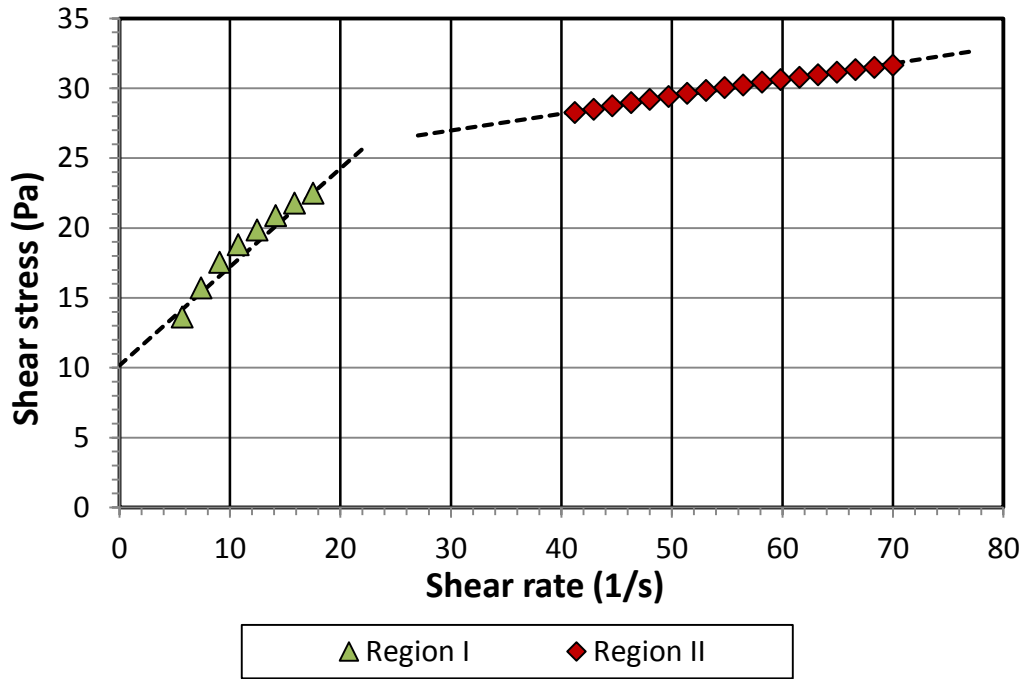


Figure 4.23 Rheogram of a Kaolinite-water suspension ($C_v=20.1\%$), obtained over two different shear rate ranges. The dotted lines represent the Bingham model fit to the two data sets

The magnitude of the Bingham yield stress and plastic viscosity of this fluid depends on which set of data (shear rate range) is selected. The fitted line to the data in Region I results in a Bingham yield stress of 10.16 Pa and the fitted line in the Region II provides a Bingham yield stress of 23.38 Pa. The fitted models are shown in Table 4.6. Now assume a steel sphere ($\rho_s=7684$ kg/m³, $d=0.01428$ m) is falling in this Kaolinite-water suspension. Regardless of the selected prediction method, the error of velocity predictions can be as low as 1.2% or as high as 54.4% depending on the selected shear rate range for characterization of the viscoplastic fluid. If one picks the

Bingham model from Region I, Wilson et al.'s method will predict the sphere to fall with a velocity of 0.44 m/s while the sphere is actually falling with a velocity twice the predicted value. The settling for this specific fluid-particle system will occur much faster in reality than what is suggested by the model. Table 4.6 shows the different predicted values of V_t by both methods, using fluid rheometry results obtained in different shear rate ranges.

Table 4.6 Velocity predictions for a steel sphere ($\rho_s=7684 \text{ kg/m}^3$, $d_p=0.01428 \text{ m}$) in a Kaolinite-water suspension ($C_v=20.1\%$, $\rho_f=1331 \text{ kg/m}^3$) fitted with two different Bingham models based on rheology measurements made over two different shear rate ranges

Prediction method	Fitted Bingham model	$V_{tp}(\text{m/s})$	Error (%)
Wilson et al. (2003)	Region I : $\tau = 10.16 + 0.71\dot{\gamma}$	0.44	54.4
	Region II: $\tau = 23.38 + 0.12\dot{\gamma}$	1.05	8.4
Modified	Region I : $\tau = 10.16 + 0.71\dot{\gamma}$	1.25	31.2
	Region II: $\tau = 23.38 + 0.12\dot{\gamma}$	0.95	1.2

Note: $V_m = 0.96 \text{ m/s}$; $\dot{\gamma}_{fall} = 45 \text{ s}^{-1}$

It is important to mention that by using α and ξ as key parameters to represent the rheology of a non-Newtonian fluid, the fluid behavior is characterized in the specific shear stress of the application as opposed to the traditional way of modeling the fluid rheology with a single two/three-parameter model for the full range of laminar flow shear rates. As was shown earlier the rheological behavior of a non-Newtonian fluid can strongly depend on the shear stress range the fluid is exposed to, and thus it is essential to characterize the fluid properties based on the parameters that represent the non-Newtonian fluid for a specific application.

5. Conclusions and recommendations for future work

5.1 Summary and conclusions

The primary objective of this research was to conduct high-quality measurements of the terminal settling velocities of single spheres falling in viscoplastic fluids, with a focus on the collection of data under conditions where existing correlations provide poor (or no) predictions. The new data, in combination with data taken from the literature, were then used to form the basis for a new, improved settling velocity correlation.

The following points summarize the key findings of the present study:

- A quantitative analysis of the Wilson et al. method (2003) for predicting terminal settling velocity of spheres in viscoplastic fluids was conducted. This method provides good predictions for cases where $Re^* > 100$. In this region, the average absolute error is 9.7% for 133 data points taken from the literature. For conditions where $Re^* < 100$, the average absolute error is 75% for 62 experimental points.
- The limitations of the Wilson et al. method (2003) were recognized and analyzed based on the available data in the literature, specifically, this method is (a) not applicable for systems with $0.3\bar{\tau} < \tau_y$, and (b) does not produce accurate predictions for systems with $Re^* < 100$.
- An experimental methodology was developed for measuring terminal settling velocity of spheres in Kaolinite-water suspensions using Electrical Impedance Tomography (EIT).

- More than 30 Kaolinite-water mixtures with concentrations ranging from 10.6% to 21.7% by volume were prepared and used as the viscoplastic medium for settling tests. Precision spheres with different sizes and densities were used for settling tests.
- Rheometry tests were carefully conducted over the shear rate ranges experienced by the fluid surrounding the particle. Both Casson and Bingham models were used to model the rheogram of the fluid.
- The analogy of Wilson-Thomas model for the turbulent pipe flow of non-Newtonian fluids was followed to study the fall velocity of spheres in viscoplastic fluids. The rheogram shape factor (α) and relative shear stress (ξ) were recognized as key parameters for yield stress fluids. The apparent viscosity of the viscoplastic fluid was defined based on these two parameters.
- The modified correlation covers the systems with $0.3\bar{\tau} < \tau_y$ and produces more accurate predictions for low Re^* regions. The accuracy of predictions obtained with the modified method is higher than previous prediction methods and the standard error is stable regardless of whether the Bingham or Casson model is used for characterization of the viscoplastic fluid.
- The analysis presented here also emphasizes the importance of making rheology measurements at relevant shear rates in order to accurately predict terminal settling velocities for particles in viscoplastic fluids.

5.2 Recommendations for future work

- The method proposed in this research has been developed based on calculations of α using Casson and Bingham models. Experimental results using Herschel-Bulkley fluids should be obtained and an analysis of the sensitivity of the modified method to the rheogram shape factor should be completed
- Spheres with rough surfaces should be tested with the same methodology to analyze the effects of surface roughness on the fall velocity of particles.
- Spherical particles are idealized form of the real irregular shaped particles present in industrial applications. Although prediction methods like this can produce an estimation of fall velocity for particles in real situations, more experimental work should be done to study the settling characteristics of non-spherical particles in non-Newtonian fluids.
- Since the size and shape of the sheared zone around a non-spherical particle falling in a viscoplastic medium are more complicated because of several factors such as to non-symmetric drag force, particle rotation and orientation, it is essential to conduct settling experiments in different conditions where three dimensional information describing the position of the particle at any moment during the fall is collected.

References

- Andres, U. Ts. "*Equilibrium and motion of spheres in a viscoplastic liquid.*" Soviet Physics Doklady. (U.S.A), 5 ,p723 (1961).
- Ansley, R.W., Smith, T.N., "*Motion of Spherical Particles in a Bingham Plastic*", AIChE. Journal, 13, p1193 (1967).
- AR-G2/AR2000ex/AR 1500ex Manual.* January (2011).
- Atapattu, D. D. *Ph.D. dissertation.* Melbourne: Monash University, (1989).
- Atapattu, D.D., Chhabra, R. P., Uhlherr, P.H.T. "*Creeping sphere motion in Herschel-Bulkley fluids: flow field and drag.*" Journal of non-Newtonian Fluid Mechanics, 59, p245 (1995).
- Atapattu, D.D., Chhabra, R.P., Tiu, C., Uhlherr, P.H.T. "*The effect of cylindrical boundaries for spheres falling in fluids having a yield stress.*" Australasian Fluid Mech. Conf., Auckland,p584 (1986).
- Atapattu, D.D., Chhabra, R.P., Uhlherr, P. H. T. "Wall effect for spheres falling at small Reynolds number in a viscoplastic medium." Journal of non-Newtonian Fluid Mechanics 38, p31 (1990).
- Barnes, H. A., Walters, K. "*The yield stress myth?*" Rheological Acta 24, p323 (1985).
- Beaulne, M., Mitsoulis, E. "*Creeping motion of a sphere in tubes filled with Herschel-Bulkley fluids*", Journal of non-Newtonian fluid Mechanics, 72, p55 (1997).
- Beris, A. N., Tsamopoulos, J., Armstrong, R. C., Brown, R. A. "*Creeping motion of a sphere through a Bingham plastic*" Journal of Fluid Mechanics 158, p219 (1985).
- Bird, R.B., Stewart, W.E., Lightfoot, E.N. *Transport Phenomena.* New York: J. Willey, (2007).
- Blackery, J., Mitsoulis, E. "*Creeping motion of a sphere in tubes filled with a Bingham plastic material*", Journal of non-Newtonian Fluid Mechanincs, 70, p59 (1997).
- Boardman, G. Whitmore, R.L. "*The static measurement of yield stress*" Laboratory Practice 10, p782 (1961).

Brown, B.H. "*Electrical Impedance Tomography (EIT)-A review.*" J. Med. Eng. Technol. 27(3), p97 (2003).

Carreau, P.J., Degee, D., Chhabra, R.P. *Rheology of polymeric systems*. Munich: Hanser, (1997).

Chafe, N. P., de Bruyn, J. R. "*Drag and relaxation in a bentonite clay suspension.*" Journal of non-Newtonian Fluid Mechanics 131, p44 (2005).

Chhabra, R. P, Agrawal, S., Chaudhary, K. "*A note on wall effect on the terminal falling velocity of a sphere in quiescent Newtonian media in cylindrical tubes.*" Powder Technology 129, p53 (2003).

Chhabra, R.P. *Bubbles, drops, and particles in non-Newtonian fluids*. Taylor & Francis, (2007).

Clift, R., Grace, J.R., Weber, M. E. *Bubbles, drops, and particles*. New York: Academic Press (1978).

Colebrook, C. F. "*Turbulent flow in pipes, with particular reference to transition region between the smooth and rough pipe laws.*" Journal of the Institute of Civil Engineers 11, p133 (1938).

Cooke, R. "*Laminar flow settling: the potential for unexpected problems*", Proc. Hydrotransport 15. Banff, AB, Canada: BHR Group, Cranfield, UK, p121 (2002).

Di Felice, R. "*A relationship for the wall effect on the settling velocity of a sphere at any flow regime*" International Journal of Multiphase Flow, 22, p527 (1996).

du Plessis, M. P., Ansley, R. W. "*Settling parameters in solids pipelining*" J.Pipeline Div. (ASCE), 93, (1967).

Elliot, D. E., Gilddon, B. J. "*Hydraulic transport of coal at high concentrations.*" Hydrotransport 1. Cranfield, UK: BHRA, paper G2 (1970).

Gillies, R. G., Hill, K.B., McKibben, M. J., Shook, C. A. "*A method for estimating deposition velocities for pseudohomogeneous slurries.*" Proc. ASME Eng Div. Summer Meeting. Vancouver, BC, Canada, (1997).

Gillies, R. G., Shook, C. A. "*Concentration Distributions of Sand Slurries in Horizontal Pipe Flow*", Particle Science Technology, 12, p45 (1994).

Gillies, R. G., Sun, R., Sanders, R. S., Schaan, J. "*Lowered expectations: The impact of yield stress on sand transport in laminar, non-Newtonian slurry flows.*" Journal of the Southern African Institute of Mining and Metallurgy, vol 107, p351 (2007).

Gillies, R. G., Hill, K. B., McKibben, M. J., Shook, C.A. "*Solids transport by laminar Newtonian flows.*" Powder Technology 104, p269 (1999).

Graham, L., Hamilton, R., Rudman, M., Strode, P., Pullum, L. "*Coarse solid concentration profiles in laminar pipe flo.*" Hydrotransport 15. Banff, Canada: BHR Group., (2003).

Gumulya, M. *The settling of spheres in viscoplastic fluids.* PhD Thesis, Perth, Australia: Curtin University of Technology, (2009).

Haberman, W.L., Sayre, R. M. *David Taylor Model Basin.* Washington: U.S. Navy Department, (1958).

Hariharaputhiran, M., Shankar Subramanian, R., Campbell, G. A., Chhabra, R.P. "The settling of spheres in a viscoplastic medium." *Journal of non-Newtonian FLuid Mechanics*, 79, p87 (1998).

Hashemi, S. A. "*Velocity and concentration fluctuations in concentrated solid-liquid flows.*" PhD dissertation. Edmonton: University of Alberta, (2013).

Kaushal, D. R., Tomita, Y. "*Prediction of Concentration Distribution in Pipeline Flow of Highly Concentrated Slurry.*" Particle Science Technology, 31, p28(2013).

L., Pullum. *Pipeline performance.* Melbourne, Australia: Paste 2003, (2003).

Litzenberger, C. G., Sumner, R. J. "Flow behavior of Kaolin clay slurries." *Hydrotransport 16.* Cranfield, U.K.: BHR Group, p77 (2004).

Masliyah, J., Czanecki, J., Xu, Z. *Handbook on theory and practice of bitumen recovery from Athabasca oil sands, Volume 1: Theoretical basis.* Kingsley Publishing Services, (2011).

Michaels, A.S., Bolger, J.C. "The plastic flow behavior of flocculated Kaolin suspensions." *Industrial and Engineering Chemistry Fundamentals 1, no. 3*, p153 (1962).

Morrison, S. J. *Introduction to Engineering Statistics.* Chichester, West Sussex, UK: Hoboken, NJ: Wiley, (2009).

Nasser, M. S., James, A. E. "*Settling and sediment bed behavior of kaolinite in aqueous media.*" Separation and Purification Technology 51, p10 (2006).

Newton, I. *Principia. Section I, II, III.* Cambridge, London: Macmillan and Co., (1863).

- Nguyen, Q. D., Boger, D. V. "*Application of Rheology to Pipeline Transport, Dewatering and Disposal of Mineral Tailings.*" 9th International Conference of Transport and Sedimentation of Solid Particles. Crascow, Poland, p 177(1997).
- Prandtl, L. "Neuere Ergebnisse Turbulenzforschung." *Z. Ver. Deutsch. Ing* 77, 5, p105(1933).
- Prashant, Derksen, J. J. "*Direct simulations of spherical particle motion in Bingham liquids.*" Computers and Chemical Engineering, p1200 (2011).
- Pullum, L., Graham, L. J. W., Slatter, P. "*A non-Newtonian two-layer model and its application to high density hydrotransport.*" Hydrotransport 16th. Santiago, Chile.: BHR Group., p579 (2004).
- De Felice. R., "*A relationship for the wall effect on the settling velocity of a sphere at any flow regime.*" International Journal of Multiphase Flow 22, p527 (1996).
- Rahman, M. H. *Yield stress of mixtures with bimodal size distributions.* MSc Thesis, Edmonton: University of Alberta, (2011).
- Rhodes, Martin. *Introduction to particle technology.* West Sussex: John Wiley and Sons. Ltd, (2008).
- Saha, G., Purohit, N.K, Mitra, A.K. "*Spherical particle terminal settling velocity and drag in Bingham liquids.*" International Journal of Mineral Processing, 36, p273 (1992).
- Schaan, J., Sanders, R. S., Gillies, R. G., McKibben, M. J., Litzenberger, C., Sun, R. J., Shook, C. A. "*Effects of shear history on flow properties of flocculant-dosed thickened tailings slurries.*" Hydrotransport 16. Cranfield, U.K.: BHR Group., p403(2004).
- Shook, C.A., Gillies, R. G., Sanders, R. S. *Pipeline Hydrotransport with Applications in the Oil Sands Industry.* Saskatoon: Saskatchewan Research Council, (2002).
- Stokes, G. G. "*On the effect of internal friction of fluids on the motion of pendulums.*" Transactions of the Cambridge Philosophical Society 9, p48 (1851).
- Talmon, A. M., van Kesteren, G. M., Sittoni, L., Hedbolm, E.P.,. "*Shear cell tests for quantification of tailings segregation*", Canadian Journal of Chemical Engineering, p362 (2014).
- Thomas, A. D., Pullum, L., Wilson, K.C. "*Stabilized laminar slurry flow: review, trends and prognosis.*" Hydrotransport 16. Cranefield, UK: BHR Group, p701 (2004).

Thomas, A.D. "*Coarse Particles in a Heavy Medium- Turbulent Pressure Drop Reduction and Deposition under Laminar Flow.*" Proc. 5th International Conference of the Hydraulic Transport of Solids in Pipes. Hanover, Germany, **(1978)**.

Tran, Q.K., Trinh, D.T., Horsley, R.R., Reizes, J.A. "*Drag coefficients and settling velocities of spheres in yield-pseudoplastic slurries.*" ASME Winter Annual Meeting. New Orleans, LA, **(1993)**.

Uhlherr, P.H.T. "*A novel method for measuring yield stress in static fluids.*" IVth National Conference of Rheology. Adelaide, p231 **(1986)**.

Valentik, L., Whitmore, R.L. "*The terminal velocity of spheres in Bingham plastics.*" Br. J. Appl. Phys. 16, p1197 **(1965)**.

van Olphen, H. *A Introduction to Clay Colloid Chemistry*. New York: Wiley-Interscience, **(1977)**.

Volarovich, M. P., Gutkin, A. M. "*Theory of flow of a viscoplastic medium.*" Colloid Journal. USSR, 15, p153 **(1953)**.

Whyte, F. M. *Fluid Mechanics, 4th Ed.* McGraw-Hill, Boston, USA, **(1999)**.

Wilson, K. C., Addie, G. R., Sellgren, A., Clift, R. *Slurry Transport Using Centrifugal Pumps*. New York: Springer **(2005)**.

Wilson, K.C, Horsely, R.R., Kealy, T., Reizes, J. C., Horsley, M. "*Direct prediction of fall velocities in non-Newtonian materials.*" International Journal of Mineral Processing 71/1-4, p17 **(2003)**.

Wilson, K.C., Horsley, R.R. "*Calculating fall velocities in non-Newtonian (and Newtonian) fluids: a new review.*" Hydrotransport 16. Cranfield, UK: BHR Group, p37**(2004)**.

Wilson, K.C., Thomas, A. D. "*A new analysis of the turbulent flow of non-Newtonian fluids.*" Canadian Journal of Chemical Engineering, p539 **(1985)**.

Yoshika, N., Adachi, K. "*On variational principles for a non-Newtonian fluid.*" J. Chem. Eng. Jpn, 4, p217 **(1971)**.

"z8000 EIT product sheet." www.itoms.com .

<http://pdf.directindustry.com/pdf/industrial-tomography-systems/z8000-electrical-impedance-tomography-product-sheet/40901-51620.html> (accessed February 25, **2015**).

Appendix 1: Calibration tests

Rheometer calibration test 1

Standard Oil	N100	Cup diameter (mm)	30.4
Test temperature	25°C	Rotor diameter (mm)	28.0
Geometry	Concentric cylinders	Rotor length (mm)	42.03
Standard viscosity at 25°C	197 mPa.s	Minimum sample (mL)	22.42
Measured viscosity	196.6 mPa.s	Operating gap (mm)	0.010
Error	0.2%		

Torque	Velocity	Temperature	Stress	Shear rate
$\mu\text{N.m}$	rad/s	°C	Pa	1/s
12.2216	0.0820504	24.997	0.198376	0.999965
60.2373	0.406163	25.001	0.977752	4.95
108.218	0.730274	25.001	1.75657	8.90001
156.118	1.05438	25.001	2.53406	12.85
203.987	1.3785	24.997	3.31105	16.8
251.834	1.70261	25.001	4.0877	20.75
299.782	2.02671	24.997	4.86597	24.7
347.645	2.35082	25.001	5.64286	28.65
395.473	2.67493	25.001	6.41919	32.6
443.19	2.99904	25.001	7.19372	36.55
490.949	3.32315	25.001	7.96892	40.5
538.733	3.64726	25.001	8.74454	44.45
586.479	3.97137	25.006	9.51953	48.4
634.238	4.29549	25.001	10.2947	52.35
681.941	4.6196	25.001	11.069	56.3
729.607	4.94371	24.997	11.8427	60.25

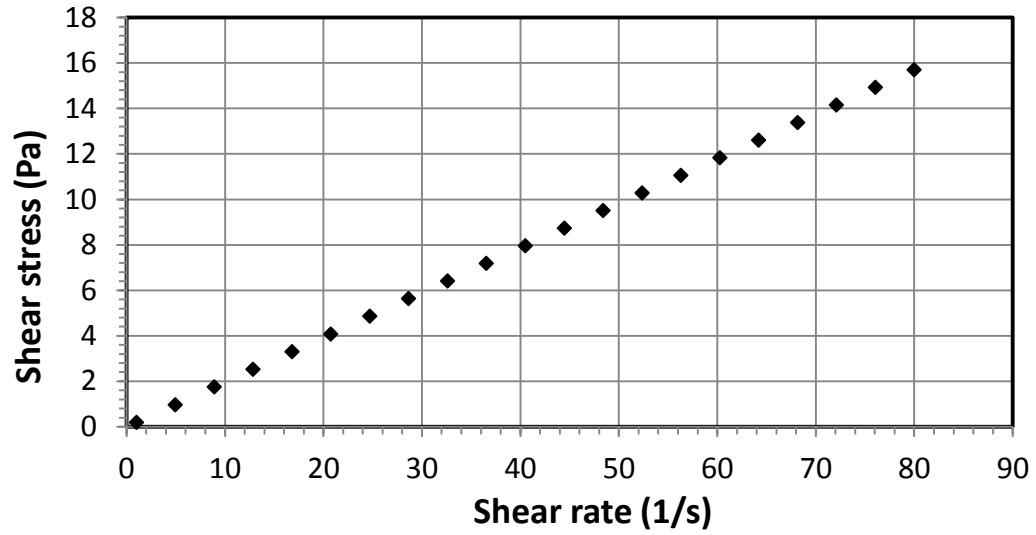
Rheometer calibration test 2

Standard Oil	S60	Cone diameter (mm)	60
Test temperature	20°C	Cone angel (°)	2.00
Geometry	Cone and Plate	Minimum sample (mL)	1.9
Standard viscosity at 20°C	140.2 mPa.s	Truncation gap (μm)	58
Measured viscosity	145.3 mPa.s		
Error	3.6%		

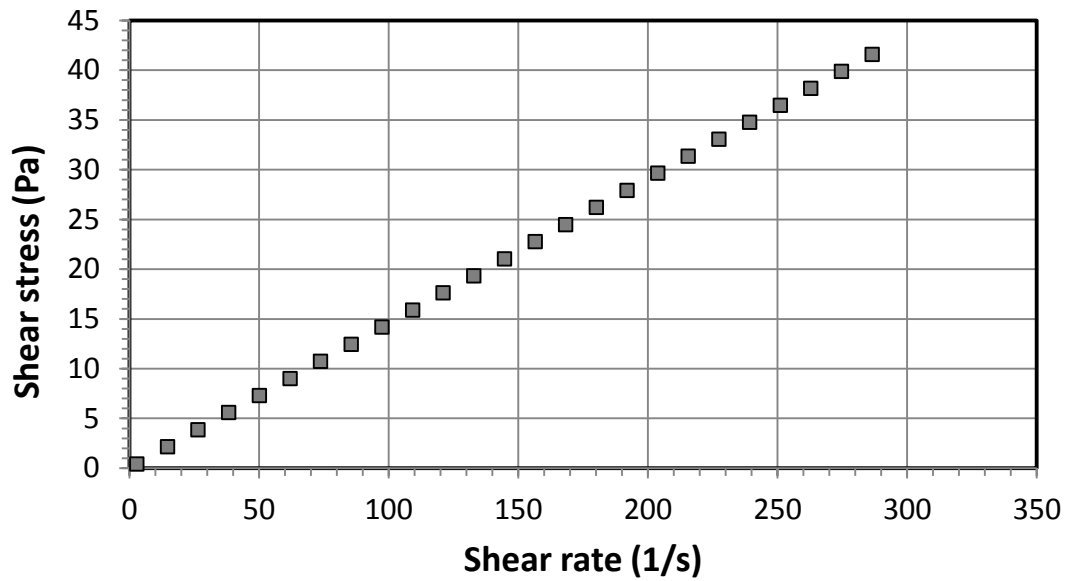
Torque	Velocity	Temperature	Stress	Shear rate
$\mu\text{N.m}$	rad/s	°C	Pa	1/s
23.5913	0.100002	19.999	0.417186	2.86484
120.891	0.5125	19.995	2.13782	14.6821
218.225	0.925	19.991	3.85907	26.4993
315.517	1.3375	20	5.57957	38.3166
412.787	1.75	20	7.29968	50.1338
509.867	2.1625	20.005	9.01643	61.951
607.171	2.575	19.994	10.7371	73.7683
704.045	2.9875	20.006	12.4502	85.5856
801.421	3.4	19.994	14.1722	97.4027
898.581	3.8125	20	15.8904	109.22
995.642	4.225	20.001	17.6068	121.037
1092.6	4.6375	20.003	19.3214	132.855
1189.96	5.05	19.998	21.0431	144.672
1287.34	5.4625	20	22.7652	156.489
1384.58	5.875	20.001	24.4848	168.306
1481.57	6.2875	19.998	26.1999	180.124
1578.4	6.7	20.002	27.9122	191.941
1675.85	7.11249	19.999	29.6355	203.758
1772.23	7.52499	20.004	31.3399	215.575
1868.96	7.9375	19.999	33.0505	227.393
1965.12	8.35	19.997	34.7509	239.21
2061.44	8.7625	20.001	36.4543	251.027

Rheograms of standard oils

N100



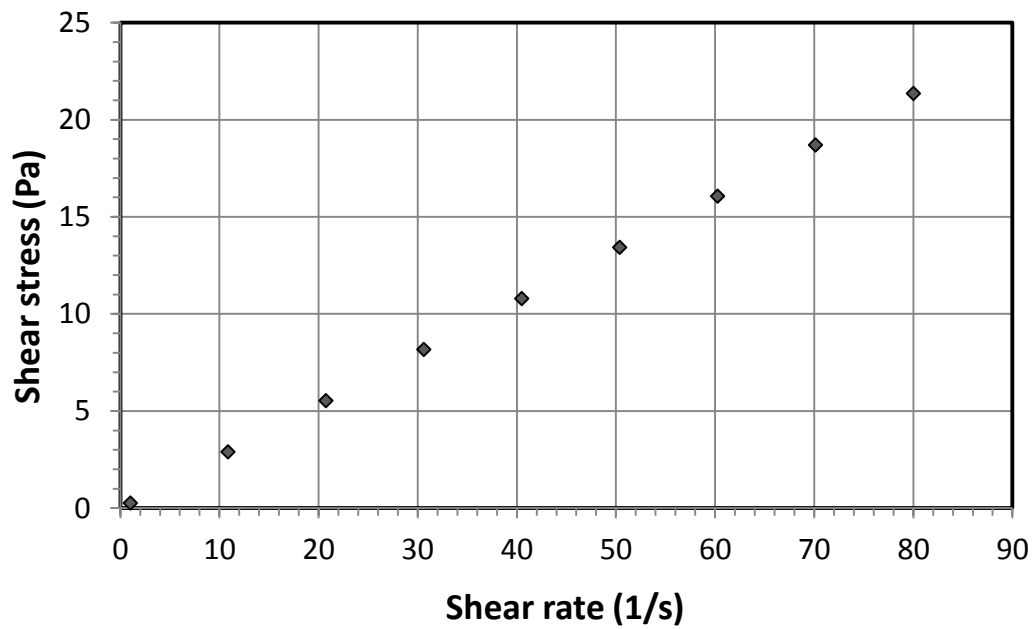
S60



Settling column Calibration:

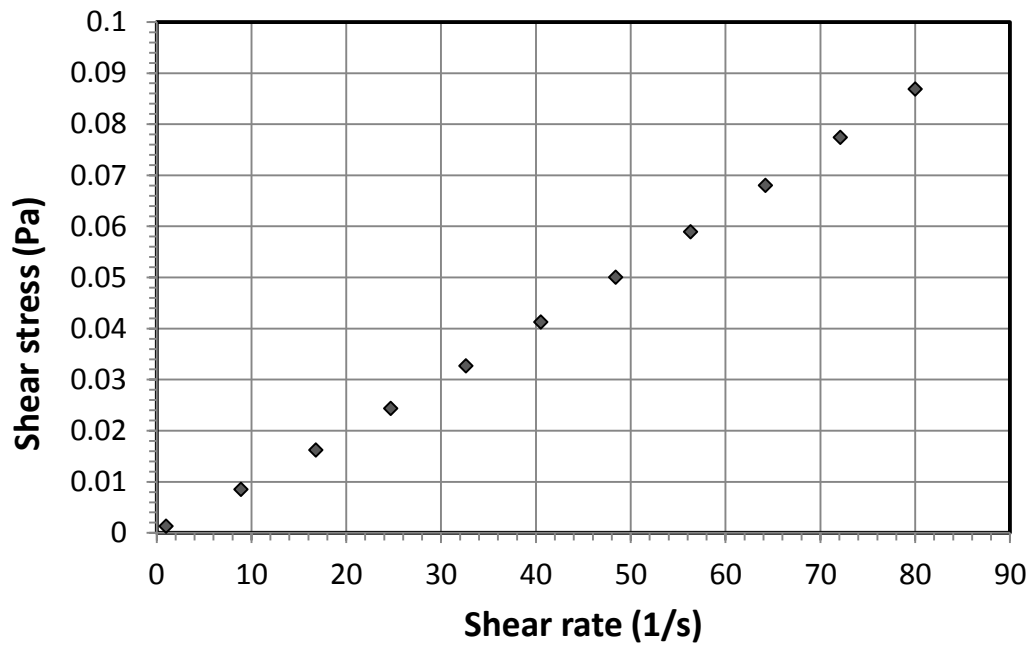
Newtonian fluid, corn syrup-water solution rheometry results

Stress	Shear rate	Temperature	Torque	Velocity
Pa	1/s	°C	μN.m	rad/s
0.271811	0.999999	22.998	16.7457	0.0820531
2.90837	10.875	22.998	179.179	0.892327
5.55112	20.75	22.994	341.993	1.7026
8.19201	30.6251	23.003	504.693	2.51289
10.8393	40.5	23.003	667.787	3.32316
13.4901	50.375	23.003	831.096	4.13343
16.1397	60.25	22.998	994.332	4.9437
18.7902	70.125	22.994	1157.62	5.75398
21.4539	80	22.998	1321.73	6.56426



Newtonian fluid, tap water rheometry results

Stress	Shear rate	Temperature	Torque	Velocity
Pa	1/s	°C	μN.m	rad/s
1.31E-03	0.999956	22	0.0805018	0.0820496
8.56E-03	8.89996	22	0.527083	0.73027
0.0162234	16.8001	22	0.999491	1.3785
0.024359	24.7	22.004	1.50071	2.02672
0.0327466	32.6	22.004	2.01745	2.67493
0.0413227	40.4999	22	2.5458	3.32315
0.0500478	48.4	22	3.08334	3.97137
0.0589659	56.3	22	3.63277	4.6196
0.0680406	64.2001	22.004	4.19184	5.26782
0.0774279	72.1	22	4.77017	5.91603
0.0868968	80	22.004	5.35353	6.56426



Appendix 2: Properties of Kaolinite-water suspensions

Sample 1:

Concentration(% by volume)	10.7
Density (kg/m ³)	1176
Bingham yield stress (Pa)	1.324
Bingham plastic viscosity (Pa.s)	0.0087
Casson yield stress (Pa)	0.6314
Casson plastic viscosity (Pa.s)	0.0044

Stress	Shear rate	Temperature	Velocity	Torque
Pa	1/s	°C	rad/s	μN.m
0.670	1.219	21.009	0.100	41.274
0.844	9.837	21.025	0.807	51.932
1.074	18.455	21.004	1.514	66.140
1.277	27.073	20.995	2.221	78.638
1.447	35.691	20.994	2.929	89.110
1.595	44.309	20.998	3.636	98.177
1.722	52.927	21.003	4.343	106.025
1.829	61.545	20.999	5.050	112.589
1.920	70.163	20.998	5.757	118.215
2.006	78.781	20.998	6.464	123.497
2.086	87.400	20.999	7.171	128.414
2.162	96.018	21.000	7.879	133.129
2.237	104.636	21.000	8.586	137.743
2.310	113.254	20.999	9.293	142.200
2.378	121.872	20.999	10.000	146.397

Sample 2:

Concentration(% by volume)	10.8
Density (kg/m ³)	1178
Bingham yield stress (Pa)	2.342
Bingham plastic viscosity (Pa.s)	0.0074
Casson yield stress (Pa)	1.635
Casson plastic viscosity (Pa.s)	0.0026

Stress	Shear rate	Temperature	Velocity	Torque
Pa	1/s	°C	rad/s	μN.m
1.692	2.865	21.094	0.100	95.662
2.255	23.123	21.100	0.807	127.506
2.588	43.381	21.101	1.514	146.353
2.839	63.639	21.100	2.221	160.521
3.041	83.897	21.099	2.929	171.954
3.214	104.155	21.101	3.636	181.746
3.369	124.414	21.101	4.343	190.526
3.512	144.672	21.099	5.050	198.588
3.645	164.930	21.100	5.757	206.125
3.768	185.188	21.099	6.464	213.103
3.887	205.446	21.100	7.171	219.808
4.006	225.704	21.100	7.879	226.542
4.123	245.963	21.101	8.586	233.170
4.232	266.221	21.099	9.293	239.320
4.335	286.479	21.100	10.000	245.142

Sample 3:

Concentration(% by volume)	11.3
Density (kg/m ³)	1186
Bingham yield stress (Pa)	2.29
Bingham plastic viscosity (Pa.s)	0.0088
Casson yield stress (Pa)	1.393
Casson plastic viscosity (Pa.s)	0.00344

Stress	Shear rate	Temperature	Velocity	Torque
Pa	1/s	°C	rad/s	μN.m
1.563	1.219	20.999	0.100	96.215
1.895	9.837	20.999	0.807	116.688
2.156	18.455	21.002	1.514	132.720
2.343	27.073	21.000	2.221	144.246
2.492	35.691	20.999	2.929	153.393
2.617	44.309	20.999	3.636	161.129
2.727	52.927	21.000	4.343	167.895
2.827	61.545	21.001	5.050	174.046
2.918	70.163	21.000	5.757	179.645
3.000	78.782	21.000	6.464	184.685
3.078	87.400	20.999	7.171	189.490
3.148	96.018	21.001	7.879	193.793
3.214	104.636	21.000	8.586	197.890
3.278	113.254	21.000	9.293	201.787
3.338	121.872	21.000	10.000	205.510

Sample 4:

Concentration(% by volume)	10.6
Density (kg/m ³)	1174
Bingham yield stress (Pa)	4.1
Bingham plastic viscosity (Pa.s)	0.0098
Casson yield stress (Pa)	2.96
Casson plastic viscosity (Pa.s)	0.0028

Stress	Shear rate	Temperature	Velocity	Torque
Pa	1/s	°C	rad/s	μN.m
1.941	2.865	20.798	0.100	109.734
2.849	23.123	20.795	0.807	161.128
3.652	43.381	20.797	1.514	206.522
4.426	63.639	20.798	2.221	250.256
4.875	83.897	20.802	2.929	275.664
5.174	104.155	20.797	3.636	292.566
5.418	124.413	20.805	4.343	306.407
5.630	144.672	20.798	5.050	318.377
5.827	164.930	20.800	5.757	329.534
6.006	185.188	20.799	6.464	339.639
6.169	205.446	20.800	7.171	348.858
6.324	225.704	20.803	7.879	357.591
6.478	245.963	20.797	8.586	366.323
6.627	266.221	20.800	9.293	374.751
6.750	286.479	20.800	10.000	381.728

Sample 5:

Concentration(% by volume)	11.1
Density (kg/m ³)	1182
Bingham yield stress (Pa)	6.57
Bingham plastic viscosity (Pa.s)	0.0125
Casson yield stress (Pa)	5.01
Casson plastic viscosity (Pa.s)	0.003

Stress	Shear rate	Temperature	Velocity	Torque
Pa	1/s	°C	rad/s	μN.m
2.965	2.865	20.798	0.100	167.651
6.014	23.123	20.797	0.807	340.069
6.825	43.381	20.799	1.514	385.932
7.328	63.639	20.804	2.221	414.408
7.679	83.897	20.795	2.929	434.247
7.971	104.156	20.796	3.636	450.733
8.235	124.414	20.798	4.343	465.678
8.485	144.672	20.799	5.050	479.834
8.726	164.930	20.801	5.757	493.463
8.958	185.188	20.802	6.464	506.563
9.188	205.447	20.798	7.171	519.591
9.414	225.704	20.799	7.879	532.327
9.620	245.962	20.800	8.586	543.980
9.828	266.221	20.800	9.293	555.759
10.036	286.479	20.799	10.000	567.521

Sample 6:

Concentration(% by volume)	15.8
Density (kg/m ³)	1260
Bingham yield stress (Pa)	11.41
Bingham plastic viscosity (Pa.s)	0.0321
Casson yield stress (Pa)	9.42
Casson plastic viscosity (Pa.s)	0.0059

Stress	Shear rate	Temperature	Velocity	Torque
Pa	1/s	°C	rad/s	μN.m
5.444	2.865	21.001	0.100	307.865
10.299	12.892	21.001	0.450	582.407
11.562	22.918	21.000	0.800	653.828
12.311	32.945	20.999	1.150	696.174
12.863	42.972	21.000	1.500	727.366
13.307	52.999	20.999	1.850	752.470
13.680	63.025	21.002	2.200	773.588
14.006	73.052	21.000	2.550	792.040
14.300	83.079	20.998	2.900	808.633
14.565	93.106	21.001	3.250	823.618
14.812	103.132	21.001	3.600	837.594
15.047	113.159	21.000	3.950	850.872
15.272	123.186	21.000	4.300	863.584
15.495	133.213	21.000	4.650	876.238
15.714	143.239	21.001	5.000	888.594

Sample 7:

Concentration(% by volume)	12.4
Density (kg/m ³)	1203
Bingham yield stress (Pa)	6.05
Bingham plastic viscosity (Pa.s)	0.02
Casson yield stress (Pa)	4.76
Casson plastic viscosity (Pa.s)	0.0045

Stress	Shear rate	Temperature	Velocity	Torque
Pa	1/s	°C	rad/s	μN.m
4.143	2.865	22.009	0.100	234.272
5.679	12.892	21.998	0.450	321.145
6.246	22.918	22.001	0.800	353.207
6.639	32.945	22.000	1.150	375.438
6.952	42.972	22.000	1.500	393.110
7.216	52.999	22.001	1.850	408.039
7.447	63.025	22.000	2.200	421.124
7.655	73.052	22.000	2.550	432.871
7.845	83.079	21.999	2.900	443.614
8.023	93.106	22.000	3.250	453.715
8.191	103.132	22.000	3.600	463.202
8.353	113.159	22.000	3.950	472.325
8.508	123.186	22.000	4.300	481.120
8.661	133.213	22.000	4.650	489.746
8.810	143.240	22.001	5.000	498.212

Sample 8:

Concentration(% by volume)	12.6
Density (kg/m ³)	1207
Bingham yield stress (Pa)	5.9
Bingham plastic viscosity (Pa.s)	0.026
Casson yield stress (Pa)	4.67
Casson plastic viscosity (Pa.s)	0.0057

Stress	Shear rate	Temperature	Velocity	Torque
Pa	1/s	°C	rad/s	μN.m
3.452	2.865	20.000	0.100	195.208
5.362	8.799	19.999	0.307	303.186
5.953	14.733	20.000	0.514	336.621
6.397	20.667	20.000	0.721	361.734
6.777	26.602	19.999	0.929	383.254
7.029	32.536	20.001	1.136	397.489
7.224	38.470	19.999	1.343	408.523
7.391	44.404	20.000	1.550	417.930
7.533	50.339	19.999	1.757	426.004
7.660	56.273	20.000	1.964	433.154
7.780	62.207	19.999	2.171	439.927
7.895	68.141	20.001	2.379	446.474
8.007	74.075	20.000	2.586	452.779
8.114	80.010	20.001	2.793	458.837
8.218	85.944	20.000	3.000	464.740

Sample 9:

Concentration(% by volume)	17.5
Density (kg/m ³)	1287
Bingham yield stress (Pa)	14.5
Bingham plastic viscosity (Pa.s)	0.054
Casson yield stress (Pa)	12.59
Casson plastic viscosity (Pa.s)	0.0087

Stress	Shear rate	Temperature	Velocity	Torque
Pa	1/s	°C	rad/s	μN.m
4.87702	2.8648	20.999	0.1	275.789
9.86913	8.7991	21	0.307147	558.086
12.4095	14.7332	21.001	0.514284	701.743
13.8371	20.6674	20.999	0.721429	782.467
14.9455	26.6016	21.001	0.928569	845.15
15.9223	32.5358	21	1.13571	900.387
16.5422	38.47	20.999	1.34286	935.439
16.9948	44.4042	21	1.55	961.034
17.3693	50.3384	21	1.75714	982.211
17.7005	56.2726	21	1.96429	1000.94
17.9974	62.2068	21	2.17143	1017.73
18.2685	68.141	21	2.37857	1033.06
18.5163	74.0752	21	2.58571	1047.07
18.7465	80.0094	21	2.79286	1060.09
18.9633	85.9437	20.999	3	1072.35

Sample 10:

Concentration(% by volume)	16.9
Density (kg/m ³)	1278
Bingham yield stress (Pa)	13.6
Bingham plastic viscosity (Pa.s)	0.055
Casson yield stress (Pa)	10.81
Casson plastic viscosity (Pa.s)	0.0122

Stress	Shear rate	Temperature	Velocity	Torque
Pa	1/s	°C	rad/s	μN.m
7.52134	2.86481	20.999	0.100001	425.322
11.3029	8.79907	21	0.307145	639.166
13.1215	14.7332	21	0.514287	742.005
14.2395	20.6673	21	0.721426	805.226
14.9117	26.6016	21	0.928571	843.237
15.4409	32.5358	20.999	1.13572	873.164
15.888	38.47	21.001	1.34286	898.446
16.2719	44.4042	21	1.55	920.156
16.5941	50.3384	21	1.75714	938.372
16.8721	56.2726	21	1.96429	954.096
17.1266	62.2068	21	2.17143	968.484
17.3678	68.1411	20.998	2.37857	982.126
17.5948	74.0752	21.001	2.58571	994.964
17.8078	80.0095	21.001	2.79286	1007.01
18.017	85.9436	20.999	3	1018.84

Sample 11:

Concentration(% by volume)	16.7
Density (kg/m ³)	1275
Bingham yield stress (Pa)	14.1
Bingham plastic viscosity (Pa.s)	0.06
Casson yield stress (Pa)	11.2
Casson plastic viscosity (Pa.s)	0.013

Stress	Shear rate	Temperature	Velocity	Torque
Pa	1/s	°C	rad/s	μN.m
7.730	2.865	20.089	0.100	437.135
11.599	8.799	20.099	0.307	655.889
13.407	14.733	20.101	0.514	758.132
14.656	20.667	20.099	0.721	828.787
15.595	26.602	20.100	0.929	881.853
16.178	32.536	20.099	1.136	914.845
16.651	38.470	20.100	1.343	941.617
17.048	44.404	20.100	1.550	964.059
17.388	50.338	20.100	1.757	983.290
17.692	56.273	20.100	1.964	1000.450
17.971	62.207	20.099	2.171	1016.230
18.229	68.141	20.099	2.379	1030.850
18.474	74.075	20.103	2.586	1044.670
18.708	80.010	20.099	2.793	1057.900
18.930	85.944	20.100	3.000	1070.490

Sample 12:

Concentration(% by volume)	16.89
Density (kg/m ³)	1277
Bingham yield stress (Pa)	8.62
Bingham plastic viscosity (Pa.s)	0.024
Casson yield stress (Pa)	7.59
Casson plastic viscosity (Pa.s)	0.0029

Stress	Shear rate	Temperature	Velocity	Torque
Pa	1/s	°C	rad/s	μN.m
7.284	2.865	20.982	0.100	411.909
8.360	8.799	20.999	0.307	472.731
8.773	14.733	21.001	0.514	496.120
9.056	20.667	21.000	0.721	512.080
9.272	26.602	21.001	0.929	524.294
9.463	32.536	21.000	1.136	535.101
9.626	38.470	21.000	1.343	544.356
9.766	44.404	21.001	1.550	552.235
9.896	50.338	20.999	1.757	559.617
10.019	56.273	21.001	1.964	566.568
10.140	62.207	21.000	2.171	573.377
10.249	68.141	21.001	2.379	579.570
10.351	74.075	21.000	2.586	585.347
10.448	80.010	21.001	2.793	590.817
10.545	85.944	20.998	3.000	596.311

Sample 13:

Concentration(% by volume)	12.2
Density (kg/m ³)	1200
Bingham yield stress (Pa)	5
Bingham plastic viscosity (Pa.s)	0.013
Casson yield stress (Pa)	3.94
Casson plastic viscosity (Pa.s)	0.0032

Stress	Shear rate	Temperature	Velocity	Torque
Pa	1/s	°C	rad/s	μN.m
2.791	2.865	21.001	0.100	157.809
4.837	23.123	20.999	0.807	273.534
5.442	43.381	21.000	1.514	307.716
5.858	63.639	21.000	2.221	331.235
6.199	83.897	21.000	2.929	350.565
6.498	104.156	21.000	3.636	367.480
6.767	124.414	20.999	4.343	382.671
7.016	144.672	21.001	5.050	396.744
7.247	164.930	21.000	5.757	409.823
7.467	185.188	21.000	6.464	422.226
7.680	205.446	20.999	7.171	434.290
7.884	225.704	20.999	7.879	445.834
8.078	245.963	21.000	8.586	456.820
8.271	266.221	21.000	9.293	467.690
8.459	286.479	20.999	10.000	478.359

Sample 14:

Concentration(% by volume)	14.7
Density (kg/m ³)	1241
Bingham yield stress (Pa)	7.84
Bingham plastic viscosity (Pa.s)	0.026
Casson yield stress (Pa)	6.244
Casson plastic viscosity (Pa.s)	0.0054

Stress	Shear rate	Temperature	Velocity	Torque
Pa	1/s	°C	rad/s	μN.m
4.128	2.865	21.200	0.100	233.433
5.585	6.753	21.200	0.236	315.805
6.375	10.641	21.201	0.371	360.497
6.929	14.529	21.199	0.507	391.828
7.327	18.417	21.200	0.643	414.325
7.662	22.304	21.201	0.779	433.263
8.019	26.192	21.198	0.914	453.482
8.299	30.080	21.200	1.050	469.297
8.474	33.968	21.200	1.186	479.220
8.623	37.856	21.201	1.321	487.596
8.762	41.744	21.200	1.457	495.488
8.889	45.632	21.200	1.593	502.655
9.009	49.520	21.199	1.729	509.440
9.122	53.408	21.200	1.864	515.814
9.230	57.296	21.199	2.000	521.957

Sample 15:

Concentration(% by volume)	15.4
Density (kg/m ³)	1252
Bingham yield stress (Pa)	8.9
Bingham plastic viscosity (Pa.s)	0.024
Casson yield stress (Pa)	7.47
Casson plastic viscosity (Pa.s)	0.004

Stress	Shear rate	Temperature	Velocity	Torque
Pa	1/s	°C	rad/s	μN.m
3.303	2.865	22.500	0.100	186.804
6.150	6.753	22.500	0.236	347.747
7.058	10.641	22.498	0.371	399.116
7.724	14.529	22.501	0.507	436.781
8.256	18.417	22.501	0.643	466.856
8.626	22.304	22.500	0.779	487.766
8.949	26.192	22.501	0.914	506.067
9.326	30.080	22.499	1.050	527.385
9.583	33.968	22.499	1.186	541.931
9.737	37.856	22.500	1.321	550.616
9.862	41.744	22.498	1.457	557.689
9.978	45.632	22.500	1.593	564.223
10.082	49.520	22.501	1.729	570.100
10.183	53.408	22.499	1.864	575.806
10.278	57.296	22.499	2.000	581.193

Sample 16:

Concentration(% by volume)	17.6
Density (kg/m ³)	1289
Bingham yield stress (Pa)	19.1
Bingham plastic viscosity (Pa.s)	0.063
Casson yield stress (Pa)	15.43
Casson plastic viscosity (Pa.s)	0.0123

Stress	Shear rate	Temperature	Velocity	Torque
Pa	1/s	°C	rad/s	μN.m
5.558	2.865	22.396	0.100	314.303
12.463	6.753	22.400	0.236	704.787
15.099	10.641	22.407	0.371	853.822
16.576	14.529	22.400	0.507	937.346
17.767	18.417	22.399	0.643	1004.720
18.826	22.304	22.396	0.779	1064.600
19.595	26.192	22.407	0.914	1108.080
20.362	30.080	22.409	1.050	1151.460
20.945	33.968	22.398	1.186	1184.410
21.316	37.856	22.399	1.321	1205.380
21.586	41.744	22.402	1.457	1220.630
21.852	45.632	22.397	1.593	1235.690
22.088	49.520	22.402	1.729	1249.070
22.311	53.408	22.402	1.864	1261.640
22.541	57.296	22.397	2.000	1274.680

Sample 17:

Concentration(% by volume)	20.1
Density (kg/m ³)	1331
Bingham yield stress (Pa)	27.3
Bingham plastic viscosity (Pa.s)	0.145
Casson yield stress (Pa)	19.7
Casson plastic viscosity (Pa.s)	0.04

Stress	Shear rate	Temperature	Velocity	Torque
Pa	1/s	°C	rad/s	μN.m
6.994	2.865	23.302	0.100	395.507
17.432	6.753	23.299	0.236	985.735
21.051	10.641	23.301	0.371	1190.380
23.983	14.529	23.299	0.507	1356.190
25.988	18.417	23.301	0.643	1469.560
27.615	22.304	23.299	0.779	1561.610
29.091	26.192	23.300	0.914	1645.050
30.372	30.080	23.301	1.050	1717.480
31.425	33.968	23.301	1.186	1777.040
32.472	37.856	23.299	1.321	1836.220
33.509	41.744	23.301	1.457	1894.870
34.304	45.632	23.300	1.593	1939.850
34.923	49.520	23.299	1.729	1974.830
35.473	53.408	23.302	1.864	2005.940
35.953	57.296	23.299	2.000	2033.070

Sample 18:

Concentration(% by volume)	19.4
Density (kg/m ³)	1318
Bingham yield stress (Pa)	19
Bingham plastic viscosity (Pa.s)	0.083
Casson yield stress (Pa)	16.17
Casson plastic viscosity (Pa.s)	0.011

Stress	Shear rate	Temperature	Velocity	Torque
Pa	1/s	°C	rad/s	μN.m
9.963	2.865	23.600	0.100	563.419
14.054	6.753	23.600	0.236	794.760
16.639	10.641	23.600	0.371	940.889
18.371	14.529	23.600	0.507	1038.850
19.338	18.417	23.599	0.643	1093.560
20.322	22.304	23.601	0.779	1149.180
21.065	26.192	23.599	0.914	1191.200
21.506	30.080	23.601	1.050	1216.150
21.874	33.968	23.601	1.186	1236.970
22.222	37.856	23.600	1.321	1256.600
22.543	41.744	23.599	1.457	1274.760
22.846	45.632	23.600	1.593	1291.930
23.142	49.520	23.600	1.729	1308.630
23.424	53.408	23.599	1.864	1324.570
23.699	57.296	23.600	2.000	1340.140

Sample 19:

Concentration(% by volume)	21.73
Density (kg/m ³)	1357
Bingham yield stress (Pa)	30
Bingham plastic viscosity (Pa.s)	0.98
Casson yield stress (Pa)	25.65
Casson plastic viscosity (Pa.s)	0.15

Stress	Shear rate	Temperature	Velocity	Torque
Pa	1/s	°C	rad/s	μN.m
14.144	0.358	24.201	0.100	799.824
21.357	0.844	24.199	0.236	1207.680
25.595	1.330	24.201	0.371	1447.380
27.892	1.816	24.201	0.507	1577.270
29.995	2.302	24.205	0.643	1696.180
31.231	2.788	24.198	0.779	1766.090
32.298	3.274	24.197	0.914	1826.390
33.484	3.760	24.203	1.050	1893.490
34.153	4.246	24.200	1.186	1931.300
34.714	4.732	24.200	1.321	1963.000
35.239	5.218	24.202	1.457	1992.720
35.719	5.704	24.198	1.593	2019.880
36.183	6.190	24.200	1.729	2046.070
36.619	6.676	24.202	1.864	2070.780
37.041	7.162	24.198	2.000	2094.620

Sample 20:

Concentration(% by volume)	21.73
Density (kg/m ³)	1357
Bingham yield stress (Pa)	19.5
Bingham plastic viscosity (Pa.s)	0.45
Casson yield stress (Pa)	12.8
Casson plastic viscosity (Pa.s)	0.157

Stress	Shear rate	Temperature	Velocity	Torque
Pa	1/s	°C	rad/s	μN.m
13.8182	2.86483	23.2	0.100001	781.401
15.9538	4.70649	23.201	0.164288	902.169
19.0855	6.5481	23.2	0.228572	1079.26
21.5917	8.38974	23.199	0.292857	1220.98
23.2561	10.2314	23.201	0.357144	1315.1
24.6405	12.073	23.201	0.421429	1393.39
25.9118	13.9147	23.199	0.485714	1465.28
27.1444	15.7563	23.2	0.55	1534.98
27.9679	17.598	23.202	0.614286	1581.55
28.6332	19.4396	23.2	0.678571	1619.17
29.3195	21.2813	23.2	0.742857	1657.98
30.2032	23.1229	23.2	0.807143	1707.95
30.9063	24.9646	23.2	0.871429	1747.71
31.3532	26.8062	23.198	0.935715	1772.98
31.7095	28.6479	23.201	1	1793.13

Sample 21:

Concentration(% by volume)	19.5
Density (kg/m ³)	1320
Bingham yield stress (Pa)	12.2
Bingham plastic viscosity (Pa.s)	0.45
Casson yield stress (Pa)	8.49
Casson plastic viscosity (Pa.s)	0.131

Stress	Shear rate	Temperature	Velocity	Torque
Pa	1/s	°C	rad/s	μN.m
12.677	4.000	23.600	0.140	716.843
13.233	4.786	23.600	0.167	748.328
13.900	5.571	23.600	0.194	786.013
14.542	6.357	23.600	0.222	822.356
15.146	7.143	23.599	0.249	856.505
15.603	7.929	23.600	0.277	882.306
15.935	8.714	23.600	0.304	901.093
16.237	9.500	23.600	0.332	918.206
16.508	10.286	23.600	0.359	933.497
16.784	11.071	23.600	0.386	949.114
17.093	11.857	23.600	0.414	966.577
17.490	12.643	23.600	0.441	989.011
17.804	13.429	23.600	0.469	1006.810
18.011	14.214	23.600	0.496	1018.490
18.175	15.000	23.600	0.524	1027.750

Sample 22:

Concentration(% by volume)	19.13
Density (kg/m ³)	1314
Bingham yield stress (Pa)	16.2
Bingham plastic viscosity (Pa.s)	0.33
Casson yield stress (Pa)	12.26
Casson plastic viscosity (Pa.s)	0.084

Stress	Shear rate	Temperature	Velocity	Torque
Pa	1/s	°C	rad/s	μN.m
8.978	4.000	24.600	0.140	507.713
11.008	5.143	24.600	0.180	622.473
13.293	6.286	24.600	0.219	751.725
14.652	7.429	24.600	0.259	828.536
15.973	8.571	24.600	0.299	903.238
17.001	9.714	24.600	0.339	961.360
17.977	10.857	24.600	0.379	1016.590
18.737	12.000	24.600	0.419	1059.560
19.454	13.143	24.601	0.459	1100.100
20.161	14.286	24.601	0.499	1140.090
20.757	15.429	24.601	0.539	1173.780
21.321	16.571	24.599	0.578	1205.670
21.962	17.714	24.600	0.618	1241.910
22.461	18.857	24.600	0.658	1270.160
22.901	20.000	24.599	0.698	1295.020
23.026	20.000	24.599	0.698	1302.110
23.480	21.429	24.600	0.748	1327.740
23.934	22.857	24.600	0.798	1353.460
24.328	24.286	24.599	0.848	1375.700
24.749	25.714	24.601	0.898	1399.530
25.209	27.143	24.600	0.947	1425.560
25.595	28.571	24.600	0.997	1447.350
25.884	30.000	24.599	1.047	1463.680

Sample 23:

Concentration(% by volume)	19.13
Density (kg/m ³)	1314
Bingham yield stress (Pa)	13.5
Bingham plastic viscosity (Pa.s)	0.46
Casson yield stress (Pa)	8.74
Casson plastic viscosity (Pa.s)	0.165

Stress	Shear rate	Temperature	Velocity	Torque
Pa	1/s	°C	rad/s	μN.m
8.978	4.000	24.600	0.140	507.713
11.008	5.143	24.600	0.180	622.473
13.293	6.286	24.600	0.219	751.725
14.652	7.429	24.600	0.259	828.536
15.973	8.571	24.600	0.299	903.238
17.001	9.714	24.600	0.339	961.360
17.977	10.857	24.600	0.379	1016.590
18.737	12.000	24.600	0.419	1059.560
19.454	13.143	24.601	0.459	1100.100
20.161	14.286	24.601	0.499	1140.090
20.757	15.429	24.601	0.539	1173.780
21.321	16.571	24.599	0.578	1205.670
21.962	17.714	24.600	0.618	1241.910
22.461	18.857	24.600	0.658	1270.160
22.901	20.000	24.599	0.698	1295.020
23.026	20.000	24.599	0.698	1302.110
23.480	21.429	24.600	0.748	1327.740
23.934	22.857	24.600	0.798	1353.460
24.328	24.286	24.599	0.848	1375.700
24.749	25.714	24.601	0.898	1399.530
25.209	27.143	24.600	0.947	1425.560
25.595	28.571	24.600	0.997	1447.350
25.884	30.000	24.599	1.047	1463.680

Sample 24:

Concentration(% by volume)	21.1
Density (kg/m ³)	1347
Bingham yield stress (Pa)	20.6
Bingham plastic viscosity (Pa.s)	0.42
Casson yield stress (Pa)	16.37
Casson plastic viscosity (Pa.s)	0.097

Stress	Shear rate	Temperature	Velocity	Torque
Pa	1/s	°C	rad/s	μN.m
24.288	10.000	24.002	0.349	1373.450
24.852	11.429	24.000	0.399	1405.320
25.759	12.857	24.001	0.449	1456.660
26.650	14.286	24.000	0.499	1507.000
27.731	15.714	24.001	0.549	1568.130
28.541	17.143	24.000	0.598	1613.980
28.998	18.571	24.000	0.648	1639.770
29.435	20.000	24.001	0.698	1664.530
29.812	21.429	23.998	0.748	1685.800
30.264	22.857	24.001	0.798	1711.400
30.759	24.286	24.000	0.848	1739.350
31.479	25.714	24.000	0.898	1780.090
32.038	27.143	23.999	0.947	1811.730
32.380	28.571	23.999	0.997	1831.060
32.683	30.000	24.001	1.047	1848.170

Sample 25:

Concentration(% by volume)	19.6
Density (kg/m ³)	1322
Bingham yield stress (Pa)	17.6
Bingham plastic viscosity (Pa.s)	0.12
Casson yield stress (Pa)	14.1
Casson plastic viscosity (Pa.s)	0.024

Stress	Shear rate	Temperature	Velocity	Torque
Pa	1/s	°C	rad/s	μN.m
16.297	10.000	24.301	0.349	921.551
16.717	11.429	24.300	0.399	945.333
17.372	12.857	24.298	0.449	982.364
17.939	14.286	24.301	0.499	1014.450
18.359	15.714	24.299	0.549	1038.200
18.716	17.143	24.299	0.598	1058.370
19.062	18.571	24.301	0.648	1077.930
19.426	20.000	24.298	0.698	1098.490
19.857	21.429	24.300	0.748	1122.900
20.345	22.857	24.299	0.798	1150.500
20.639	24.286	24.299	0.848	1167.110
20.863	25.714	24.302	0.898	1179.750
21.062	27.143	24.299	0.947	1191.000
21.247	28.571	24.300	0.997	1201.470
21.414	30.000	24.300	1.047	1210.910
21.440	30.000	24.300	1.047	1212.420
21.623	31.429	24.300	1.097	1222.730
21.795	32.857	24.298	1.147	1232.490
21.947	34.286	24.300	1.197	1241.080
22.093	35.714	24.300	1.247	1249.300
22.256	37.143	24.299	1.297	1258.530
22.416	38.571	24.301	1.346	1267.570
22.569	40.000	24.300	1.396	1276.270

Sample 26:

Concentration(% by volume)	17.1
Density (kg/m ³)	1280
Bingham yield stress (Pa)	15.1
Bingham plastic viscosity (Pa.s)	0.11
Casson yield stress (Pa)	11.8
Casson plastic viscosity (Pa.s)	0.026

Stress	Shear rate	Temperature	Velocity	Torque
Pa	1/s	°C	rad/s	μN.m
12.096	10.000	23.000	0.349	683.994
12.234	11.579	23.000	0.404	691.791
12.644	13.158	22.999	0.459	714.991
13.114	14.737	23.001	0.514	741.553
13.542	16.316	22.999	0.570	765.754
13.920	17.895	23.001	0.625	787.141
14.316	19.474	23.001	0.680	809.563
14.708	21.053	22.999	0.735	831.701
15.105	22.632	23.001	0.790	854.167
15.431	24.211	23.000	0.845	872.618
15.696	25.790	23.000	0.900	887.584
15.936	27.368	22.999	0.955	901.165
16.168	28.947	23.000	1.010	914.251
16.370	30.526	22.999	1.066	925.725
16.563	32.105	23.000	1.121	936.590
16.754	33.684	23.000	1.176	947.431
16.933	35.263	23.001	1.231	957.509
17.106	36.842	23.001	1.286	967.339
17.269	38.421	23.000	1.341	976.538
17.415	40.000	23.000	1.396	984.776

Sample 27:

Concentration(% by volume)	16.7
Density (kg/m ³)	1275
Bingham yield stress (Pa)	14.5
Bingham plastic viscosity (Pa.s)	0.1
Casson yield stress (Pa)	12.7
Casson plastic viscosity (Pa.s)	0.013

Stress	Shear rate	Temperature	Velocity	Torque
Pa	1/s	°C	rad/s	μN.m
12.096	10.000	23.000	0.349	683.994
12.234	11.579	23.000	0.404	691.791
12.644	13.158	22.999	0.459	714.991
13.114	14.737	23.001	0.514	741.553
13.542	16.316	22.999	0.570	765.754
13.920	17.895	23.001	0.625	787.141
14.316	19.474	23.001	0.680	809.563
14.708	21.053	22.999	0.735	831.701
15.105	22.632	23.001	0.790	854.167
15.431	24.211	23.000	0.845	872.618
15.696	25.790	23.000	0.900	887.584
15.936	27.368	22.999	0.955	901.165
16.168	28.947	23.000	1.010	914.251
16.370	30.526	22.999	1.066	925.725
16.563	32.105	23.000	1.121	936.590
16.754	33.684	23.000	1.176	947.431
16.933	35.263	23.001	1.231	957.509
17.106	36.842	23.001	1.286	967.339
17.269	38.421	23.000	1.341	976.538
17.415	40.000	23.000	1.396	984.776

Sample 28:

Concentration(% by volume)	18.5
Density (kg/m ³)	1303
Bingham yield stress (Pa)	16.88
Bingham plastic viscosity (Pa.s)	0.1
Casson yield stress (Pa)	14
Casson plastic viscosity (Pa.s)	0.016

Stress	Shear rate	Temperature	Velocity	Torque
Pa	1/s	°C	rad/s	μN.m
13.927	10.000	21.301	0.349	787.549
14.274	11.579	21.300	0.404	807.167
14.753	13.158	21.300	0.459	834.279
15.163	14.737	21.301	0.514	857.450
15.503	16.316	21.301	0.570	876.644
15.801	17.895	21.300	0.625	893.518
16.088	19.474	21.301	0.680	909.762
16.371	21.053	21.300	0.735	925.773
16.684	22.632	21.300	0.790	943.467
17.010	24.211	21.299	0.845	961.900
17.237	25.790	21.300	0.900	974.747
17.431	27.368	21.300	0.955	985.698
17.595	28.947	21.300	1.010	994.978
17.750	30.526	21.300	1.066	1003.730
17.905	32.105	21.301	1.121	1012.500
18.051	33.684	21.300	1.176	1020.780
18.196	35.263	21.299	1.231	1028.930
18.347	36.842	21.300	1.286	1037.500
18.499	38.421	21.299	1.341	1046.080
18.642	40.000	21.301	1.396	1054.200

Sample 29:

Concentration(% by volume)	20.4
Density (kg/m ³)	1335
Bingham yield stress (Pa)	10.77
Bingham plastic viscosity (Pa.s)	0.5
Casson yield stress (Pa)	7.8
Casson plastic viscosity (Pa.s)	0.15

Stress	Shear rate	Temperature	Velocity	Torque
Pa	1/s	°C	rad/s	μN.m
10.083	4.000	23.000	0.140	570.200
10.494	5.143	23.000	0.180	593.430
11.985	6.286	23.000	0.219	677.742
13.300	7.429	22.999	0.259	752.068
14.448	8.571	23.001	0.299	816.986
15.492	9.714	22.999	0.339	876.047
16.346	10.857	23.001	0.379	924.365
17.114	12.000	22.999	0.419	967.762
17.845	13.143	23.001	0.459	1009.080
18.506	14.286	22.999	0.499	1046.500
19.110	15.429	23.000	0.539	1080.670
19.590	16.571	23.000	0.578	1107.810
20.024	17.714	23.000	0.618	1132.340
20.422	18.857	23.000	0.658	1154.840
20.779	20.000	23.000	0.698	1175.010

Sample 30:

Concentration(% by volume)	17.7
Density (kg/m ³)	1290
Bingham yield stress (Pa)	13.9
Bingham plastic viscosity (Pa.s)	0.21
Casson yield stress (Pa)	9.73
Casson plastic viscosity (Pa.s)	0.38

Stress	Shear rate	Temperature	Velocity	Torque
Pa	1/s	°C	rad/s	μN.m
11.632	8.000	22.900	0.279	657.757
11.328	8.706	22.900	0.304	640.585
11.834	9.412	22.899	0.329	669.173
12.360	10.118	22.900	0.353	698.936
12.897	10.824	22.899	0.378	729.319
13.426	11.529	22.901	0.402	759.202
13.914	12.235	22.899	0.427	786.843
14.430	12.941	22.900	0.452	815.988
14.886	13.647	22.901	0.476	841.800
15.269	14.353	22.900	0.501	863.412
15.640	15.059	22.900	0.526	884.433
15.970	15.765	22.900	0.550	903.056
16.387	16.471	22.900	0.575	926.657
16.738	17.177	22.900	0.600	946.510
17.104	17.882	22.900	0.624	967.207
17.469	18.588	22.899	0.649	987.830
17.811	19.294	22.900	0.673	1007.180
18.125	20.000	22.900	0.698	1024.950

Sample 31:

Concentration(% by volume)	19.8
Density (kg/m ³)	1325
Bingham yield stress (Pa)	18
Bingham plastic viscosity (Pa.s)	0.1
Casson yield stress (Pa)	14.77
Casson plastic viscosity (Pa.s)	0.017

Stress	Shear rate	Temperature	Velocity	Torque
Pa	1/s	°C	rad/s	μN.m
14.111	8.000	22.900	0.279	797.932
14.742	9.590	22.900	0.335	833.632
15.525	11.180	22.899	0.390	877.892
16.307	12.769	22.900	0.446	922.117
16.825	14.359	22.900	0.501	951.416
17.245	15.949	22.900	0.557	975.153
17.616	17.539	22.900	0.612	996.166
17.983	19.128	22.900	0.668	1016.910
18.317	20.718	22.900	0.723	1035.780
18.660	22.308	22.900	0.779	1055.200
19.023	23.897	22.901	0.834	1075.730
19.519	25.487	22.899	0.890	1103.760
19.926	27.077	22.901	0.945	1126.810
20.182	28.667	22.900	1.001	1141.280
20.405	30.256	22.901	1.056	1153.870
20.606	31.846	22.900	1.112	1165.250
20.792	33.436	22.899	1.167	1175.770
20.966	35.026	22.901	1.223	1185.620
21.134	36.615	22.900	1.278	1195.090
21.303	38.205	22.900	1.334	1204.650
21.473	39.795	22.900	1.389	1214.250
21.635	41.385	22.899	1.445	1223.430

Sample 32:

Concentration(% by volume)	20.1
Density (kg/m ³)	1331
Bingham yield stress (Pa)	22.4
Bingham plastic viscosity (Pa.s)	0.124
Casson yield stress (Pa)	18.4
Casson plastic viscosity (Pa.s)	0.024

Stress	Shear rate	Temperature	Velocity	Torque
Pa	1/s	°C	rad/s	μN.m
17.111	8.000	24.000	0.279	967.588
17.130	8.857	24.000	0.309	968.671
17.757	9.714	23.999	0.339	1004.160
18.373	10.572	24.001	0.369	1038.950
19.008	11.429	23.999	0.399	1074.870
19.568	12.286	24.000	0.429	1106.560
20.113	13.143	24.001	0.459	1137.340
20.636	14.000	23.999	0.489	1166.920
21.154	14.857	24.000	0.519	1196.240
21.559	15.714	24.000	0.549	1219.150
21.980	16.571	24.000	0.578	1242.920
22.343	17.429	24.000	0.608	1263.480
22.717	18.286	24.001	0.638	1284.630
23.094	19.143	23.999	0.668	1305.920
23.417	20.000	24.001	0.698	1324.220

Sample 33:

Concentration(% by volume)	15.6
Density (kg/m ³)	1256
Bingham yield stress (Pa)	8.17
Bingham plastic viscosity (Pa.s)	0.0324
Casson yield stress (Pa)	7.06
Casson plastic viscosity (Pa.s)	0.0045

Stress	Shear rate	Temperature	Velocity	Torque
Pa	1/s	°C	rad/s	μN.m
5.475	4.000	22.000	0.140	309.579
6.139	5.941	22.000	0.207	347.139
6.682	7.882	22.000	0.275	377.861
7.086	9.824	22.000	0.343	400.706
7.383	11.765	22.001	0.411	417.471
7.634	13.706	21.999	0.478	431.681
7.873	15.647	22.001	0.546	445.214
8.100	17.588	22.000	0.614	458.061
8.343	19.529	22.001	0.682	471.806
8.609	21.471	22.000	0.749	486.814
8.793	23.412	21.999	0.817	497.205
8.923	25.353	22.000	0.885	504.557
9.027	27.294	22.001	0.953	510.481
9.119	29.235	22.000	1.021	515.648
9.203	31.177	21.999	1.088	520.445
9.280	33.118	22.001	1.156	524.756
9.352	35.059	21.999	1.224	528.871
9.420	37.000	22.000	1.292	532.671
9.484	38.941	21.999	1.359	536.314
9.544	40.882	22.000	1.427	539.707
9.605	42.824	22.001	1.495	543.169
9.668	44.765	22.000	1.563	546.686
9.726	46.706	22.001	1.630	549.975

Appendix 3: Velocity measurements for spheres falling in Kaolinite-water suspensions

Relative standard deviation (σ_{rel}):

$$\sigma_{re} = \sqrt{\frac{\sum_{i=1}^n (V_{ti} - \overline{V_{ti}})^2}{n}} \times \frac{1}{\overline{V_{ti}}} \times 100$$

V_{ti} : measured terminal settling velocity in each settling experiment (m/s)

$\overline{V_{ti}}$: average of measured velocities for identical fluid-particle systems (m/s)

n: number of measured velocities for identical fluid-particle systems

Sample #*	d(m)	ρ_s (kg/m ³)	V_{ti} (m/s)	V_{tm} (m/s)	σ_{rel} (%)
1	0.0127	2710	0.610	0.620	12.6
			0.630		
			0.720		
			0.500		
2	0.0127	2710	0.590	0.640	4.7
			0.656		
			0.646		
			0.612		
3	0.0127	2710	0.640	0.660	3.6
			0.650		
			0.660		
			0.680		
4	0.0127	2710	0.690	0.650	8.3
			0.581		
			0.626		
			0.714		
5	0.0127	2710	0.581	0.593	4.0
			0.563		
			0.626		
			0.604		

*The "Sample #" corresponds to fluid properties presented in Appendix 2

Sample #	d(m)	ρ_s (kg/m ³)	V _{ti} (m/s)	V _{tm} (m/s)	σ_{rel} (%)
6	0.0191	7697	1.549	1.472	3.5
			1.418		
			1.433		
			1.489		
	0.0159	7722	1.374	1.293	4.2
			1.333		
			1.340		
			1.327		
			1.140		
			1.241		
	0.0143	7684	1.270	1.270	2.8
			1.314		
			1.213		
			1.301		
			1.252		
	0.0127	7841	1.150	1.181	2.2
			1.136		
			1.170		
			1.218		
			1.196		
1.191					
1.186					
1.213					
1.170					
0.0127	2710	0.022	0.028	13.7	
		0.030			
		0.032			
		0.027			

Sample #	d(m)	ρ_s (kg/m ³)	V _{ti} (m/s)	V _{tm} (m/s)	σ_{rel} (%)
7	0.0143	7684	1.497	1.461	2.8
			1.489		
			1.418		
			1.411		
			1.489		
	0.0127	7841	1.481	1.457	2.0
			1.473		
			1.449		
			1.403		
			1.481		
	0.0127	2710	0.416	0.405	4.1
			0.396		
			0.381		
			0.416		
			0.383		
0.436					
8	0.0159	7722	1.103	1.270	8.0
			1.282		
			1.320		
			1.374		
	0.0127	2710	0.385	0.404	3.6
			0.401		
			0.411		
			0.393		
			0.431		
			0.401		

Sample #	d(m)	ρ_s (kg/m ³)	V _{ti} (m/s)	V _{tm} (m/s)	σ_{rel} (%)
9	0.0191	7697	1.605	1.591	0.7
			1.586		
			1.576		
			1.595		
	0.0159	7722	1.426	1.383	3.5
			1.360		
			1.314		
			1.433		
	0.0143	7684	1.218	1.185	10.8
			1.186		
			1.186		
			0.921		
			1.264		
			1.333		
0.0127	7841	1.140	1.195	2.5	
		1.202			
		1.207			
		1.218			
		1.181			
		1.224			
10	0.0143	7684	1.367	1.359	12.8
			1.347		
			1.347		
			1.374		
	0.0127	7841	1.258	1.262	6.1
			1.270		
			1.264		
			1.258		
			1.258		
			1.258		

Sample #	d(m)	ρ_s (kg/m ³)	V _{ti} (m/s)	V _{tm} (m/s)	σ_{rel} (%)
11	0.0191	7697	1.576	1.584	1.1
			1.595		
			1.605		
			1.558		
	0.0175	7675	1.481	1.510	5.1
			1.506		
			1.540		
			1.514		
	0.0159	7722	1.457	1.455	8.9
			1.449		
			1.457		
			1.473		
			1.441		
	0.0143	7684	1.327	1.337	18.4
			1.333		
			1.347		
1.327					
1.354					
0.0127	7841	1.276	1.253	1.5	
		1.270			
		1.252			
		1.229			
		1.235			
12	0.0127	7841	1.309	1.282	2.7
			1.285		
			1.255		
			1.279		
13	0.0190	2790	0.770	0.786	1.4
			0.779		
			0.784		
			0.798		
			0.798		

Sample #	d(m)	ρ_s (kg/m ³)	V_{ti} (m/s)	V_{tm} (m/s)	σ_{rel} (%)
14	0.0143	7684	1.489	1.436	3.3
			1.449		
			1.441		
			1.347		
			1.457		
	0.0127	7841	1.396	1.385	2.3
			1.389		
			1.327		
			1.426		
			1.389		
	0.0190	2790	0.596	0.621	2.9
			0.631		
			0.623		
			0.606		
			0.647		
	0.0159	2790	0.528	0.514	3.0
			0.494		
			0.498		
			0.519		
			0.532		
0.0127	2790	0.267	0.264	7.6	
		0.226			
		0.273			
		0.287			
		0.269			
15	0.0127	2710	0.212	0.243	8.7
			0.238		
			0.270		
			0.251		
16	0.0127	7841	1.112	1.101	1.7
			1.121		
			1.131		
			1.103		
			1.039		

Sample #	d(m)	ρ_s (kg/m ³)	V_{ti} (m/s)	V_{tm} (m/s)	σ_{rel} (%)
17	0.0143	7684	0.927	0.925	1.4
			0.931		
			0.899		
			0.937		
			0.931		
	0.0159	7722	1.103	1.093	2.6
			1.039		
			1.098		
			1.098		
			1.126		
18	0.0190	3940	0.494	0.490	4.7
			0.476		
			0.464		
			0.524		
19	0.0190	3940	0.017	0.013	19.4
			0.010		
			0.012		
			0.013		
20	0.0159	3957	0.004	0.004	15.3
			0.003		
			0.004		
			0.003		
22	0.0190	3940	0.224	0.247	6.3
			0.248		
			0.237		
			0.262		
			0.265		
23	0.0159	3957	0.038	0.042	9.8
			0.038		
			0.044		
			0.044		
			0.049		
	0.0143	3950	0.011	0.011	5.9
			0.010		
			0.010		
			0.011		

Sample #	d(m)	ρ_s (kg/m ³)	V_{ti} (m/s)	V_{tm} (m/s)	σ_{rel} (%)
21	0.0143	7684	1.165	1.126	6.4
			1.207		
			1.015		
			1.117		
	0.0127	7841	1.008	0.985	6.3
			1.055		
			0.884		
			0.993		
	0.0190	3940	0.533	0.517	3.3
			0.524		
			0.488		
			0.522		
	0.0159	3957	0.293	0.298	3.3
			0.291		
			0.318		
			0.301		
			0.288		
			0.299		
	0.0140	3904	0.062	0.058	4.1
			0.057		
0.055					
0.058					
0.0190	2790	0.006	0.005	14.7	
		0.005			
		0.004			
		0.004			

Sample #	d(m)	ρ_s (kg/m ³)	V _{ti} (m/s)	V _{tm} (m/s)	σ_{rel} (%)
24	0.0190	7697	1.252	1.221	3.4
			1.218		
			1.155		
			1.258		
	0.0175	7675	1.117	1.117	5.8
			1.218		
			1.094		
			1.039		
	0.0159	7722	1.027	1.032	3.3
			1.043		
			0.982		
			1.076		
	0.0143	7684	0.730	0.803	10.2
			0.912		
			0.718		
			0.854		
0.0127	7841	0.597	0.660	6.4	
		0.711			
		0.649			
		0.682			
0.0190	3940	0.052	0.059	12.6	
		0.060			
		0.071			
		0.054			
25	0.0190	2790	0.003	0.003	22.3
			0.004		
			0.002		
			0.003		
27	0.0158	2790	0.018	0.020	12.0
			0.024		
			0.019		
			0.018		

Sample #	d(m)	ρ_s (kg/m ³)	V_{ti} (m/s)	V_{tm} (m/s)	σ_{rel} (%)
26	0.0190	3940	0.509	0.522	6.0
			0.489		
			0.573		
			0.517		
	0.0159	3957	0.316	0.381	10.1
			0.416		
			0.391		
			0.401		
	0.0140	3904	0.196	0.194	10.2
			0.158		
			0.209		
			0.192		
	0.0127	3925	0.215	0.061	20.4
			0.082		
			0.059		
			0.054		
0.0190	2790	0.049	0.004	11.2	
		0.004			
		0.005			
		0.004			
30	0.0190	3940	0.004	0.363	14.7
			0.406		
			0.423		
			0.293		
	0.0159	3957	0.330	0.098	15.5
			0.099		
			0.095		
			0.111		
			0.093		
	0.0143	3950	0.090	0.046	21.7
			0.046		
			0.063		
0.038					
			0.039		

Sample #	d(m)	ρ_s (kg/m ³)	V _{ti} (m/s)	V _{tm} (m/s)	σ_{rel} (%)
28	0.0190	3940	0.683	0.621	9.3
			0.675		
			0.565		
			0.563		
	0.0159	3957	0.444	0.431	2.6
			0.417		
			0.425		
			0.440		
	0.0143	3950	0.364	0.300	16.8
			0.237		
			0.266		
			0.333		
	0.0140	3904	0.316	0.283	20.5
			0.360		
			0.212		
			0.246		
	0.0127	3925	0.156	0.159	31.7
			0.156		
			0.091		
			0.234		
0.0190	2790	0.036	0.035	13.1	
		0.037			
		0.028			
		0.040			
0.0158	2790	0.004	0.004	26.9	
		0.004			
		0.006			
		0.005			
		0.004			

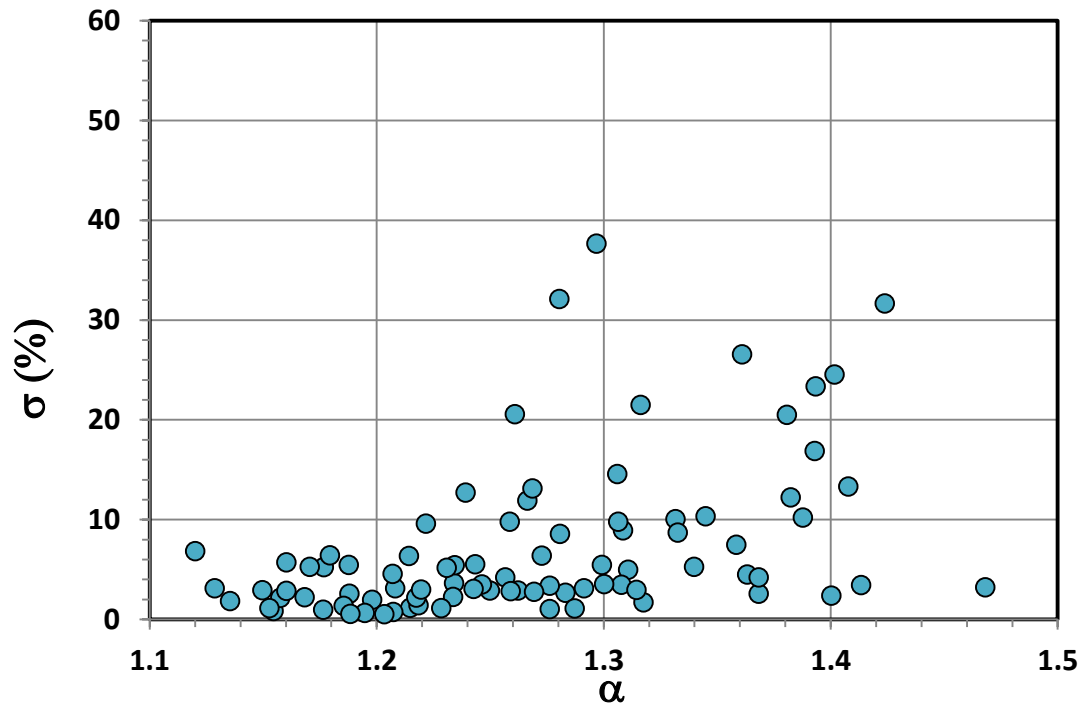
Sample #	d(m)	ρ_s (kg/m ³)	V _{ti} (m/s)	V _{tm} (m/s)	σ_{rel} (%)
29	0.0190	7697	1.290	1.333	2.3
			1.314		
			1.381		
			1.347		
	0.0175	7675	1.264	1.283	1.3
			1.307		
			1.288		
			1.270		
	0.0159	7722	1.213	1.179	6.6
			1.288		
			1.089		
			1.126		
	0.0143	7684	0.993	1.084	5.8
			1.136		
			1.059		
			1.150		
	0.0127	7841	0.918	0.920	6.9
			0.944		
			0.996		
			0.822		
	0.0190	3940	0.412	0.332	17.2
			0.306		
			0.354		
			0.256		
	0.0159	3957	0.035	0.032	6.1
			0.030		
			0.032		
			0.031		
0.0143	3950	0.008	0.010	16.5	
		0.010			
		0.012			
		0.008			
0.0140	3904	0.008	0.007	12.2	
		0.006			
		0.007			
		0.007			
0.0127	3925	0.004	0.004	0.0	
		0.004			
		0.004			
		0.004			

Sample #	d(m)	ρ_s (kg/m ³)	V _{ti} (m/s)	V _{tm} (m/s)	σ_{rel} (%)
31	0.0190	7697	1.218	1.307	5.0
			1.314		
			1.295		
			1.403		
	0.0175	7675	1.258	1.302	2.5
			1.314		
			1.288		
			1.347		
	0.0159	7722	1.282	1.263	1.1
			1.252		
			1.270		
			1.247		
	0.0143	7684	1.068	1.138	5.8
			1.150		
			1.241		
			1.094		
	0.0127	7841	0.964	0.952	2.8
			0.890		
			1.004		
			0.950		
	0.0140	3950	0.042	0.048	10.0
			0.055		
			0.050		
			0.047		
	0.0190	3940	0.382	0.425	10.2
			0.392		
			0.424		
			0.500		
0.0127	3950	0.017	0.016	2.6	
		0.015			
		0.018			
		0.014			
0.0159	3957	0.238	0.202	32.0	
		0.179			
		0.179			
		0.211			

Sample #	d(m)	ρ_s (kg/m ³)	V _{ti} (m/s)	V _{tm} (m/s)	σ_{rel} (%)
31	0.0143	3950	0.068	0.067	4.9
			0.059		
			0.081		
			0.059		

Sample #	d(m)	ρ_s (kg/m ³)	V _{ti} (m/s)	V _{tm} (m/s)	σ_{rel} (%)	
33	0.0143	3950	1.000	0.687	11.9	
			0.673			
			0.732			
			0.616			
	0.0140	3904	3904	0.562	0.591	6.4
				0.502		
				0.702		
				0.597		
	0.0127	3925	3925	0.644	0.781	1.1
				1.181		
				0.511		
				0.786		
	0.0190	2790	2790	0.800	0.571	1.7
				0.579		
				0.584		
				0.615		
	0.0159	2790	2790	0.429	0.455	12.2
				0.487		
				0.469		
				0.435		
0.0127	2790	2790	0.195	0.197	12.3	
			0.183			
			0.230			
			0.178			
0.0127	2710	2710	0.162	0.168	3.0	
			0.168			
			0.173			
			0.171			

Sample #	d(m)	ρ_s (kg/m ³)	V _{ti} (m/s)	V _{tm} (m/s)	σ_{rel} (%)
32	0.0190	7697	1.175	1.277	3.0
			1.333		
			1.224		
			1.374		
	0.0175	7675	1.160	1.169	4.2
			1.247		
			1.136		
			1.136		
	0.0159	7722	1.081	1.063	2.9
			1.008		
			1.081		
			1.085		
	0.0143	7684	0.968	0.966	8.6
			0.961		
			0.982		
			0.954		
	0.0127	7841	0.800	0.819	9.8
			0.832		
			0.764		
			0.812		
			0.832		
	0.0190	3940	0.069	0.102	5.6
			0.125		
			0.089		
			0.125		
	0.0159	3957	0.024	0.040	8.6
			0.059		
			0.015		
0.042					
0.012					
0.0143	3950	0.005	0.004	9.3	
		0.004			
		0.005			
		0.003			



Appendix 4: MatLab codes for correlation development

Surface fitting for data points with $\alpha < 1.3$:

```
function [fitresult, gof] = createSurfaceFit1(alpha, TyTB, M_eq_M_N)
alpha = alpha(:);
TyTB = TyTB(:);
M_eq_M_N = M_eq_M_N(:);

%% Fit: 'untitled fit 1'.
ft = fittype( 'a*y^b*exp(x^c)+y^d+e', 'indep', {'x', 'y'}, 'depend',
'z' );
opts = fitoptions( ft );
opts.Display = 'Off';
opts.Lower = [-Inf -Inf -Inf -Inf -Inf];
opts.StartPoint = [0.521493347812023 0.944223846832328
0.305603466997734 0.143327062772478 0.548847435698431];
opts.Upper = [Inf Inf Inf Inf Inf];
opts.Weights = zeros(1,0);
ex = excludedata( alpha, TyTB, 'Indices', [4 12 24 34 43 46 57 64 65
79 91 102] );
opts.Exclude = ex;
[fitresult, gof] = fit( [alpha, TyTB], M_eq_M_N, ft, opts );

% Create a figure for the plots.
figure( 'Name', 'untitled fit 1' );

% Plot fit with data.
subplot( 2, 1, 1 );
h = plot( fitresult, [alpha, TyTB], M_eq_M_N, 'Exclude', ex );
legend( h, 'untitled fit 1', 'M_eq_M_N vs. alpha, TyTB', 'Excluded
M_eq_M_N vs. alpha, TyTB', 'Location', 'NorthEast' );
% Label axes
xlabel( 'alpha' );
ylabel( 'TyTB' );
zlabel( 'M_eq_M_N' );
grid on
view( 11.5, -10 );

% Plot residuals.
subplot( 2, 1, 2 );
h = plot( fitresult, [alpha, TyTB], M_eq_M_N, 'Style', 'Residual',
'Exclude', ex );
legend( h, 'untitled fit 1 - residuals', 'Excluded M_eq_M_N vs.
alpha, TyTB', 'Location', 'NorthEast' );
% Label axes
xlabel( 'alpha' );
ylabel( 'TyTB' );
zlabel( 'M_eq_M_N' );
grid on
view( 26.5, 0 );
```

Surface fitting for data points with $\alpha \geq 1.3$:

```
function [fitresult, gof] = createSurfaceFit1(alpha, TyTB, M_eq_M_N)
alpha = alpha(:);
TyTB = TyTB(:);
M_eq_M_N = M_eq_M_N(:);

%% Fit: 'untitled fit 1'.
ft = fittype( 'a*y^b*exp(x^c)+y^d+e', 'indep', {'x', 'y'}, 'depend',
'z' );
opts = fitoptions( ft );
opts.Display = 'Off';
opts.Lower = [-Inf -Inf -Inf -Inf -Inf];
opts.StartPoint = [0.521493347812023 0.944223846832328
0.305603466997734 0.143327062772478 0.548847435698431];
opts.Upper = [Inf Inf Inf Inf Inf];
opts.Weights = zeros(1,0);
ex = excludedata( alpha, TyTB, 'Indices', [4 12 24 34 43 46 57 64 65
79 91 102] );
opts.Exclude = ex;
[fitresult, gof] = fit( [alpha, TyTB], M_eq_M_N, ft, opts );

% Create a figure for the plots.
figure( 'Name', 'untitled fit 1' );

% % Plot fit with data.
% subplot( 2, 1, 1 );
% h = plot( fitresult, [alpha, TyTB], M_eq_M_N, 'Exclude', ex );
% legend( h, 'untitled fit 1', 'M_eq_M_N vs. alpha, TyTB', 'Excluded
M_eq_M_N vs. alpha, TyTB', 'Location', 'NorthEast' );
% % Label axes
% set (gca, 'FontName', 'Symbol');
% xlabel( 'a' );
% ylabel( 'z' );
% zlabel( 'B' );
% grid on
% view( 11.5, -10 );

% Plot residuals.
subplot( 2, 1, 2 );
h = plot( fitresult, [alpha, TyTB], M_eq_M_N, 'Style', 'Residual',
'Exclude', ex );
legend( h, 'untitled fit 1 - residuals', 'Excluded M_eq_M_N vs.
alpha, TyTB', 'Location', 'NorthEast' );
% Label axes
set (gca, 'FontName', 'Symbol');
xlabel( 'a' );
ylabel( 'z' );
zlabel( 'B' );
grid on
view( 26.5, 0 );
```

The objective function for optimization process:

```

function Err = objective(x)

% global d Rof Vst alpha Meq vt_m

a=x(1);
b=x(2);
c=x(3);
e=x(4);
f=x(5);

%Error calculation for Wilson's method
%-----
% a=2;
% b=-3;
% c=2.6;
% f=5;
Mapp=zeros(107,1);
Rest=zeros(107,1);
vt_p=zeros(107,1);
y=zeros(107,1);
Er=zeros(107,1);
%-----
% Reading properties from xls
d=xlsread('Data-CB-8.xlsx', 1, 'A254:A360');
Rof=xlsread('Data-CB-8.xlsx', 1, 'B254:B360');
Vst=xlsread('Data-CB-8.xlsx', 1, 'D254:D360');
alpha=xlsread('Data-CB-8.xlsx', 1, 'Q254:Q360');
Meq=xlsread('Data-CB-8.xlsx', 1, 'K254:K360');
vt_m=xlsread('Data-CB-8.xlsx', 1, 'P254:P360');
TyTb=xlsread('Data-CB-8.xlsx', 1, 'V254:V360');
% Rest=xlsread('Data-CB-3.xlsx', 1, 'O2:O98');
%-----
%Calculating Re*
for i=1:107

Mapp(i,1)=Meq(i,1)*(a*TyTb(i,1).^b*exp(alpha(i,1).^c)+TyTb(i,1).^e+f)
;
    Rest(i,1)=d(i,1)*Vst(i,1)*Rof(i,1)/Mapp(i,1);
end
%
%-----

%Predicting velocity by Modified method
for i=1:107
if Rest(i,1)<=10

vt_p(i,1)=(Rest(i,1)/(3*(1+0.08*(Rest(i,1)).^1.2))+2.8/(1+30000*(Rest
(i,1)).^(-3.2)));
end

if Rest(i,1)>10
    Q(i,1)=log10(Rest(i,1)/10);

```

```

        y(i,1)=0.2069+0.5*Q(i,1)-0.158*(Q(i,1)).^1.72;
        vt_p(i,1)=(10.^(y(i,1)));
    end

    if Rest(i,1)>=260
        vt_p(i,1)=4.24;
    end
end

%-----
%Calculating collective error
for i=1:107
    Er(i,1)=(vt_p(i,1)-vt_m(i,1)).^2;
end
Err=(mean(Er).^0.5);

```

Appendix 5: Genetic algorithm (GA)

Genetic algorithm is an optimization method used for solving both constrained and unconstrained problems following the process of natural selection. The algorithm generates several solutions in each iteration and selects individuals randomly from the current generation and uses them as parents to produce children of the next generation. A classic optimization algorithm generates a single point at each iteration and the sequence of points reaches an optimum solution while GA generates a population at each iteration and the best point at each population approaches an optimal solution. The feature that makes GA a strong optimization method is that the next population is always selected by computations which uses random number generators. This feature avoids entrapment in local optimums and increases the probability of reaching for the global optimum solution.

The following outline summarizes how the genetic algorithm works*:

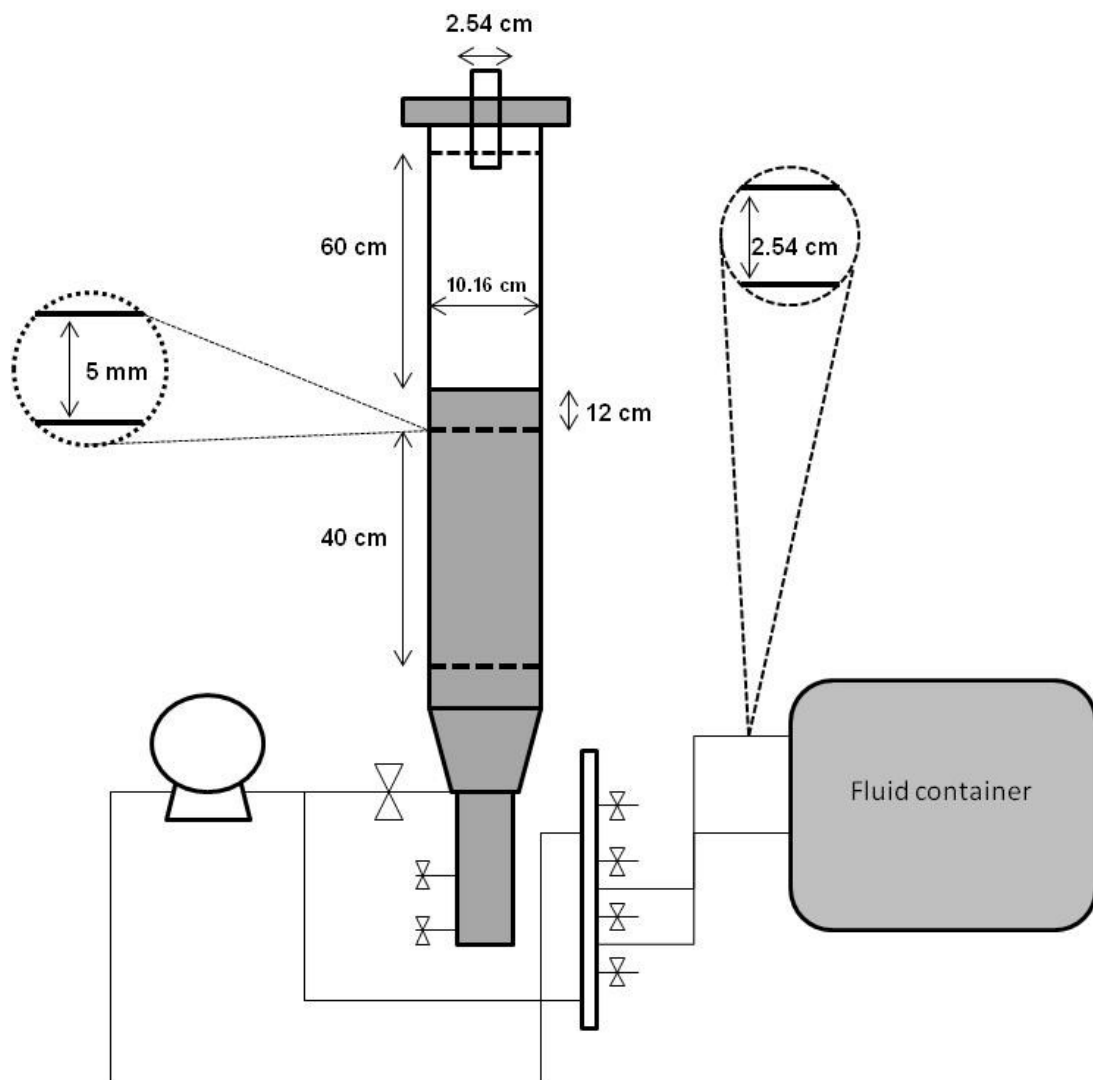
1. The algorithm begins by creating a random initial population.
2. The algorithm then creates a sequence of new populations. At each step, the algorithm uses the individuals in the current generation to create the next population. To create the new population, the algorithm performs the following steps:
 - a. Scores each member of the current population by computing its fitness value.
 - b. Scales the raw fitness scores to convert them into a more usable range of values.
 - c. Selects members, called parents, based on their fitness.

- d. Some of the individuals in the current population that have lower fitness are chosen as *elite*. These elite individuals are passed to the next population.
 - e. Produces children from the parents. Children are produced either by making random changes to a single parent—*mutation*—or by combining the vector entries of a pair of parents—*crossover*.
 - f. Replaces the current population with the children to form the next generation.
3. The algorithm stops when one of the stopping criteria is met.

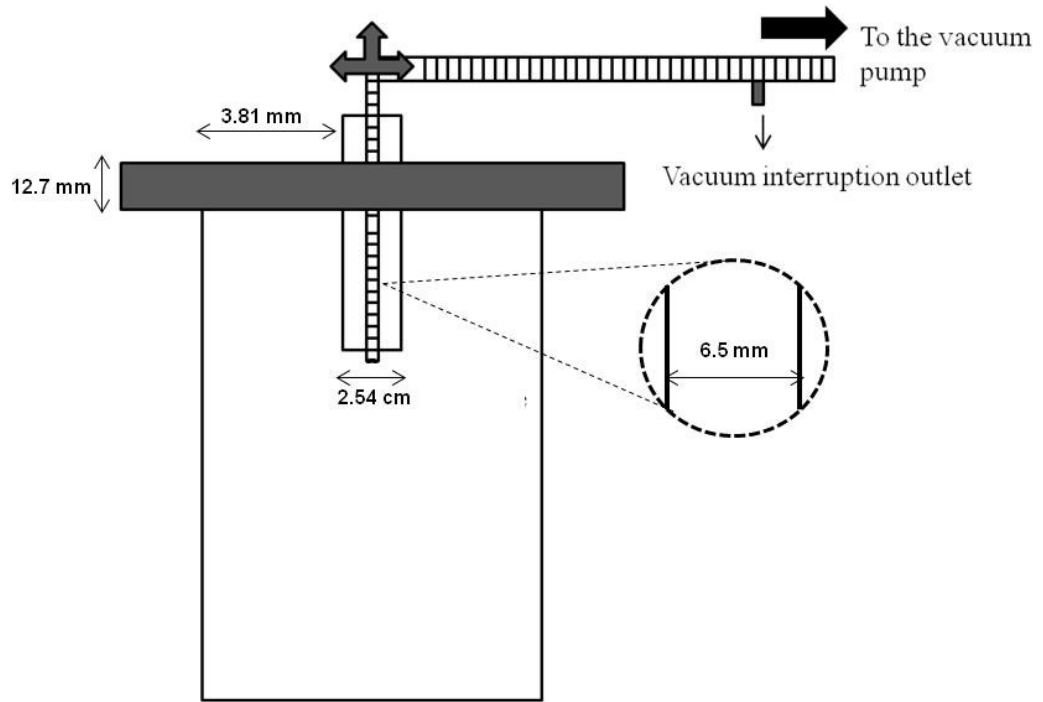
* *Mathworks. (2010). GA Optimization Toolbox: User's Guide (r2010a). Retrieved March 5, 2015 from www.mathworks.com/help/pdf_doc/gads/gads_tb.pdf*

Appendix 6: Diagrams and pictures

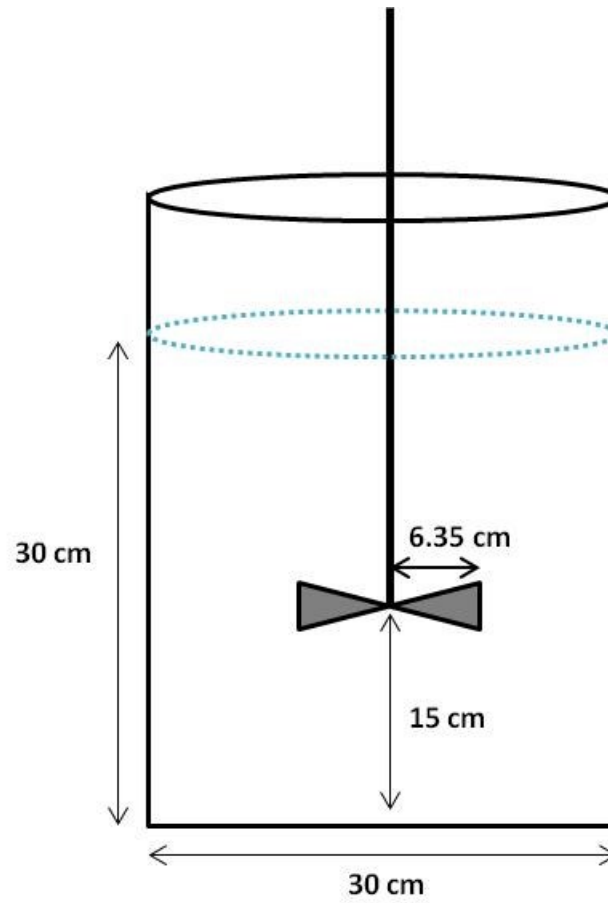
The dimensions of the settling column

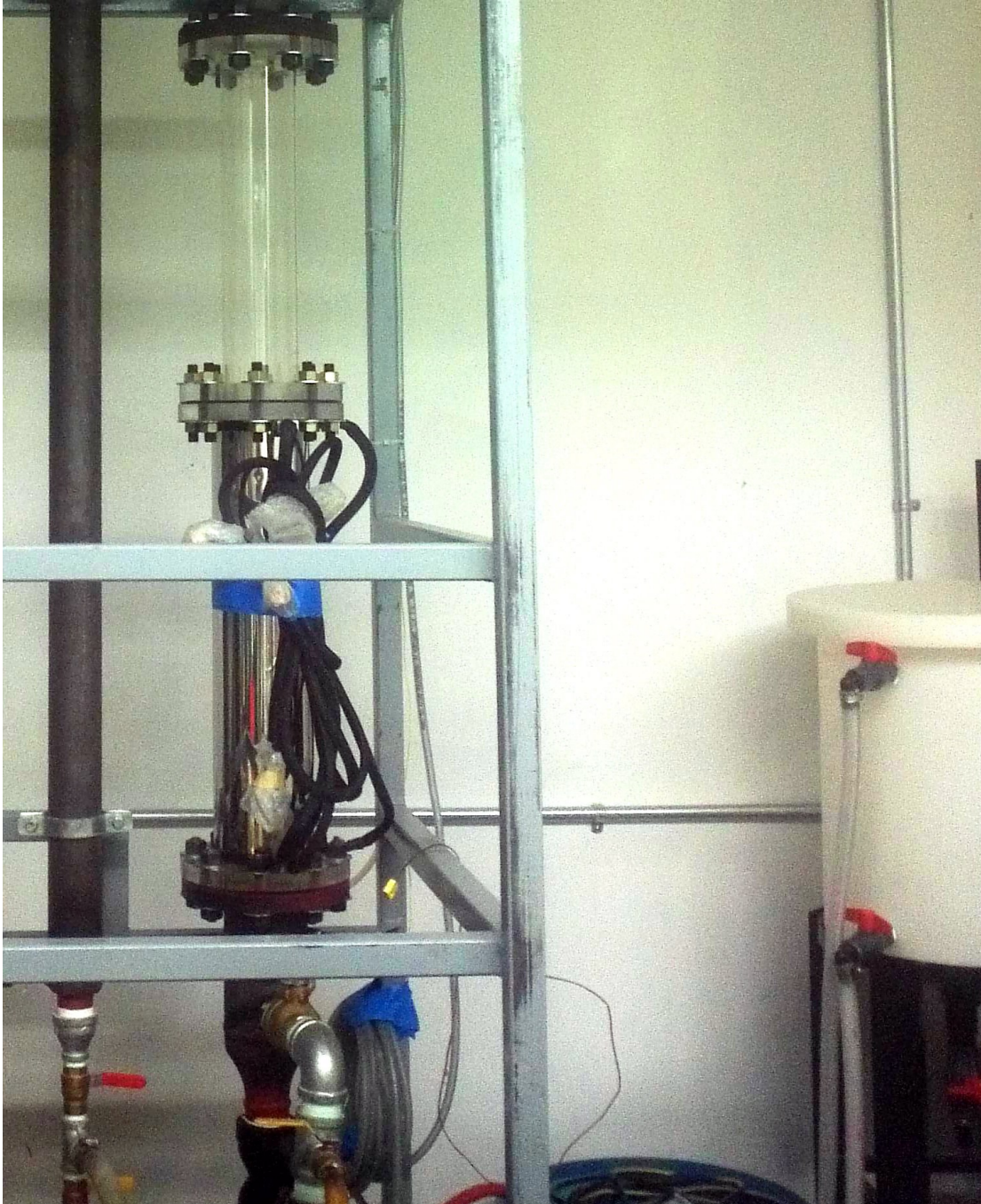


The dimensions of the releasing mechanism

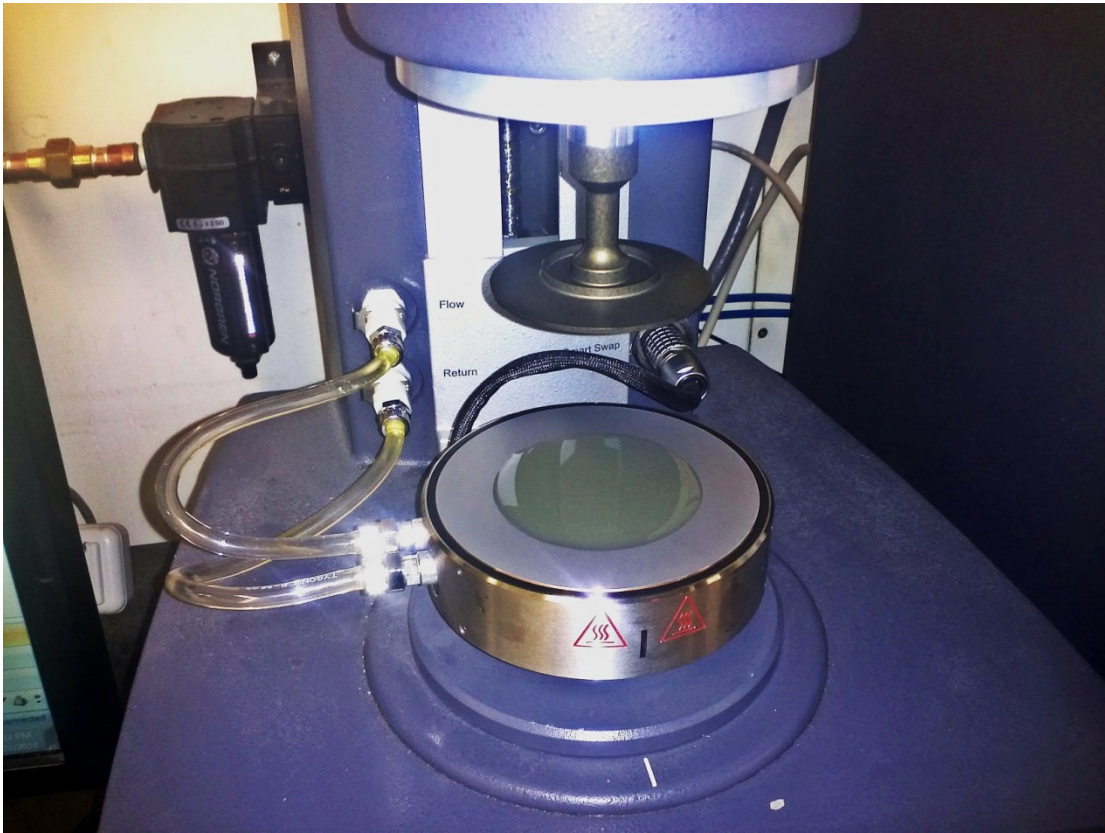


The dimensions of the mixing apparatus





Settling column



Cone-and-plate apparatus used for rheometry tests